LOCALIZATION OF BOSE-EINSTEIN CONDENSATES IN ONE-DIMENSIONAL RANDOM POTENTIALS

DISSERTATION

zur Erlangung des Doktorgrades der
Fakultät für Mathematik und Physik der
Albert-Ludwigs Universität
Freiburg im Breisgau

vorgelegt von
Juan Pablo Ramírez Valdes
aus Medellín in Antioquia, Kolumbien
2017

DEKAN:
Prof. Dr. Gregor Herten

BETREUER DER ARBEIT:
PD Dr. Thomas Wellens
IN ZUSAMMENARBEIT MIT:
Prof. Dr. Andreas Buchleitner

REFERENT:
PD Dr. Thomas Wellens
KOREFERENT:

TAG DER MÜNDLICHEN PRÜFUNG:
04.04.2017

PRÜFER:
PD Dr. Thomas Wellens
Prof. Dr. Thomas Filk
Prof. Dr. Tobias Schätz

Para el Álef, mi familia y mis amigos.

ABSTRACT

Within the present thesis, we investigate, analytically and numerically, the expansion of initially strongly confined wave packets in one-dimensional, correlated random potentials.

In the first part, we focus on single-particle wave packets, i. e. without considering interactions between particles. At long times, the expansion of the wave packet comes to a halt due to destructive interferences leading to *Anderson localization*. The resulting stationary density profile has been measured in experiments on Bose-Einstein condensates in one-dimensional random potentials, but existing theories are unable to explain the behaviour of the density profile at the center. To improve this situation, we develop an analytical description for the disorder-averaged localized density profile. For this purpose, we employ the diagrammatic method of Berezinskii, which we generalize to the case of wave packets, present an analytical expression of the localization length which is valid for small as well as for high energies and finally, develop a self-consistent Born approximation in order to analytically calculate the energy distribution of our wave packet. By comparison with numerical simulations, we show that our theory describes well the complete localized density profile, not only in the tails but also in the center.

In the second part, we discuss the influence of interactions on the spatial expansion of Bose-Einstein condesates in one-dimensional random potentials. We show, by comparison with numerical data, that the quasi-stationary state reached at intermediate times can be well described within the theory developed for the non-interacting case, provided that the interactions are taken into account through the choice of an effective initial state.

ZUSAMMENFASSUNG

Die vorliegende Arbeit enthält analytische und numerische Studien zur Ausbreitung von anfangs räumlich stark begrenzten Wellenpaketen in eindimensionalen zufälligen Potentialen.

Im ersten Teil konzentrieren wir uns auf Wellenpakete einzelner Teilchen, d.h. ohne Berüchsichtigung von Wechselwirkungen zwischen Teilchen. Im Limes langer Zeiten kommt die Ausbreitung des Wellenpakets aufgrund destruktiver Interferenzen, die zur *Anderson Lokalisierung* führen, zum Stillstand. Das sich daraus ergebende stationäre Dichteprofil wurde mit Bose-Einstein-Kondensaten in eindimensionalen zufälligen Potentialen experimentell nachgewiesen. Bisher veröffentlichte Theorien sind jedoch nicht in der Lage, das Verhalten dieses Dichteprofils für kleine Abstände zu erklären. Um diese Situation zu verbessern, entwickeln wir eine analytische Beschreibung des Ensemble-gemittelten lokalisierten Dichteprofils. Zu diesem Zweck verwenden wir die diagrammatische Methode von Berezinskii, welche wir für Wellenpakete verallgemeinern, leiten einen analytischen Ausdruck der Lokalisierungslänge her, welcher sowohl für kleine als auch große Energien gültig ist, und entwickeln schließlich eine selbstkonsistente Bornsche Näherung, um die Energieverteilung unseres Wellenpakets analytisch zu berechnen. Durch den Vergleich mit numerischen Simulationen zeigen wir, dass unsere Theorie das gesamte lokalisierte Dichteprofil sowohl für kleine als auch für große Abstände gut beschreibt.

Im zweiten Teil untersuchen wir den Einfluss von Wechselwirkungen auf die räumliche Ausbreitung von Bose-Einstein-Kondensaten in eindimensionalen zufälligen Potentialen. Durch den Vergleich mit numerischen Daten zeigen wir, dass der quasi-stationäre Zustand, welcher in einem Regime mittlerer Zeiten erreicht wird, gut durch die für den nicht wechselwirkenden Fall entwickelte Theorie beschreiben wird, sofern die Wechselwirkungen durch die Wahl eines effektiven Anlangszustands berücksichtigt werden.

PUBLICATIONS AND CONFERENCES

PUBLICATONS

1. *Localization of wave packets in one-dimensional random potentials*
   Juan Pablo Ramírez Valdes and Thomas Wellens.
   Phys. Rev. A. **93**, 063634 (2016).

CONFERENCES

1. *Wave packet dynamics of a Bose Einstein Condensate in a one dimensional, disordered potential for variable interaction strengths.*
   Juan Pablo Ramírez Valdes, T. Wellens und A. Buchleitner.
   Poster at the spring meeting of the Deutsche Physikalische Gesellschaft (DPG).
   Berlin - Germany, 19 March, 2014.

2. *Dynamics of Bose-Einstein condensates in a one dimensional correlated disorder potential.*
   Juan Pablo Ramírez Valdes, T. Wellens und A. Buchleitner.
   Presentation at the spring meeting of the Deutsche Physikalische Gesellschaft (DPG).
   Heidelberg - Germany, 23 March, 2015.

3. *Analytical description of wave packet expansion in a one dimensional disordered potential.*
   Juan Pablo Ramírez Valdes, T. Wellens und A. Buchleitner.
   Presentation at the conference Extreme Atomic Systems (EAS).
   Riezlern - Austria, 14 February, 2016.

4. *Analytical description of wave packet expansion in a one dimensional disordered potential.*
   Juan Pablo Ramírez Valdes, T. Wellens und A. Buchleitner.
   Presentation at the spring meeting of the Deutsche Physikalische Gesellschaft (DPG).
   Hannover - Germany, 29 February, 2016.

Ohana means family.
Family means nobody gets left behind, or forgotten.

— Lilo & Stitch

DANKSAGUNG – AGRADECIMIENTOS

Mit den Worten auf dieser Seite möchte ich mich bei meinen deutschen und kolumbianischen Freunden und Kollegen bedanken, die mich im Laufe der letzten drei Jahre begleitet und mir Vertrauen gegeben haben.

Zuallererst möchte ich mich bei Andreas für die Aufnahme in seine Arbeitsgruppe und die tägliche gute Arbeitsstimmung bedanken.

Ich bedanke mich bei Thomas, der der intelligenteste und geduldigste Mensch und Physiker ist, den ich in meiner Karriere kennengelernt habe. Vielen Dank dafür, dass Du Dich jederzeit und mit viel Geduld allen meinen Fragen gewidmet hast.

Mein großer Dank gilt auch den Kollegen im 9. Stock für Ihre uneingeschränkte Freundschaft und wissenschaftlichen Ratschläge. Insbesondere ist in diesem Zusammenhang Chahan Kropf zunennen. Danke Chahan, dass Du für mich da warst, als ich eine schwierige Zeit hatte.

Jalina, im Laufe dieser drei Jahren hat mich deine Liebe viele schöne Sachen gelehrt, die ich drei Leben durch die Bücher zu lernen gebraucht hätte.

Uroma, Oma, Valeska und Familie Tschernig, ihr seid für mich ein wichtiger Teil meiner Geschichte in Deutschland. Ich bedanke mich bei Euch für Eure familiäre Liebe und Unterstützung.

Mis agradecimientos más profundos van dirigidos al Álef, el Dios de amor que profesa mí madre, quien siempre ha estado ahí para mí. Gracias Mamá y Papá por su amor incondicional, él cual es un fiel reflejo de sus convicciones. Gracias a mis hermanos: Carlos y Alvaro, por su amor y compañía a pesar de la distancia. Gracias a la familia Valdes, primos y tios, y a mis amigos en Colombia, por estar siempre pendiente de mí a pesar de mi ingratitud.

Diese Arbeit wurde vom Deutschen Akademischen Austauschdienst mit der Nummer 91540377 unterstützt. Die numerischen Simulationen in dieser Arbeit wurden am Black Forest Grid Freiburg durchgeführt.

CONTENTS

1 INTRODUCTION 1
- 1.1 From localization of eigenstates to localization of wave packets 4
- 1.2 The aim of this thesis 4
- 1.3 Outline of this thesis 5

2 MOTIVATION AND STATE OF THE ART 9
- 2.1 Experiments on 1D localization of Bose-Einstein condensates 9
  - 2.1.1 Classical reflection at high potential barriers 9
  - 2.1.2 Experimental observation of Anderson localization 11
- 2.2 Attempts to theoretically describe the average asymptotic density profile 14
  - 2.2.1 Localization length 14
  - 2.2.2 Corrections to pure exponential decay 15
  - 2.2.3 Energy distribution 17
- 2.3 Comparison with numerical results 18

3 MODEL AND GENERAL CONCEPTS 21
- 3.1 Model 21
  - 3.1.1 Schrödinger equation 21
  - 3.1.2 Initial state 22
  - 3.1.3 Asymptotic density profile 23
- 3.2 Random potentials 23
  - 3.2.1 Correlation functions and cumulants 24
  - 3.2.2 Gaussian disorder 25
  - 3.2.3 Speckle potentials 27
- 3.3 Green function 28
  - 3.3.1 Free particle Green function 30
  - 3.3.2 Lippmann-Schwinger equation and Born series 31
  - 3.3.3 Average Green function: Dyson equation 32

4 DIAGRAMMATIC CALCULATION OF THE ASYMPTOTIC DENSITY PROFILE 37
- 4.1 Density-density autocorrelation function at fixed energy: method of Berezinskii 37
  - 4.1.1 Average intensity propagator 38
  - 4.1.2 Essential diagrams 39
  - 4.1.3 Summation of essential diagrams 41
  - 4.1.4 Discussion 45
- 4.2 Generalization of Berezinskii's method to wave packets 45
  - 4.2.1 Average intensity propagator with two different source points 46

4.2.2 Neglect of disorder in the vicinity of the source points 46
4.2.3 Including disorder in the vicinity of the source points 48
5 LYAPUNOV EXPONENT 51
5.1 Definition 52
5.2 Numerical determination 53
5.3 Perturbation theory 54
5.3.1 Phase formalism 54
5.3.2 Born approximation 56
5.4 Exact expression for uncorrelated potentials 58
5.4.1 Thouless' relation between Lyapunov exponent and density of states 58
5.4.2 Average density of states for uncorrelated potentials: Halperin's method 60
5.5 Interpolation method for correlated potentials 62
6 SPECTRAL FUNCTION 65
6.1 Definition 65
6.2 Born approximation 68
6.3 Self-consistent Born approximation 68
7 COMPARISON BETWEEN THEORY AND NUMERICS 71
7.1 Summary of theoretical results 71
7.2 Numerical algorithm 73
7.3 Results 74
7.3.1 Energy distribution 74
7.3.2 Asymptotic average density 75
7.3.3 Agreement theory vs. numerics in different energy intervals 77
8 INFLUENCE OF INTERACTIONS 81
8.1 Gross-Pitaevskii equation 82
8.2 Long-time behaviour: sub-diffusive spreading 84
8.3 Intermediate times: Quasi-stationary state 86
8.4 Effective Gaussian initial state 88
8.5 Energy probability distribution $P_g(E)$ 89
9 NUMERICAL RESULTS WITH INTERACTIONS 93
9.1 Numerical algorithms for solving the Gross-Pitaevskii equation 94
9.2 Time-dependent expansion of the wave packet 94
9.3 Validity of the effective Gaussian initial state ansatz 96
9.4 Quasi-stationary density profile 101
9.4.1 Discussion of numerical results 101
9.4.2 Comparison with theory 103
10 SUMMARY & OUTLOOK 109

10.1 Summary 109
10.2 Outlook 112

I APPENDIX 113
A SOME IMPORTANT EQUIVALENCES 115
B BEREZINSKII'S METHOD FOR WAVE PACKETS 117
C NUMERICAL INTEGRATION SCHEMES 123

BIBLIOGRAPHY 129

1 INTRODUCTION

Starting from the Drude model (for classical particles)[1] and the Bloch theorem (for waves)[2], research on electron transport has always been a hot topic in physics and other areas of science. For almost three decades, the Bloch theorem with its delocalized states established the basis for describing, e. g., the electronic band structure in solid state physics of regular crystals, whereas electronic transport and conductivity in disordered metals has been described with the classical Drude model, which neglects interferences due to the quantum-mechanical wave nature. In 1958, P. W. Anderson studied electron diffusion in uncorrelated disordered potentials, i. e., non-regular crystal lattice structures, predicting that the electronic energy eigenstates are localized. In the limit of long times, the particle then remains localized in a finite region surrounding its initial position [4]. This phenomenon is known as *Anderson localization* (AL) and arises due to destructive interferences between multiply reflected wave amplitudes. In other words, the electron eigenstates neither satisfy the conditions of the Bloch theorem nor of the classical Drude model. Thereby, the main characteristics of AL is the exponential decay of the spatial probability density of eigenstates in the random potential, where their corresponding exponent is characterized by the localization length L_{loc},[3] which depends on the corresponding electron energy [5]. From the exponential decay of the probability density of eigenstates in the Anderson model, many physical properties which were found using the Bloch model or the Drude model in older works, e. g. concerning the conductivity, had to be revisited

Some important research on the absence of conductivity in electron systems

One of the most important consequence of Anderson's works was to establisch the existence of a transition between extended and localized

1 In the Drude model, the electron transport through a metal atom lattice is described by the kinetic theory, which assumes a classical behavior of the electrons in a solid, and thereby visualizes the electron dynamics as bouncing and re-bouncing of electrons with themselves and the immobile atoms [1], [2].

2 The Bloch model introduces the quantum mechanical wave nature of the particles, and asserts that the particles with a given fixed energy, have the same probability to be situated anywhere within the potential. Therefore, the eigenstates of the particles which travel in periodic lattices are delocalized, which implies that the wave state is spread over the whole periodic potential [3].

3 The inverse of the localization length defines the Lyapunov exponent γ_E. See Sec. 2.2.1.

states driven by the amount of disorder in the underlying three dimensional potential landscape. This metal-insulator transition is called the Anderson transition [6]. Soon after, N. F. Mott and W. D. Twose demonstrated that the energy eigenstates in one and two-dimensional disordered potentials are always localized and, therefore, the Anderson transition only occurs in three-dimensional disordered potentials [7]. In 1979, E. Abrahams *et. al.* found an expression for the dependence of the conductivity in terms of the dimensionless conductance g_c[4], and the size of the disordered potential L [9]. According to this work, in three-dimensional potentials, the energy eigenstates are localized if $g_c < 1$, while in one and two-dimensional potentials, they are localized for all values of g_c, or quasi-extended if the system size is smaller than the localization length. In the 90's, D. Dunlap *et. al.* found an interesting result related to the Anderson theorem: if the disordered potential exhibits correlations between the atoms that constitute it,[5] then the electronic states may become delocalized for specific values of the energy, regardless the dimensionality of the potential [10]. In principle, the effects of specific long-range correlations also led to the possibility of a delocalization-localization transition even in one-dimensional disordered potentials [11]. This illustrates the importance of correlations in the disordered systems and that the Anderson theorem is only valid for uncorrelated potentials.

Although at first, Anderson localization was a phenomenon linked to disordered electron systems, experimentally, one-dimensional Anderson localization has also been observed in other disordered systems, including, e. g., light waves in photonic waveguide lattices [12], microwaves [13] or sound waves [14]. From these experimental results, we may conclude that the physics mechanism behind Anderson localization must be a wave interference phenomenon [15]. In order to show it, researchers focused first to systems where the interactions or nonlinearities are negligible, e. g., light waves in disordered media [16], [17] or ultracold atoms plus optical potentials [18], [19], where the parameter related to the interaction can be easily controlled.

4 g_c was defined as the ratio between two time scales: *i*) the time it takes a conducting electron in a zigzag motion to arrive at the boundary of the potential, and *ii*) the longest time that an electron wavepacket can travel inside a finite potential without visiting the same region twice [8].

5 Given two types atoms a and b, an uncorrelated one-dimensional potentials is obtained, if their positions are statistically independent: *aaababa*, while atoms in the correlated potential always occur in pairs, e. g. *aabaabbbaa*.

On single state localization

The problem to describe the localization of single eigenstates with given energy E is already well studied, and the description successfully achieved. Based on diagrammatic methods, a well-done deduction of the average probability density of one single energy eigenstate, which connects the initial point i and the final point j, was reported by Berezinskii [20]. Later, Gogolin *et. al.* extended the technique to the case of short-range correlated potentials [21], [22]. The basic idea behind [20]–[22] is to get an analytic expression of the density-density autocorrelation function, which provides information about the dependence of the particle density in one point f at time t, on that in some other point i at time $t_0 < t$. For non-interacting fermions (e. g. electrons) at zero temperature, this correlation is mediated only by those eigenstates the energy of which is equal to the Fermi energy. The analytic result found by Berezinskii and Gogolin exhibits an (approximately) exponential decay of the density-density correlation function with increasing distance between the points i and j, which reflects the above-mentioned exponential localization of energy eigenstates.

In [23], D. J. Thoules found an expression of the Lyapunov exponent, for a general 1D potential, related to the cumulative density of states via the Kramers–Kronig relations [24]. For a free particle in a box, the dispersion relation between energy E and wave vector k is parabolic, i. e. $E = \hbar^2 k^2/(2m)$, and, as a result of this relation, it is easy to find the density of states. This situation changes drastically if the particle is subject to random, disordered potentials. For every single realization of a random potential, the energy spectrum changes and the relation between the energy and wave vector is no longer parabolic, especially for small values of energy, which are related to confined states in differents quantum wells produced in every single realization. Here enters B. I. Halperin's contribution [25], where he found the spectral function as the average relation between the energies and the wave vectors for uncorrelated random potentials. In [25], the author also found an analytical expression for the cumulative density of states. Thereby, we may say that the localization of single energy eigenstates for a particle in an uncorrelated one-dimensional disordered potential is a well studied and solved problem, which has an elegant and successful description.

The story of interactions

The interaction between the particles introduces another important aspect in the Anderson localization phenomenon. Interesting results on the destruction of Anderson localization in one-dimensional systems via particle interactions have been found as a consequence of non-lineari-

ties in the non-linear Schrödinger equation or the Gross-Pitaevskii equation. As an example, A. S. Pikovsky and D. L. Shepelyansky developed a numerical study of the spreading of an initially localized wave packet in a one-dimensional discrete nonlinear Schrödinger disordered lattice, finding that the Anderson localization is destroyed by a certain critical strength of nonlinearity [26]. Nevertheless, how the interactions at transient times can affect the long time state of an initially strongly confined wave packet, and the question if there exists or not an average asymptotic state assumed at long times in the presence of interactions, is an interesting problem to solve. Thereby, the analytic description of the particle density at long times remains as non-trivial task to explore and to do.

1.1 FROM LOCALIZATION OF EIGENSTATES TO LOCALIZATION OF WAVE PACKETS

On the other side, the description of the dynamics of wave packets described as a superposition of many energy eigenstates with different energies is also a well-studied problem, but not in total achieved [27], [28]. Several experiments on Anderson localization of Bose-Einstein condensates (BEC) in one-dimensional random potentials have been performed in the last decade [29]–[34]. These experiments have been interpreted in terms of Anderson localization of non-interacting particles, although the interactions between the particles forming the condensate do affect the shape of the initial state reached during a short expansion period following the release of the initially trapped condensate, after which the interactions are assumed to be negligibly small. The appearance of the disorder potential then localizes the condensate's density distribution. The dynamics of wave packets in a one-dimensional random potential, is a much more complex phenomenon that the localization of eigenstates, due to the superposition of many eigenstates with different energies [27], [28]. In general, this superposition leads to a non-exponential decay of the asymptotic density profile reached at long times.

1.2 THE AIM OF THIS THESIS

For an initially strongly confined wave packet, theoretical descriptions have been developed which explain well the exponential or algebraic decay of the localized density profile in the far tails (i. e. for large distances) [27], [28], but, so far, no theory has been able to reproduce the behaviour at the center close to the initial position, where the maximum of the density profile remains. To fill this gap is the first purpose of the present thesis. We will give a theoretical description of the complete

density profile (including the center and the tails) which agrees well with the results of numerical calculations. To capture the correct behavior at the center, it is essential to treat, in particular, the regime of small energies in an adequate way. We achieve this aim by developing a self-consistent Born approximation to calculate the spectral function, as well as by making use of an exact analytical expression of the Lyapunov exponent for uncorrelated potentials [35], which is valid for large as well as for small energies.

The second purpose of the present thesis is to understand how the interactions can affect the expansion of the BEC, and in consequence, the long-time state of initially strongly confined wave packets. Our aim is also to describe analytically the dependence of the long time disorder-averaged localized density profile on the interaction parameter.

1.3 OUTLINE OF THIS THESIS

The thesis is organized as follows:

- In Chapter 2, we start by discussing experiments on localization of Bose-Einstein condensates in one-dimensional disordered potentials in order to lay the motivation for the present thesis. We introduce first the phenomenon of classical reflection at high potential barriers, and distinguish it from Anderson localization in random potentials. Once we addressed these issues, we make a review of some important concepts, e. g., the localization length and the spectral function, in previous theoretical works attempting to describe the average asymptotic density profile. At the end, we show a comparison of the numerical results with the theoretical predictions, where we conclude that the existing theory is able to explain the behaviour of the asymptotic density profile in its wings (i. e. for large distances from the initial position), whereas significant deviations between theory and numerics are observed in the center of the profile (i. e. in the vicinity of the initial position).

- The model and general concepts of multiple scattering theory used in this thesis are explained in Chapter 3. First, we introduce the Hamiltonian and the initial state that we use throughout this thesis. Immediately after, we show how the asymptotic density profile can be expressed in terms of solutions of the stationary Schrödinger equation. Here, we will also focus our attention on the description and the characterization of a set of random potentials in a statistical sense, and introduce the Gaussian disorder model. To finish, we will introduce the concept of Green functions,

which will turn out to be useful in order to derive the Dyson equation as an average over the disorder.

- In Chapter 4, we introduce a diagrammatic method for describing scattering processes in one-dimensional random potentials, and with this, make it possible to review Berezinskii's analytical description of the density-density autocorrelation function at a given energy. Then, we develop a generalization of Berezinskii's method to the case of wave packets, which finally allows us to derive a general equation for the localized, asymptotic density profile of an initially strongly confined wave packet, taking into account the energy distribution of the latter. This equation, Eq. (9), expresses the density profile in terms of the Lyapunov exponent and the spectral function, which are treated in the following two chapters.

- In Chapter 5, we define the concept of the Lyapunov exponent and derive a matrix formalism for the one-dimensional disordered system. Using this matrix formalism, we calculate numerically the Lyapunov exponent for a one-dimensional Gaussian disordered correlated potential. On the one hand, in order to get an analytical expression of the Lyapunov exponent, we introduce the phase formalism and the Born approximation, which leads us to a perturbative expression in terms of the potential second-order correlation function. On the other hand, we disscus Thouless' relation between Lyapunov exponent and density of states, and Halperin's expression for the average density of states for uncorrelated potentials. These two relations leads us to an exact analytical expression for the Lyapunov exponent for uncorrelated potentials. At the end of the chapter, we interpolate between both analytical expressions (one valid for high energies or short wave lengths, the other one small energies or long wave lengths) to find an analytical equation that describes the Lyapunov exponent for one-dimensional disordered correlated potentials in the entire range of energies.

- The spectral funtion as a main quantity to describe the BEC asymptotic density profile is the subject of Chapter 6. We define first the spectral function, and then, we derive the spectral function for the free particle. We then employ the Born approximation in order to derive the spectral function in the presence of a weak random potential for long energies. After this, we develop a self-consistent Born approximation to get an analytical expression for the spectral density which is approximately valid also for small energies.

- Chapter 7 is devoted to do a comparison of the theoretical description developed in the previous chapters (Chapters 4 - 6) with

numerical results. For the latter, we consider periodic boundary conditions. First, we compare the analytical energy distribution function with the numerics, and after that, we show the result of the analytic asymptotic average density and compare with the numerics. Im both cases, we find a good agrement between theory and numerics. As explained at the end of this chapter, small deviations can be explained by the finite size of the numerical system in connection with the periodic boundary conditions, whereas the theory has been developed for an infinite system.

- In the previous chapter, one of the main aims of the present thesis was achieved, i. e., to improve the existing theoretical description of Anderson localization in one-dimensional random potentials, in such a way, that we are able to describe the complete density profile of the asymptotic state. Nevertheless, the description in Chapters 3 - 7 does not consider the interactions between the bosons. In order to consider them, we must introduce a new experimental scenario, as we shortly mentioned in Sec. 2.3, where the BEC is drived by its interactions at transient times. This chapter is devoted to including the interactions between the particles in the description of the asymptotic average BEC density in our model. We set up a theoretical model according to which the interactions are taken into account through the choice of an appropiate effective initial state.

- In Chapter 9, we present the numerical results for the quasi-stationary density, $\overline{n_g(x)}$, of a BEC in a one-dimensional disordered potential, which is driven by interations at transient times. Then, we compare it with the theoretical description developed in Chapter 8. Again, we find good agreement between the theory and the numerics.

- In Chapter 10, we first summarize the main results of this thesis. Secondly, we discuss some open questions which arise on the basis of the results of this thesis.

2

MOTIVATION AND STATE OF THE ART

An important motivation for the present thesis originates from experimental works on Anderson localization of Bose-Einstein condensates (BECs) in random potentials. These experiments are described in Sec. 2.1. We consider the following, experimentally observed scenario: a spatially trapped condensate starts to expand in a one-dimensional random potential as soon as the trap is released. After a certain time, however, the expansion of the condensate comes to a halt, and a quasi-stationary density profile is observed. We will discuss below whether the suppression of the expansion can be regarded as a manifestation of Anderson localization in a one-dimensional random potential. In the following, we will be interested in analyzing the shape of the resulting asymptotic long-time averaged density profile.

We will review previous attempts to describe this asymptotic density profile theoretically in Sec. 2.2. For this purpose, we will briefly introduce and motivate a number of important theoretical concepts (e. g. the localization length and the spectral function) which will be treated in much more detail later in this thesis. As we will see in Sec. 2.3, the present theory is able to explain the behaviour of the asymptotic density profile in its wings (i. e. for large distances from the initial position), whereas significant deviations between theory and numerics are observed in the center of the profile (i. e. in the vicinity of the initial position). Therefore, one of the main aims of the present thesis will be to improve the existing theoretical description of Anderson localization in one-dimensional random potentials, in such a way, that we are able to describe the complete density profile of the asymptotic state.

2.1 EXPERIMENTS ON 1D LOCALIZATION OF BOSE-EINSTEIN CONDENSATES

2.1.1 *Classical reflection at high potential barriers*

Within the context of random potentials, the works [30] and [31] have reported strong reduction of mobility of atoms in an elongated (i. e. effectively one-dimensional) BEC. D. Clément *et. al.* in the Letter [30] started with a ^{87}Rb BEC in a 3D harmonic trap with radial frequency $\omega_\perp/2\pi = 660(4)$ Hz and axial frequency $\omega_z/2\pi = 670(7)$ Hz. The BEC has approximately 3.5×10^5 atoms, Thomas-Fermi half-length $L_{\mathrm{TF}} = 150\ \mu$m, radius $R_{\mathrm{TF}} = 1.5\ \mu$m, and chemical potential $\mu/2\pi\hbar \sim 5$ kHz.

Additionally, there exists an axial 1D random speckle potential. The amplitude of the random fluctuations of the latter is characterized by V_0. The ratio of the correlation length σ_V and the chemical potential μ is $\gamma = \sigma_V/\mu$. Then, the experimentalists turn off the axial trapping potential while the strong transverse confinement continues to exist. Due to the repulsive interactions, the BEC experiences an axial expansion in the random potential. In Fig. (1), it is possible to observes that the root mean square (rms) size L of the BEC reaches a saturation value as a function of time, which decreases with increasing strength γ of the disorder, while the rms size L grows linearly in time in the absence of the random potential ($\gamma = 0$), at a velocity $\sim 2.47(3)$ mm s^{-1}. In the inset, we observe an analogous behaviour of the BEC's longitudinal center of mass motion.

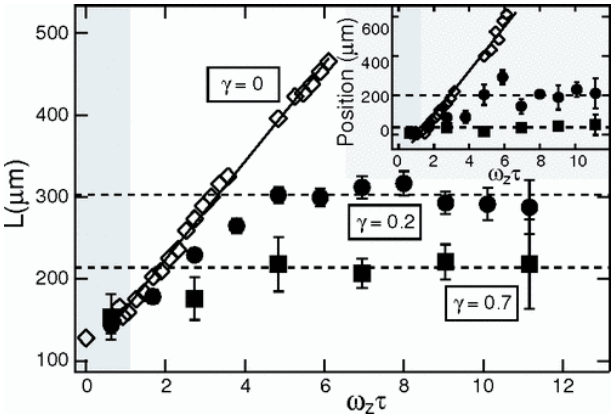

Fig. (1) Time evolution of the BEC axial rms size L for different values of random potential aplitudes $V_0 = \mu\gamma$ for a fixed chemical potential μ. (taken from [30]). All V_0 values are smaller than the chemical potential μ [$\gamma = 0$ (◊), 0.2 (•) and 0.7 (■)]. Every point is the result of an average over three measurements. The solid and the dashed lines are fits to the data and guides to the eye respectively. The inset shows the motion of the BEC center of mass during the axial expansion for the same values of γ. The saturation of L shows a strong suppression of transport due to the disorder.

Nevertheless, the autors in [30] wondered whether their observations can be interpreted in terms of Anderson localization, since the suppression of transport can also be explained by a classical mechanism: If the kinetic energy of the quantum particle is smaller than the highest potential barrier occurring in a typical realization of the random potential, the localization can be understood as a classical reflection process, see Fig. (2). The autors of [30] estimated the probability for the occurrence of high potential barriers using the statistical properties of the random speckle potential (see also Subs. 3.2.3), and concluded that this

is indeed the case. A similar conclusion was also reached in a different experiment performed by C. Fort *et. al.* [31].

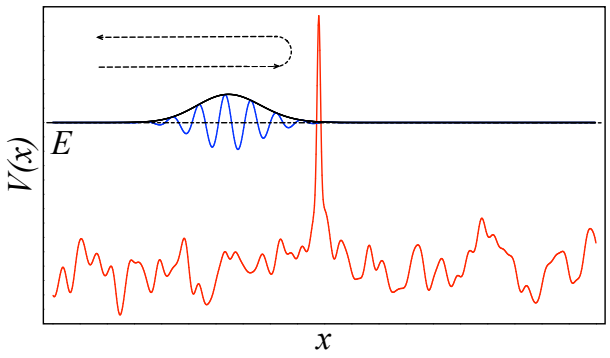

Fig. (2) Classical reflection at high potential barriers. In a given realization of the random potential (red line) in the strong disorder regime, the kinetic energy (E) of the quantum particle (represented by the blue line in the black line packet) can be smaller than the highest potential barrier. In this case, the suppression of transport on a BEC in a 1D random disordered potential experiments can be interpreted in terms of classical reflection at high potential barriers (dotted curve).

2.1.2 *Experimental observation of Anderson localization*

Whereas the above classical localization experiments have been performed in the regime of strong disorder, subsequent theoretical works predicted that it is possible to observe localization of matter waves in optical speckle potentials also for weak disorder [27], [34]. Since, in this regime, the kinetic energy of the quantum particle is larger than the highest potential barrier occurring in a typical realization of the random potential, localization can only be understood as a consequence of the quantum-mechanical wave nature. This is the regime of Anderson localization arising from destructive interference between multiply reflected wave amplitudes [4].

Indeed, in 2008, J. Billy *et. al.* have observed Anderson localization of matter waves in a weak disordered optical speckle potential [29]. In particular, the experiment measured – for the first time with matter waves – the formation of a stationary, exponentially localized wavefunction as a direct signature of Anderson localization. The experiment is performed with a BEC of Rubidium-87 atoms in a one-dimensional optical waveguide which restricts the propagation of the BEC to the z-direction. Furthermore, a controlled disorder potential is created by laser speckle. The detuning of the latter from the atomic frequency is large enough, and the intensity low enough, to ensure that any spontaneous photon

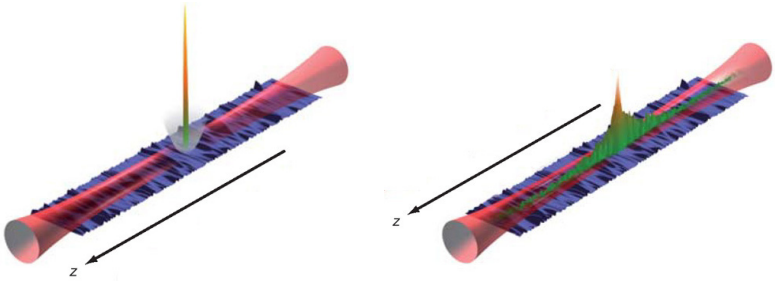

(a) (b)

Fig. (3) Sketch of the BEC localization scenario (taken from [29]). **(a)** A small BEC is trapped in a magnetic trap (gray paraboloid) in the presence of a disordered potential (diffusive blue-black layer), which has amplitude V_0 much smaller than the chemical potential μ of the condensate ($V_0/\mu = 0.12$). The red cylinder represents a horizontal optical waveguide, which ensures the one-dimensional propagation of the BEC. **(b)** Once the magnetic trap is switched off, the BEC spreads along the disordered potential until reaching an asymptotic state at $t = 1$ s.

scattering on the atoms is negligible during the expansion, and thereby, the disorder potential is purely conservative.

Initially, the condensate is trapped in the longitudinal z-direction by an additional magnetic trap. In Fig. (3a), the waveguide and the longitudinal magnetic trap are sketched as a red cylinder and a gray paraboloid, respectively, whereas the disordered speckle potential is drawn in Fig. (3a) as a blue-black layer. The BEC has transverse and longitudinal radii of 3 μm and 35 μm, respectively, whereas the disordered potential length is 4 mm along the z direction.

At time $t = 0$, the longitudinal confinement is switched off, and the BEC expands due to the repulsive interactions between the particles. However, the particle density of the condensate is chosen small enough such that interactions become negligible after a short time of expansion, during which all the interaction energy is converted into kinetic energy. At $t = 1$ s, the BEC reaches the asymptotic state shown in Fig. (3b). The atomic density in Fig. (3b) is observed by direct imaging of the fluorescence of the rubidium atoms irradiated by a resonant probe.

The fact that the density profile $n(z)$ shown in Fig. (3b) indeed corresponds to a stationary state is demonstrated in Fig. (4a), where the profile is shown (as a function of z) at three different times 0.8, 1.0 and 2.0 seconds. We see that the three profiles are almost the same. In particular, in the wings (i. e. for large z), all three curves can be fitted by an exponential function:

$$n(z) \propto \exp\left[-2|z|/L_{loc}\right] \text{ (for large } z\text{)}, \tag{1}$$

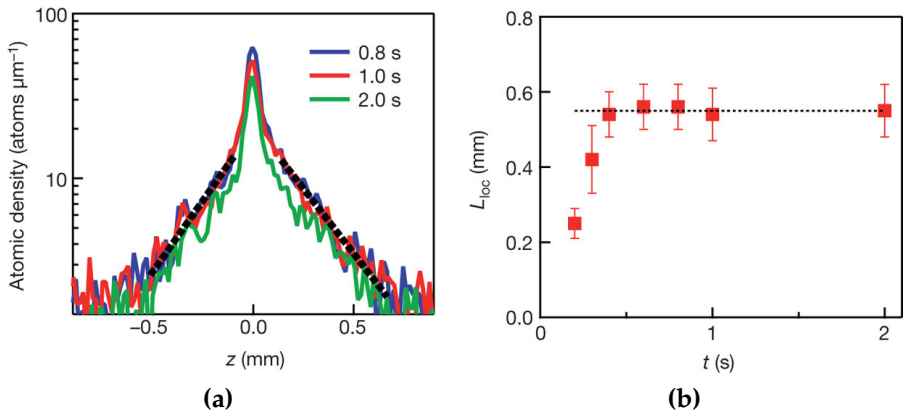

Fig. (4) BEC asymptotic atomic density profile (taken from [29]). **(a)** Three atomic density profiles (in units of atoms μm^{-1}) as a function of distance (in units of nm) at 0.8, 1.0 and 2.0 seconds. The profile is almost constant as a function of time. The wings are fitted by an exponential function (dotted line) defining the localization length. **(b)** Localization length (in units of nm) as a function of time (in units of s). A stationary state is reached after $t \simeq 0.5$ s.

where L_{loc} is the localization length extracted from the fitting. As shown in Fig. (4b), the localization length assumes a stationary value after $t \simeq 0.5$ s.

In summary, the above experiment demonstrates that a weak, one-dimensional disorder potential can stop the expansion of an initially trapped BEC and lead to the formation of a stationary, exponentially localized wavefunction [29]. Note, however, that the experimentally measured density profiles in Fig. (4a) still exhibit time-dependent fluctuations around the exponential fit. Strictly speaking, the wave function is not truly stationary since it is not an eigenfunction of the Hamiltonian. Instead of speaking of a stationary state, we will therefore introduce an asymptotic density profile, defined in Chapter 3 in terms of a long-time average, see Eq. (21). Moreover, even the time-averaged profile still exhibits fluctuations determined by the given realization of the disorder potential. To get rid of these fluctuations, we will employ an additional ensemble average over the realizations of the disorder potential, see Chapter 3.

2.2 ATTEMPTS TO THEORETICALLY DESCRIBE THE AVERAGE ASYMPTOTIC DENSITY PROFILE

2.2.1 *Localization length*

The fact that an exponentially localized wave functions can be realized with BECs and optical speckle potentials has been predicted by the theoretical works [27] and [34]. Indeed, it has been known for a long time that eigenfunctions of the Schrödinger equation in a one-dimensional disorder potential are expontially localized in the generic case [4] (unless the correlations of the random potential are designed in a specific way [11]). A detailed discussion of this result will be presented in Chapter 5 below.

Using a perturbative method (i. e. the Born approximation discussed in Subs. 5.3.2 below) for calculating the localization length at a given energy E, [27] and [34] derived the following result for the localization length as a function of the energy in an optical speckle potential with strength V_0 and correlation length σ_c (see Subs. 3.2.3):

$$L_{\mathrm{loc}}(E) = \begin{cases} \frac{8p_E^2}{\pi V_0^2 \sigma_c (1 - p_E \sigma_c)}, & \text{if } p_E \sigma_c < 1. \\ \infty, & \text{if } p_E \sigma_c \geq 1, \end{cases} \tag{2}$$

where $p_E = \sqrt{E}$ is the free particle momentum in units where $\hbar = 2m = 1$.

The fact that the localization length diverges for $p_E \sigma_c \geq 1$ can be traced back to a specific property of the correlation function of optical speckle potentials (i. e. the finite support of the Fourier transform of its correlation function), which we will discuss in Subs. 3.2.3 below. In fact, only the perturbative result diverges. The exact value of the localization length (including higher orders of perturbation theory [36]) remains finite, but assumes very large values (larger than the size of the experimental system) for $p_E \sigma_c > 1$. The validity of the Born approximation leading to Eq. (2) will be further discussed in Subs. 5.3.2 below.

Eq. (2) describes the localization length as a function of energy. As already mentioned, the BEC in the above experiment does not correspond to an energy eigenfunction, but rather consists of a superposition of eigenfunctions with different energies. The stationary density profile is therefore expected to be given as a superposition of exponentials with different localization lengths. In principle, this may lead, in total, to a non-exponential decay. If, however, the initial momentum distribution of the condensate (after a short period of expansion driven by the interactions, as discussed above) is bounded, with a maximum momentum $p_{\mathrm{max}} < \sigma_c^{-1}$, the behaviour at large z is dominated by the exponent associated to the corresponding energy $E_{\mathrm{max}} = p_{\mathrm{max}}^2$ [27], [34]. This

condition is indeed fulfilled in the experimental runs corresponding to Figs. (3) and (4) above, where $p_{\max}\sigma_c \simeq 0.65$ was measured by observing the free expansion of the BEC in the waveguide in the absence of disorder. The corresponding localization length $L_{\mathrm{loc}}(E_{\max})$ is in good agreement with the above experimental data (see Fig. (3) in [29]).

On the other hand, if $p_{\max}\sigma_c > 1$, a certain fraction of atoms (i. e. those with momenta $p > \sigma_c^{-1}$) are not localized (on the length scale of the experimental setup) according to Eq. (2). As shown in [27] and [34], the remaining localized part of the BEC then exhibits an algebraic ($\propto z^{-2}$) instead of an exponential decay. Also this prediction has been confirmed experimentally, by repeating the above experiment with larger number of atoms leading to $p_{\max}\sigma_c \simeq 1.17$ [29]. In this case, the wings of the localized density profile can be fitted by a power-law decay of the form $1/|z|^{\beta}$ with $\beta \simeq 2$, in agreement with the theoretical prediction.

Thereby, a quantitative agreement between theory and experiment has been achieved at least for the wings of the asymptotic density profile. In order to describe the complete shape of the density profile, however, it is necessary to take into account two additional aspects: first, the energy eigenfunctions in a one-dimensional random potential are not purely exponential functions, but exhibit corrections to an exponential decay which become relevant, in particular, for small distances $|z|$, see Subs. 2.2.2. Second, a suitable way of averaging over the energy distribution of the BEC wave packet must be established, see Subs. 2.2.3.

2.2.2 *Corrections to pure exponential decay*

In order to quantify the corrections to pure exponential decay, we define the density-density autocorrelation function for eigenstates with energy E (see also Subs. 4.1.1):

$$\overline{n_E(x-x')} = \overline{\sum_{n=0}^{\infty} |\phi_n(x)|^2 |\phi_n(x')|^2 \delta(E_n - E)} / \overline{\rho_E}, \tag{3}$$

where $\{|\phi_n\rangle\}$ represents a complete set of energy eigenfunction in the one-dimensional random potential with corresponding energies $\{E_n\}$. The overline describes the average over all realizations of the random potential (see Sec. 3.2). The average density of states:

$$\overline{\rho_E} = \overline{\sum_n |\langle \phi_n | x' \rangle|^2 \delta(E_n - E)}, \tag{4}$$

is introduced to ensure normalization, i. e., $\int \mathrm{d}x\, \overline{n_E(x)} = 1$. The statistical properties of the random potential are assumed to be translationally invariant, such that the quantity defined in Eq. (3) depends only on the difference $x - x'$, and Eq. (4) is independent of x'.

Physically, the function introduced in Eq. (3) describes transport of a quantum particle from an initial position x' to a final position x mediated by eigenfunctions with fixed energy E. For a one-dimensional random potential, this function has been calculated by Berezinskii and Gogolin [20]–[22], using a diagrammatic method, which we will review in Chapter 4. The result is:

$$\begin{aligned}\overline{n_E(x-x')} &= \frac{\pi^2\gamma(E)}{8}\int_0^\infty du\; u\sinh(\pi u)\left[\frac{1+u^2}{1+\cosh(\pi u)}\right]^2 \\ &\times \exp\{-(1+u^2)\gamma(E)|x-x'|/2\}. \end{aligned} \tag{5}$$

where the Lyapunov exponent

$$\gamma(E) = \frac{1}{L_{\rm loc}(E)} \tag{6}$$

defines the inverse of the localization length.

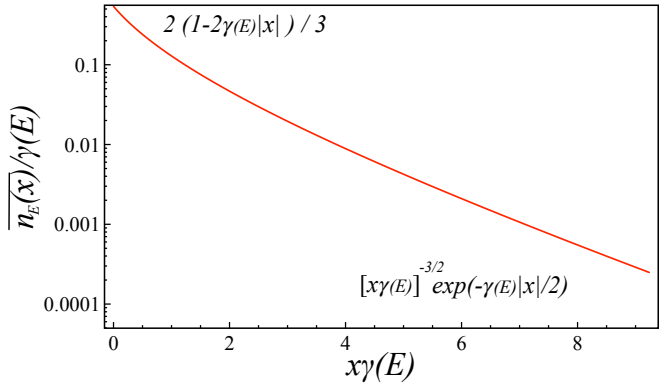

Fig. (5) Density-density autocorrelation function $n_E(x)$ at fixed energy E, see Eq. (3), in units of $\gamma^{-1}(E)$, as a function of dimensionless distance $x\gamma(E)$. For small values of the product $x\gamma(E)$, the asymptotic density behaves as $2(1-2\gamma(E)|x|)/3$, while for higher values it approaches an exponential decay $[x\gamma(E)]^{-3/2}e^{-\gamma(E)|x|/2}$ corrected by an algebraic prefactor.

The function $\overline{n_E(x-x')}$ as given by Eq. (5) is plotted in Fig. (5). For large x, it decays exponentially:

$$\overline{n_E(x)} \underset{x\to\infty}{\longrightarrow} x^{-3/2}e^{-\gamma(E)|x|/2}, \tag{7}$$

(with correction due to an additional algebraic prefactor). Note that the localization length defined by Eqs. (6,7) differs by a factor 4 from the one defined in Eq. (1). We will come back to this point in Chapter 5. On the other hand, the behaviour at small x is given by:

$$\overline{n_E(x)} \underset{x\to 0}{\longrightarrow} \frac{2\gamma(E)}{3}\Big(1-2\gamma(E)|x|\Big), \tag{8}$$

which clearly deviates from the behaviour at large x described by Eq. (7).

2.2.3 *Energy distribution*

In order to average over the initial position and momentum uncertainty of the condensate wave function, the following ansatz was introduced in [27], [28] and [34]:

$$\overline{n(x)} = \int_{-\infty}^{\infty} \mathrm{d}E \int_{-\infty}^{\infty} \mathrm{d}p\mathrm{d}q \; W(q,p) A(p,E) \overline{n_E(x-q)}, \tag{9}$$

where $\overline{n_E(x-q)}$ denotes the density-density autocorrelation function at fixed energy introduced in the previous subsection, and

$$W(q,p) = \int_{-\infty}^{\infty} \mathrm{d}x \; \frac{e^{ipx}}{2\pi} \left\langle q - \frac{x}{2} \middle| \psi_0 \right\rangle \left\langle \psi_0 \middle| q + \frac{x}{2} \right\rangle, \tag{10}$$

is the Wigner function of the initial state $|\psi_0\rangle$. As already mentioned above, the initial state $|\psi_0\rangle$ is evaluated after a short expansion period driven by the interactions, which can be expressed in terms of the solution of the nonlinear Gross-Pitaevskii equation in the absence of disorder (see Chapter 8). After this period, interactions are assumed to be negligible, and the remaining propagation is described by the linear single-particle Schrödinger equation in the presence of the disorder potential, see Eq. (16).

The spectral function $A(p,E)$ in Eq. (9) converts the momentum uncertainty into an energy uncertainty. In other words, it gives the probability that a state with momentum p has energy E in the random potential. A precise definition in terms of the average Green function will be given in Chapter 6. For large momentum p, where the kinetic energy $E = p^2$ (remember that $\hbar = 2m = 1$) dominates over the potential energy, $A(p,E) \simeq A_0(p,E)$ can be approximated by the spectral function

$$A_0(p,E) = \delta(E - p^2) \tag{11}$$

of a free particle. Moreover, for the case of an initially strongly confined wave packet, one can neglect the small initial position uncertainty q in the function $\overline{n_E(x-q)}$. These two approximations lead to [27]:

$$\overline{n(x)} = \int_{-\infty}^{\infty} \mathrm{d}p \; |\tilde{\psi}_0(p)|^2 \; \overline{n_{p^2}(x)} \tag{12}$$

where $|\tilde{\psi}_0(p)|^2$ denotes the momentum distribution of the initial wave packet. The latter exhibits a high-momentum cutoff at

$$p_{\max} = \sqrt{2\mu} \tag{13}$$

where μ is the chemical potential of the initially trapped condensate. Using Eq. (12), the authors of [27] succeeded in predicting the exponential or algebraic decay of the asymptotic density profile discussed in

Subs. 2.2.1. In the exponentially localized regime, i. e., for $p_{\max}\sigma_c < 1$, they obtained the following algebraic correction to Eq. (1):

$$\overline{n(z)} \propto |z|^{-7/2} \exp[-2|z|/L_{\mathrm{loc}}(E_{\max})], \quad \text{(for large } z\text{)}. \tag{14}$$

However, Eq. (12) does not yield an accurate description of the density profile for small z (see Sec. 2.3 below). A more refined approximation was therefore developed in [28]. Here, the position uncertainty in Eq. (9) is fully taken into account and, in addition, the influence of the random potential on the spectral function $A(p, E)$ is evaluated in lowest non-vanishing order of perturbation theory (using the Born approximation discussed in Sec. 6.2). In both theoretical approaches ([27] and [28]), the Lyapunov exponent $\gamma(E)$ entering in Eq. (5) for the density-density autocorrelation function at fixed energy was determined by the inverse of the localization length $L_{\mathrm{loc}}(E)$ in Born approximation, see Eqs. (2) and (6).

2.3 COMPARISON WITH NUMERICAL RESULTS

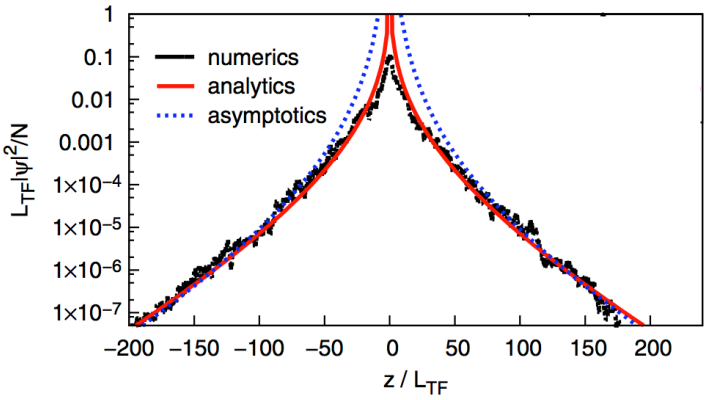

Fig. (6) Density profile of a localized BEC in a speckle potential at time $t = 150/\omega$ (taken from [27]). The probability density times the constant $L_{TF} = \sqrt{4\mu/\omega^2}$ (dimensionless) is shown as a function of the position z (in units of L_{TF}). In the wings of the probability density, the numerical data (black lines) agrees well with the theoretical prediction given by Eq. (12) with a multiplying constant as only fit parameter (red line), and also with the asymptotic formula Eq. (14) (blue dotted line). At the origin, the theoretical prediction strongly overestimates the density obtained from the numerical data. The parameters are: $V_0 = 0.2\mu$, $\xi = \hbar/\sqrt{4m\mu} = 3\sigma_R/2$ and $\sigma_R = 0.27\ \mu$m.

In order to test their theoretical approaches outlined in Subs. 2.2.3, the authors of [27] and [28] performed a comparison with numerical simulations. Fig. (6) shows the result in the regime $\sqrt{2\mu} < \sigma_c^{-1}$ of exponential localization. We see that Eq. (12) gives a good account of the

wings of the density profile. However, to achieve this agreement, the authors had to multiply their result with a constant fitting parameter. This is due to the fact that Eq. (12) strongly overestimates the density in the center of the density profile. The center is determined by the contribution originating from small momenta with correspondingly short localization length, where the Born approximation, see Eq. (2), breaks down. Moreover, the replacement of the spectral function $A(p, E)$ by the free-particle expression $A_0(p, E)$, see Eq. (11), is not valid for small momenta. This difference becomes even more apparent if the profile is plotted on a linear scale instead of the exponential scale shown in Fig. (6), which emphasizes the wings of the density profile.

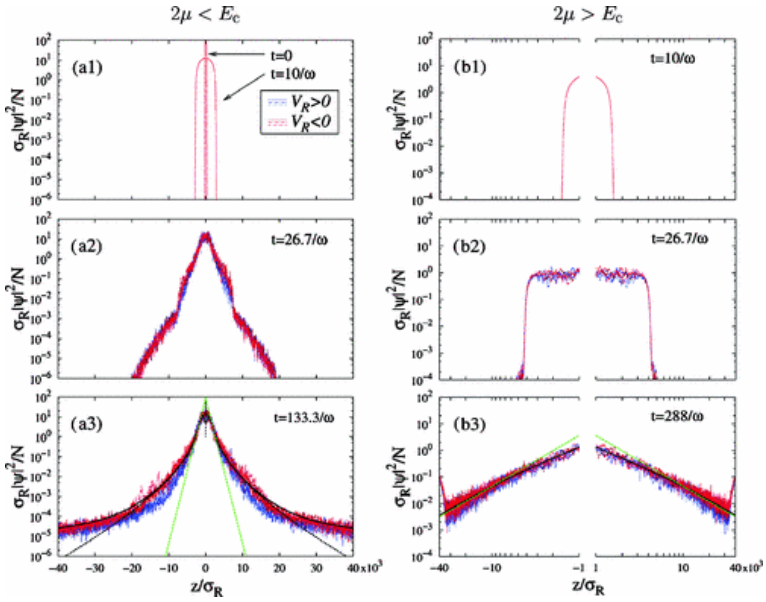

Fig. (7) Time evolution of the probability density of an initially strongly confined matter wave expanding in an one-dimensional random potential for $\mu = 0.22\sigma_c^{-2}$ (left panel) and $\mu = 0.72\sigma_c^{-2}$ (right panel) (taken from [28]). The blue and red lines are runing averages of numerical data for the asymptotic density for three realizations of speckle potentials. The black lines represent the theoretical prediction given by Eq. (9) (with a multiplying constant as fit parameter) taking into account the spectral broadening $A(p, E)$ evaluated in Born approximation. The dotted black lines represent the result obtained by neglecting the spectral broadening ($A(p, E) \to \delta(E - p^2)$). The green dashed line in (a3) shows a fit of $\ln[n(z)] = A - 2\gamma(2\mu)|z|$ (with A as fitting parameter), which describes the behaviour for small $|z|$ (except very close to the center), see Eq. (8). The green dashed line in (b3) is a fit of $n(z) = A/|z|^\beta$, with A and β as fitting parameters. The values of V_0 and ω are $\pm 0.0325 E_c$ and $2 \times 10^{-2}\mu/\hbar$ respectively, where $E_c = \hbar^2/(2m\sigma_c^2)$.

Fig. (7), extracted from [28], shows another comparison, using the more refined theoretical approach which takes into account the spectral broadening described by the function $A(p, E)$. The numerical simulation scheme slightly differs from the one used in Fig. (6): the disorder is switched on, and the interactions switched off, after a certain time $t_i = 10/\omega$ ($\omega = 2 \times 10^{-2}\mu/\hbar$), whereas, both, disorder and interactions are present all the time in the numerical data shown in Fig. (6). Two different values of the chemical potential, corresponding to the previously discussed regimes of exponential (left) and algebraic localization (right) are chosen. As evident from Fig. (7) (a3), the spectral broadening leads to a non-exponential decay also in the first case, since the broadening may lift the energy above the critical value σ_c^{-2} where the localization length diverges (in Born approximation), see Eq. (2). Good agreement between theory and numerics is, again, only achieved after multiplication with a constant fitting factor. For small $|z|$ (close to the center), the theory predicts the occurrence of a non-physical dip, which is not present in the numerical data. Again, the reason for this discrepancy can be traced back to the fact that the Born approximation (both, for the Lyapunov exponent and for the spectral function) is inadequate for small momenta.

In summary, we state that the existing theories for Anderson localization of wave packets in one-dimensional random potentials are unable to describe the behaviour of the localized density profile close to its maximum. In contrast, the wings of the density profile are well described after multiplication with a constant fitting factor. Moreover, the ansatz, Eq. (9), on which these theories are based, is lacking a rigorous theoretical foundation. In the present thesis, we will show how these shortcomings can be cured: first, we will give a derivation of the basic ansatz, Eq. (9), using diagrammatic theory. Second, we will derive new analytical approximations for the Lyapunov exponent and the spectral function which can be used also in the regime of small (in particular also negative) energies. Finally, this will allow us to describe the complete, localized density profile without fitting parameters.

3

MODEL AND GENERAL CONCEPTS

From the previous chapter, the general structure of this thesis becomes apparent: we are interested in describing the asymptotic density profile of a single particle propagating in a one-dimensional disorder potential. A theoretical ansatz for calculating this density profile is given by Eq. (9) above. In Chapter 4, we will provide a justification of this ansatz by using diagrammatic theory. In order to apply this ansatz, we need accurate, analytical estimations of the localization length and the spectral function, which we will derive in Chapters 5 and 6, respectively. We compare our approach with numerical data in Chapter 7, and finally consider the influence of interactions between particles in Chapter 8, comparing later our analytical approach with numerical data in the presence of interactions in Chapter 9 .

In the present chapter, we set the stage for this work by defining the model under consideration and introducing general concepts of multiple scattering theory which will be needed in the following chapters. In Sec. 3.1, we will introduce the Schrödinger equation and the initial state that we will use in this thesis, and show how the asymptotic density profile can be expressed in terms of solutions of the stationary Schrödinger equation. In Sec. 3.2, we will discuss how to characterize the properties of the random potential in a statistical sense, and introduce the Gaussian disorder model that we will use throughout this thesis. In Sec. 3.3, we will introduce the concept of Green functions, which will turn out to be useful in order to perform the average over the disorder.

3.1 MODEL

3.1.1 *Schrödinger equation*

To describe the propagation of N non-interacting bosons in a 1D random correlated potential, we will use the single particle Hamiltonian:[1]

$$H = p^2 + V(x), \tag{15}$$

where p is the momentum operator and $V(x)$ is the random correlated potential, with correlation length σ_c. Note that, throughout this thesis,

1 If there is no interaction between the bosons, the wavefunction for N particles is a product of identical single-particle wavefunctions and its evolution is given by the single-particle Schrödinger equation.

we use units such that $\hbar = 2m = 1$. Then, we consider the Schrödinger equation

$$i\frac{\partial\psi}{\partial t} = H\psi = \Big(p^2 + V(x)\Big)\psi. \tag{16}$$

Eq. (16) exhibits solutions with constant energy E:

$$\psi(x,t) = \psi_E(x)e^{-iEt}, \tag{17}$$

and using this in Eq. (16), we obtain the stationary Schrödinger equation [37], [38]:

$$\Big(\partial_x^2 + E - V(x)\Big)\psi_E(x) = 0. \tag{18}$$

3.1.2 *Initial state*

As an initial trapped BEC state, we consider a Gaussian wave packet:

$$\psi_0(x) = \langle x|\psi_0\rangle = \left(\frac{1}{\pi a^2}\right)^{1/4} e^{-x^2/(2a^2)}, \tag{19}$$

where a is the initial width of the wave packet, which we assume to be much smaller than the localization length (see Chapter 5) in the relevant range of energies (see Chapter 6). For the numerical solution of the Gaussian wave packet propagation induced by Eq. (16), we use periodic bounday conditions, i. e., $\psi(x+L,t) = \psi(x,t)$ with system size $L \gg a, \sigma_c$.

Note that the works [27] and [28] discussed in Chapter 2 use a different initial state, where the interaction between the particles inside the harmonic trap, where the initial BEC is trapped, were considered. According to the Thomas-Fermi approximation (valid for large interactions), they considered a truncated inverted parabola as an initial density:

$$|\psi_{\mathrm{TF}}(x)|^2 = \left(\frac{\mu}{g}\right)[1 - (x/L_{\mathrm{TF}})^2], \tag{20}$$

where $L_{\mathrm{TF}} = \sqrt{2\mu/m\omega^2}$ denotes the Thomas-Fermi length, ω the harmonic trap frequency, m the atomic mass, g the strength of the interactions and μ the chemical potential. See Chapter 8 for a more detailed discussion.

As we already mentioned, our initial state, Eq. (19), that we will use throughout this thesis, does not include the interaction between the particles. For this reason, we may consider that all atoms from the non-interacting gas of bosons are described by the same Gaussian wave packet, which as an initial state is simpler than the inverted parabola and better suited for a rigorous theoretical analysis.

3.1.3 *Asymptotic density profile*

The BEC asymptotic state, assumed at long times t, is defined by:

$$n(x) = \lim_{T\to\infty} \frac{1}{T} \int_0^T \mathrm{d}t\; n(x,t), \tag{21}$$

where

$$n(x,t) = |\langle x|e^{-iHt}|\psi_0\rangle|^2, \tag{22}$$

denotes the density at position x and time t.

It is useful to write $n(x)$ in terms of the eigenfunctions $\{|\phi_n\rangle\}$ of Eq. (15). To do this, we use the relation $\sum_{n=0}^{\infty} |\phi_n\rangle\langle\phi_n| = \mathbb{1}$ in Eq. (22), leaving as a result:

$$n(x,t) = \sum_{n,m=0}^{\infty} \langle x|\phi_n\rangle\langle\phi_n|\psi_0\rangle\langle\psi_0|\phi_m\rangle\langle\phi_m|x\rangle e^{-i(E_m-E_n)t}. \tag{23}$$

Under the assumption of a non-degenerate energy spectrum $\{E_n\}$, the definition Eq. (21) applied to Eq. (23) is not zero only under the condition $m = n$. Thereby, we can conclude:

$$n(x) = \sum_{n=0}^{\infty} |\langle x|\phi_n\rangle\langle\phi_n|\psi_0\rangle|^2. \tag{24}$$

3.2 RANDOM POTENTIALS

It remains to characterize the random potential $V(x)$ in Eq. (15). In principle $V(x)$ could be also a random function of time, but along this thesis, we will consider only quenched or time independent disordered potentials.

The random nature of $V(x)$ induces us to work with realizations, which are defined as different sets of particular outcomes of the various values of $V(x)$ for every position x [39]. Even though we do not know anything about one single potential realization, we can get a statistical characterization of the whole set of realizations, and thereby, obtain a probability function $P[V]$ to perform the statistical average for the relevant quantities, e. g., conductivity σ, probability density for a particle with a single energy state $n_E(x)$, probability density for a wave packet $n(x)$, etc. In general, for a quantity A, we define its average

$$\overline{A} = \int \mathrm{d}V\; A\; P[V], \tag{25}$$

where the overline in Eq. (25) represents the average over all realizations of the random potential.

3.2.1 *Correlation functions and cumulants*

Instead of finding $P[V]$ for Eq. (25), we can characterize the set of different realization of $V(x)$ through all the *moments* or *correlation functions* and *cumulants* [40]–[43]. This equivalent way of characerizing the disorder will be useful in the context of the diagrammatic multiple scattering series discussed below.

The *moments* or *correlation functions* are defined as:

$$C_n(x_1, x_2, ..., x_n) = \overline{V(x_1)V(x_2)...V(x_n)}, \tag{26}$$

where we assume that the moments exist. Assuming $\overline{V(x)} =$ constant, we can set through this thesis $\overline{V(x)} = 0$ by redefining the point of zero energy.

This assumption implies that the potential statistical properties do not depend on the position in the average potential realizations, and in this sense, the average potential is homogeneous. The potential homogeneity implies translational invariance. Mathematically, this means that the n-point correlator of Eq. (26) depends only on $n-1$ points, or:

$$C_n(x_1, x_2, ..., x_n) = C_n(x_1 + x_0, x_2 + x_0, ..., x_n + x_0), \tag{27}$$

for all $x_0 \in \mathbb{R}$.

If the potential value at position x_1 depends on the potential value at position x_2, then the potential is correlated. Otherwise, the potential is un-correlated and the second moment can be factorized like:

$$C_2(x_1, x_2) = \overline{V(x_1)} \times \overline{V(x_2)}. \tag{28}$$

This allows us to introduce the concept of *cumulants*, $K_n(x_1, x_2, ..., x_n)$, as the difference:

$$\begin{aligned}
K_2(x_1, x_2) &= C_2(x_1, x_2) - \overline{V(x_1)} \times \overline{V(x_2)}, \\
K_3(x_1, x_2, x_3) &= C_3(x_1, x_2, x_3) - \overline{V(x_1)V(x_2)} \times \overline{V(x_3)} - \\
&\quad \overline{V(x_1)V(x_3)} \times \overline{V(x_2)} - \overline{V(x_2)V(x_3)} \times \overline{V(x_1)} \\
K_4(x_1, x_2, x_3, x_4) &= C_4(x_1, x_2, x_3, x_4) - [14 \text{ diferent terms}] \\
... &= ...,
\end{aligned} \tag{29}$$

where the 14 different terms can be written as:

$(x_1x_2x_3)(x_4), (x_1x_2x_4)(x_3), (x_1x_3x_4)(x_2), (x_2x_3x_4)(x_1), (x_1x_2)(x_3x_4),$
$(x_1x_3)(x_2x_4), (x_1x_4)(x_2x_3), (x_1x_2)(x_3)(x_4), (x_1x_3)(x_2)(x_4), (x_1x_4)(x_2)(x_3),$
$(x_2x_3)(x_1)(x_4), (x_2x_4)(x_1)(x_3), (x_3x_4)(x_1)(x_2)$ and $(x_1)(x_2)(x_3)(x_4)$,

where $(x_1x_2x_3)(x_4) = \overline{V(x_1)V(x_2)V(x_3)} \times \overline{V(x_4)}$, etc.

Due to the choice $\overline{V(x)} = 0$, the cumulants K_2 and K_3 concide with the moments C_2 and C_3, respectively.

3.2.2 *Gaussian disorder*

The Gaussian disorder is defined as a stochastic process where all the cumulants K_n of order $n > 2$ vanish. Together with $\overline{V(x)} = 0$, this implies that all correlations C_n of odd n-order also vanish.

On the other side, by expanding all correlation functions with even order into products of C_2-functions, a Gaussian stochastic process is *completely* characterized by $\overline{V(x)} = 0$ and $C_2(x_1, x_2)$. Using translational invariance, see Eq. (27), we will write $C_2(x_1, x_2) = C_2(x_1 - x_2)$ in the following. As examples of two Gaussian disorder models, we have:

i) The Gaussian correlated disorder, which considers a Gaussian distribution as the two-point correlation function:

$$C_2(x) = V_0^2 e^{-|x|^2/(2\sigma_c^2)}, \tag{30}$$

where V_0 is the strength of the random potential, and σ_c is the correlation length. Figs. (8a) and (8b) show an example of a numerically generated realization of a random potential with this correlation function.

The numerical implementation to create a potential with a Gaussian correlation function – Eq. (30) – requires to create a set of random numbers $\{a_i\}$, where $i = 0, 1, 2, ..., N_L$ and N_L is the number of lattice points, for every lattice point i. The set of random numbers follows a Gaussian probability distribution:

$$P(a_i) = \frac{1}{V_0\sqrt{2\pi}} e^{-a_i^2/(2V_0^2)}, \tag{31}$$

independently for each i.

Once we have the set of random numbers, we convolute it with a Gaussian envelope:

$$V(x) = \int \mathrm{d}x' \, \frac{v(x')}{N_x} e^{-|x-x'|^2/\sigma_c^2}, \tag{32}$$

where

$$v(x) = \sum_{i=0}^{N_L} a_i \delta(x - i\Delta x), \tag{33}$$

the normalization factor

$$N_x = \sigma\sqrt{2\pi}/(2\Delta x), \tag{34}$$

and Δx is the lattice spacing in x direction.

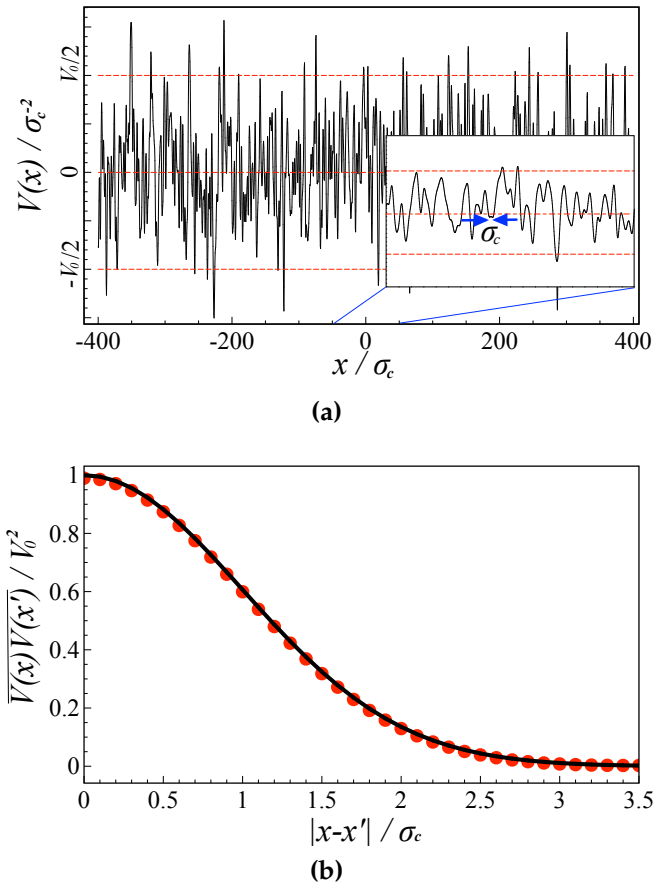

Fig. (8) (a) An example of a one-dimensional Gaussian correlated potential with correlation function as defined by Eq. (30), with strength V_0 and correlation length σ_c. The potential (in units of σ_c^{-2}) is plotted as a function of the position (in units of σ_c) in the interval $[-400, 400]\sigma_c$. The inset illustrates the scale of the correlation length σ_c (between the blue arrows) in comparison with the total potential length in the interval $[-50, 50]\sigma_c$. **(b)** Comparison between the numerical (red points) and analytical (black line) one-dimensional Gaussian correlation functions. The numerical correlation function was obtained by averaging over 2000 disordered potential realizations. The dimensionless quantity $\overline{V(x)V(x')}/V_0^2$ is shown as a function of the distance $|x - x'|$ (in units of σ_c).

ii) The white noise disorder, which considers a delta distribution as the two-point correlation function [44]–[46]:[2]

$$C_2(x) = D\delta(x), \tag{35}$$

2 This model can be used as a mathematical idealization under the assumption that the correlation length is smaller than the wavelength $\gamma_E = 2\pi/k_E$ of the quantum particle.

where $D = \int \mathrm{d}x\, C_2(x)$ parametrizes the potential strength. According to Eq. (35), the correlation length between two different positions is zero.

3.2.3 *Speckle potentials*

The Gaussian disorder model is analytically easier to treat than the speckle potentials, but its experimental implementation is more difficult. This fact is not unknown for the experimentalists, and for this reason, speckle potentials were used in the experimental setups discussed in Sec. 2.1. Although we will rely on the Gaussian model in this thesis, it is therefore convenient to introduce some important features of the mathematical description of the speckle potentials in the present section.

The experimental advantage of the speckle potential is its simple optical implementation to produce a random landscape [47]–[51]. The physical mechanism behind a speckle pattern is the superposition of different waves with random phases. The setup to achieve this experimental superposition consists basically of a plane wave or laser beam which passes trough a diffusive lens. The Huygens principle then asserts that the lens behaves as a source of N_i independent partial waves, with amplitudes E_j and phases ϕ_j, which has as total amplitude:

$$E = \frac{1}{\sqrt{N_i}} \sum_{j=1}^{N_i} |E_i| e^{i\phi_j}. \tag{36}$$

The partial waves thus create a random interference pattern, see Fig. (9).

Due the irregular form of the lens, we can assume that the amplitudes E_j and phases ϕ_j are uncorrelated, and the phases are uniformly distributed in the interval $[0, 2\pi]$. Under this conditions, in the limit $N_i \to \infty$, the central limit theorem ensures that the real and imaginary part of E in Eq. (36) have Gaussian statistics. Nevertheless, the interference pattern depends on the absolute square $I = |E|^2$ of Eq. (36), and the absolute square of a Gaussian field does not fulfill the Gaussian properties.

Notwithstanding that the speckle potential is different from the Gaussian model that we will use in our analytic model, in the theories presented in Chapter. 2, the non-Gaussian character of the speckle is not relevant, since they use the Born approximation (i. e. higher moments than second order do not appear). One of our goals in this thesis is to go beyond the Born approximation. For this purpose, it is useful to study first the case of Gaussian potentials since this is more practical for developing an exact theory.

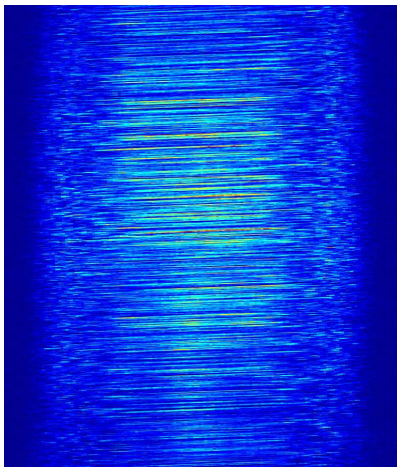

Fig. (9) Experimental one-dimensional speckle pattern. A laser beam illuminates a diffusive plate producing different electromagnetic fields. Therefore, the superposition of the various fields produces an interference pattern (blue: minimum and red: maximum) known as speckle potential. Image from [52].

The last point to illustrate is the second order correlation function of a one-dimensional speckle potential, which is given by [52]:

$$C_2(z) = V_0^2 \frac{\sin^2(z/\sigma_c)}{(z/\sigma_c)^2}. \tag{37}$$

Moreover, its Fourier transform is:

$$C_2(p_E) = \begin{cases} V_0^2 \sqrt{\frac{\pi}{2}} \sigma_c \left(1 - p_E \sigma_c\right), & \text{if } p_E \sigma_c < 1, \\ 0, & \text{if } p_E \sigma_c \geq 1. \end{cases} \tag{38}$$

Note the finite support of the Fourier transform, which we already mentioned in Subs. 2.2.1.

3.3 GREEN FUNCTION

For any initial state $|\psi_0\rangle = |\psi(t=0)\rangle$ which evolves in a closed system, the time evolution is described by the unitary evolution operator $U(t)$:

$$U(t) = e^{-iHt}, \tag{39}$$

where H is given by Eq. (15). Thereby, the state $|\psi(t)\rangle$ at time t is:

$$|\psi(t)\rangle = U(t)|\psi_0\rangle = e^{-iHt}|\psi_0\rangle, \tag{40}$$

and in the spatial representation:

$$\psi(x,t) = \langle x|\psi(t)\rangle = \int \mathrm{d}x' \, \langle x|e^{-iHt}|x'\rangle \psi_0(x'). \tag{41}$$

The kernel of Eq. (41) is defined as the Green function [53]:

$$G(x,x',t) = \langle x|e^{-iHt}|x'\rangle, \tag{42}$$

or the Green operator:

$$G(t) = e^{-iHt}. \tag{43}$$

If $\{E_n\}$ and $\{\phi_n\}$ are respectively the eigenenergies and the eigenstates of H, then Eq. (42) can be expressed as:

$$G(x,x',t) = \langle x|e^{-iHt}|x'\rangle = \sum_n \phi_n(x)\phi_n^*(x')e^{-iE_nt}. \tag{44}$$

The variable t in Eqs. (43) and (44) is not positive or negative defined. Therefore, the evolution between $t = 0$ and $t > 0$, will be related with the Green funtion $G_0^{(+)}(x,x',t)$; while the evolution to $t < 0$, will be related with the Green funtion $G_0^{(-)}(x,x',t)$:

$$\begin{aligned} G^{(+)}(x,x',t) &= -i\theta(t)\langle x|e^{-iHt}|x'\rangle = -i\theta(t)\sum_n \phi_n(x)\phi_n^*(x')e^{-iE_nt}, \\ G^{(-)}(x,x',t) &= i\theta(-t)\langle x|e^{-iHt}|x'\rangle = i\theta(-t)\sum_n \phi_n(x)\phi_n^*(x')e^{-iE_nt}. \end{aligned} \tag{45}$$

With the goal to get the Green functions $G_0^{(+)}(x,x',t)$ and $G_0^{(-)}(x,x',t)$ in terms of the energy E instead of time t, we perform its Fourier transform:

$$G^{(\pm)}(x,x',E) = \int_{-\infty}^{\infty} \mathrm{d}t\; G^{(\pm)}(x,x',t)e^{-iEt}, \tag{46}$$

which leaves as a result:

$$G^{(\pm)}(x,x',E) = \sum_n \frac{\phi_n(x)\phi_n^*(x')}{E - E_n \pm i\eta}, \tag{47}$$

and in operator form [54]:

$$G^{(\pm)}(E) = \frac{1}{E - H \pm i\eta}, \tag{48}$$

with infinitesimal positive quantity η in Eqs. (47) and (48), which assures the convergence of the integrals in Eq. (46). For the free particle ($H_0 = p_E^2$) the Green function as operator is [54]:

$$G_0^{(\pm)}(E) = \frac{1}{E - H_0 \pm i\eta}. \tag{49}$$

Using Eqs. (48) and (49), we can construct the next derivation:

$$\begin{aligned}
[G^{(\pm)}(E)]^{-1}G^{(\pm)}(E) &= \mathbb{1}, \\
(E - H_0 - V)G^{(\pm)}(E) &= \mathbb{1}, \\
G_0^{(\pm)}(E)([G_0^{(\pm)}(E)]^{-1} - V)G^{(\pm)}(E) &= G_0^{(\pm)}(E), \\
G^{(\pm)}(E) - G_0^{(\pm)}(E)VG^{(\pm)}(E) &= G_0^{(\pm)}(E),
\end{aligned} \tag{50}$$

or

$$G^{(\pm)}(E) = G_0^{(\pm)}(E) + G_0^{(\pm)}(E)VG^{(\pm)}(E), \tag{51}$$

which is the *Lippmann-Schwinger* equation, yielding an iterative expansion to get the Green function related to the full Hamiltonian $H = H_0 + V(x)$. See Sec. 3.3.2.

The tools developed in this section will be used in this thesis in the following two powerful applications of the Green functions formalism: The Berezinskii method [20] to get the density-density autocorrelation function at fixed energy and to prove the ansatz Eq. (9) in Chapter 4, and Thouless' relation between localization length and density of states [23] in Chapter 5. But first, in the next subsections, we will deduce the Green function as function of the space variable x.

3.3.1 *Free particle Green function*

For the free particle in a one-dimensional box with length L, the eigenenergies and eigenstates of H_0 are respectively $\{E_n = p_n^2\}$ and $\{\phi_n(x) = e^{-ip_n x}/\sqrt{L}\}$, where $p_n = 2\pi n/L$, with $n = \pm 1, \pm 2, \ldots$. If $L \to \infty$, then the sum in Eq. (47) becomes an integral over n [55]:

$$G_0^{(\pm)}(x, x', E) = \frac{1}{L}\int \mathrm{d}n\, \rho(n) \frac{e^{-ip_n(x-x')}}{E - p_n^2 \pm i\eta} = \frac{1}{2\pi}\int_{-\infty}^{\infty} \mathrm{d}p\ \frac{e^{-ip(x-x')}}{E - p^2 \pm i\eta}, \tag{52}$$

where we have used the relation between p_n and E_n, and based on the same relation, the density is $\rho(n) = dp/dn = 2\pi/L$. From the relation Eq. (52) we can conclude that the Green functions $G_0^{(\pm)}(x, x', E)$ depend on the difference $x - x'$, therefore, henceforth, we may also write $G_0^{(\pm)}(x - x', E)$. Based on this property, the Fourier transform of $G_0^{(+)}(x - x', E)$ is:

$$\begin{aligned}
\tilde{G}_0^{(+)}(p, p', E) &= \frac{1}{2\pi}\int \mathrm{d}x\mathrm{d}x'\ e^{-ipx+ip'x'} G_0^{(+)}(x - x', E), \\
&= \frac{1}{2\pi}\int \mathrm{d}x'\mathrm{d}x''\ e^{-ip(x'+x'')+ip'x'} G_0^{(+)}(x'', E), \\
&= \tilde{G}_0^{(+)}(p, E)\delta(p - p'),
\end{aligned} \tag{53}$$

where we defined:

$$\begin{aligned}\tilde{G}_0^{(+)}(p,E) &= \int_{-\infty}^{\infty} \mathrm{d}x\, e^{ipx} G_0^{(+)}(x,E), \\ &= \frac{1}{E-p^2+i\eta}. \end{aligned} \tag{54}$$

The delta function in Eq. (53) is an evidence of momentum conservation. In order to perform the integral in Eq. (52), and thereby to get an expression for the Green functions in position space, we use the following relation:

$$\frac{1}{A-B^2} = \frac{1}{2\sqrt{A}}\left[\frac{1}{\sqrt{A}+B} + \frac{1}{\sqrt{A}-B}\right], \tag{55}$$

where $A = E \pm i\eta$ and $B = p$, then:

$$G_0^{(\pm)}(x-x',E) = \frac{1}{4\pi\sqrt{E\pm i\eta}} \int_{-\infty}^{\infty} \mathrm{d}p \left[\frac{e^{-ip(x-x')}}{\sqrt{E\pm i\eta}+p} + \frac{e^{-ip(x-x')}}{\sqrt{E\pm i\eta}-p}\right]. \tag{56}$$

The difference between $x - x'$ can be positive or negative. If we choose $x - x' > 0$ ($x - x' < 0$), then, using the calculus of residues and Cauchy's integral theorem, the integral is:

$$G_0^{(\pm)}(x,x',E) = \mp\frac{i}{2p_E} e^{\pm ip_E|x-x'|}, \tag{57}$$

where $p_E = \sqrt{E \pm i\eta}$ [53].

The question is now how to get the average Green function associated to a set of Hamiltonians given by Eq. (15). The solution of the Dyson equation will answer this question, but first, we will come back to the Lippmann-Schwinger equation [56].

3.3.2 *Lippmann-Schwinger equation and Born series*

Eq. (51) reads in position space:

$$\begin{aligned} G^{(+)}(x,x',E) = G_0^{(+)}(x,x',E) \\ + \int \mathrm{d}x''\; G_0^{(+)}(x,x'',E) V(x'') G^{(+)}(x'',x',E). \end{aligned} \tag{58}$$

Introducing the following symbols:

$G^{(+)}(x,x',E)$:

$G_0^{(+)}(x,x',E)$:

$V(x)$: 

Eq. (58) reads:

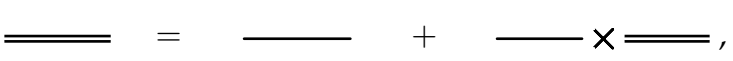

(59)

where the last term includes an integral over the intermediate variables that connect, via the potential, two different Green functions. The iterative solution of Eq. (59) lead us to the Born series for any potential:

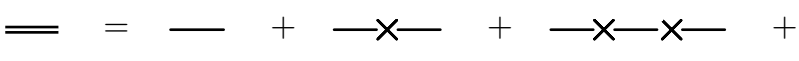

(60)

or

$$
\begin{aligned}
&G^{(+)}(x,x',E) = G_0^{(+)}(x,x',E) \\
&+ \int \mathrm{d}x''\; G_0^{(+)}(x,x'',E)V(x'')G_0^{(+)}(x'',x',E) \\
&+ \int \mathrm{d}x''\mathrm{d}x'''\; G_0^{(+)}(x,x'',E)V(x'')G_0^{(+)}(x'',x''',E)V(x''')G_0^{(+)}(x''',x',E) \\
&+ \ldots
\end{aligned}
\tag{61}
$$

The Born series expresses the Green function associated to the potential $V(x)$ as a sum over scattering paths. The latter consist of free propagations G_0 interrupted by scattering events V. Due to the free propagation, see Eq. (57), each scattering path carries a phase factor $e^{ip_E|x-x_1|}e^{ip_E|x_2-x_1|}\ldots e^{ip_E|x_n-x'|}$ depending on the positions $x_1, x_2, \ldots, x_n$ of the scattering events.

3.3.3 *Average Green function: Dyson equation*

Averaging the Lippmann-Schwinger equation for Gaussian disorder

As we introduced earlier, see Sec. 2.2, a disorder potential which follows Gaussian statistics is completely characterized by the first and the second moment, i. e., all the even statistical moments can be expressed in terms of:

$$
\overline{V(x)} = 0, \quad \text{and} \quad C_2(x-x') = \overline{V(x)V(x')}, \tag{62}
$$

while all the odd moments are zero, since $\overline{V(x)} = 0$. As an example, the fourth moment $\overline{V(x_1)V(x_2)V(x_3)V(x_4)}$, can be factorized to a sum of the product of two point correlators:

$$
\begin{aligned}
\overline{V(x_1)V(x_2)V(x_3)V(x_4)} = C_2(x_1-x_2)C_2(x_3-x_4) + C_2(x_1-x_3)\times \\
C_2(x_2-x_4) + C_2(x_1-x_4)C_2(x_2-x_3),
\end{aligned}
\tag{63}
$$

or in diagrammatic notation:

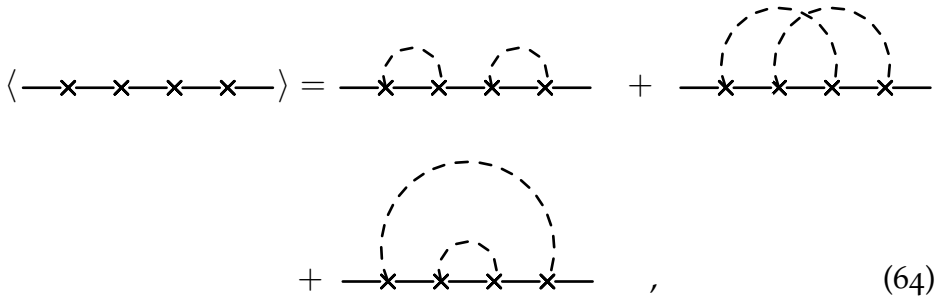

(64)

where $\langle \cdots \rangle$ is equivalent to $\overline{\cdots}$, i. e., both notations represent an average over the disordered potentials of the stochastic process. The dashed lines represent the correlation function $C_2(x - x')$. Therefore, taking the average of Eq. (58), or diagrammatically Eq. (60), we must in the following introduce the Dyson equation.

We now perform the disorder average of Eq. (60), and to do this, let us define the *self energy* $\Sigma^{(+)}(x, x', E)$, as a function that represents the disorder-averaged sum of all the irreducible diagrams, which are those non-factorizable in more than one term, if we cut one of its Green functions. The second and third term on the right-hand side of Eq. (64) are examples of non-factorizable terms, whereas the first one can be factorized by cutting the Green function connecting x_2 and x_3. The first few diagrams for the self-energy are [56]:

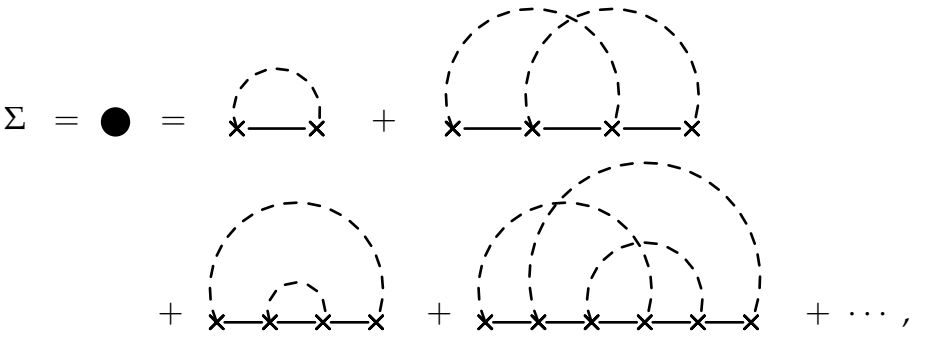

(65)

where the equation for the first two terms reads:

$$\begin{aligned}\Sigma^{(+)}(x, x', E) =& C_2(x - x')G_0^{(+)}(x, x', E) + \\ & \int \mathrm{d}x_1 \mathrm{d}x_2 \; C_2(x - x_2)C_2(x_1 - x') \times \\ & G_0^{(+)}(x, x_1, E)G_0^{(+)}(x_1, x_2, E)G_0^{(+)}(x_2, x', E) + \cdots\end{aligned} \tag{66}$$

The self-energy is a complex function, and in general, its imaginary part must be negative, since the negative imaginary part of the Green

function is proportional to the density of states, which is a positive quantity, see Eq. (178). With the self-energy and the disorder average, we obtain an equation that describes how a wave propagates on average in a Gaussian random potential. The propagation on average is given by an average Green function, which fulfills the Dyson equation:

$$\overline{G^{(+)}(x,x',E)} = G_0^{(+)}(x,x',E) + \int \mathrm{d}x''\mathrm{d}x'''\; G_0^{(+)}(x,x'',E)\Sigma^{(+)}(x'',x''')\overline{G^{(+)}(x''',x',E)}, \tag{67}$$

or in diagrammatic notation:

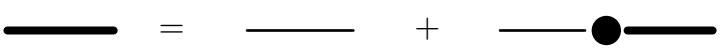

(68)

where the thick line represents the average Green function.

The average Green function

The solution of Eq. (67) yields the average Green function, and to find it easily, we transform the Dyson equation into momentum representation. As we already commented in Sec. 2.2, under the assumption that the statistical properties of the potential are translationally invariant, Eq. (27), we assume also that the self-energy depends only on the difference $x - x'$:

$$\Sigma(x,x') = \Sigma(x-x'), \tag{69}$$

therefore, as well as the free particle Green function, the self-energy conserves momentum:

$$\begin{aligned}\widetilde{\Sigma}(p,p') &= \frac{1}{2\pi}\int \mathrm{d}x\mathrm{d}x'\; e^{-ipx+ip'x'}\Sigma(x-x'),\\ &= \frac{1}{2\pi}\int \mathrm{d}x'\mathrm{d}x''\; e^{-ip(x'+x'')+ip'x'}\Sigma(x''),\\ &= \widetilde{\Sigma}(p)\delta(p-p'),\end{aligned} \tag{70}$$

where we used $\int \mathrm{d}x\; e^{ipx} = 2\pi\delta(p)$. The delta function in Eq. (70) is an evidence of momentum conservation.

Considering the double Fourier transform on both sides of Eq. (67), and using Eqs. (53) and (70), we get the Dyson equation in momentum representation:

$$\overline{\tilde{G}^{(+)}(p,p',E)} = \tilde{G}_0^{(+)}(p,E)\delta(p-p') + \tilde{G}_0^{(+)}(p,E)\tilde{\Sigma}(p,E)\overline{\tilde{G}^{(+)}(p,p',E)}. \tag{71}$$

Due to the property of momentum conservation, from Eq. (71) we may deduce:

$$\overline{\tilde{G}^{(+)}(p,p',E)} = \overline{\tilde{G}^{(+)}(p,E)}\delta(p-p'), \tag{72}$$

thereby, the average Green function also fulfils the momentum conservation and the Dyson equation in momentum space, Eq. (71), simplifies to:

$$\overline{\tilde{G}^{(+)}(p,E)} = \tilde{G}_0^{(+)}(p,E) + \tilde{G}_0^{(+)}(p,E)\tilde{\Sigma}(p,E)\overline{\tilde{G}^{(+)}(p,E)}. \tag{73}$$

The solution of Eq. (73) is:

$$\overline{\tilde{G}^{(+)}(p,E)} = \frac{1}{E - p^2 - \tilde{\Sigma}^{(+)}(p,E)}. \tag{74}$$

Assuming a weak random potential (and, correspondingly, small Σ), we see that the main contribution to $\overline{\tilde{G}^{(+)}(p,E)}$ originates from momenta $p \simeq p_E = \sqrt{E}$, where the term $E - p^2$ in the denominator of Eq. (65) vanishes. We hence neglect the momentum dependence of the self-energy, i. e., we replace Eq. (74) by:

$$\overline{\tilde{G}^{(+)}(p,E)} = \frac{1}{E - p^2 - \Sigma^{(+)}(E)}, \tag{75}$$

where:

$$\Sigma^{(+)}(E) = \tilde{\Sigma}^{(+)}(p_E,E). \tag{76}$$

The average Green function then takes the following form in position space:

$$\overline{G^{(+)}(x_1 - x_2, E)} = -\frac{i}{\tilde{p}_E} e^{i\tilde{p}_E|x_1 - x_2|}, \tag{77}$$

which is similar to the free-particle Green function where $p_E = \sqrt{E}$, Eq. (57), but with complex effective wave vector

$$\tilde{p}_E = \sqrt{E - \Sigma^{(+)}(E)} \tag{78}$$

instead of p_E.

If we define $\tilde{p}_E = \Re\{\tilde{p}_E\} + i\Im\{\tilde{p}_E\}$, then, taking $|\overline{G^{(+)}(x_1 - x_2, E)}|^2$, we find:

$$|\overline{G^{(+)}(x_1 - x_2, E)}|^2 = \frac{e^{-2\Im\{\tilde{p}_E\}|x_1 - x_2|}}{\Re\{\tilde{p}_E\}^2 + \Im\{\tilde{p}_E\}^2}. \tag{79}$$

These results can be interpreted as follows: the random medium forms an average effective medium, which has refractive index:

$$n_E = \frac{\tilde{p}_E}{p_E}, \tag{80}$$

where its imaginary part defines the scattering mean free path:

$$\ell = \frac{1}{2p_E \Im\{n_E\}}. \tag{81}$$

as the average distance between two subsequent scattering events. Combining Eqs. (79–81) we can conclude:

$$|\overline{G^{(+)}(x_1 - x_2, E)}|^2 = \frac{e^{-|x_1 - x_2|/\ell}}{\Re\{\tilde{p}_E\}^2 + \Im\{\tilde{p}_E\}^2}, \tag{82}$$

implying that the propagation of the average amplitude decays exponentially. The average Green function will be used in Chapter 6 in order to determine the spectral function.

Mean free path in Born approximation

In the Born approximation, the self-energy is approximated by the first term of the Eq. (75), i. e.

$$\begin{aligned} \Sigma^{(+)}_{\text{Born}}(x, x', E) &= C_2(x - x') G_0^{(+)}(x, x', E), \\ &= -\frac{i}{p_E} C_2(x - x') e^{i p_E |x - x'|}, \end{aligned} \tag{83}$$

$$\tag{84}$$

where we used Eq. (57). The Fourier transform yields:

$$\Sigma^{(+)}_{\text{Born}}(E) = \widetilde{\Sigma}^{(+)}_{\text{Born}}(p_E, E) = -\frac{i}{p_E} \int_{-\infty}^{\infty} \mathrm{d}x \; C_2(x) e^{i p_E (x + |x|)}. \tag{85}$$

According to Eq. (78), we get (for $|\Sigma^{(+)}(E)| \ll E$):

$$\Im\{\tilde{p}_E\} \approx -\frac{\Im\{\Sigma^{(+)}(E)\}}{2p_E}, \tag{86}$$

which finally yields, see Eqs. (80,81), the inverse of the scattering mean free path in Born approximation:

$$\frac{1}{\ell_{\text{Born}}} = \frac{1}{p_E^2} \int_0^{\infty} \mathrm{d}x \; C_2(x) \left[1 + \cos(2p_E x)\right]. \tag{87}$$

4

DIAGRAMMATIC CALCULATION OF THE ASYMPTOTIC DENSITY PROFILE

In Subs. 3.3.3, we have seen that, under the assumption of a weak random potential, the average Green function decays exponentially in position space, see Eq. (82), where the rate of this decay defines the scattering mean free path ℓ, see Eq. (81). In order to calculate our quantity of interest, the average asymptotic density profile $\overline{n(x)}$ defined in Subs. 3.1.3, see Eq. (24), the knowledge of the average Green function is, however, not sufficient, since, as shown below, this quantity involves the average of a product of two Green functions. We will therefore introduce in this chapter a diagrammatic method for performing this average that will finally lead us to Eq. (9) – the same equation that, as discussed in Subs. 2.2.3, has already been introduced as a heuristic ansatz in previous works [27], [28], [34].

The diagrammatic method that we will use to calculate $\overline{n(x)}$ has been invented by Berezinskii in 1974 [20]. He developed this method in order to determine the density-density autocorrelation function $\overline{n_E(x)}$ at fixed energy E introduced in Eq. (3). As explained in Subs. 2.2.2, this function does not only describe the exponential decay of energy eigenfunctions at large distances, but also corrections to this exponential decay relevant for small distances.

We will review Berezinskii's calculation of $\overline{n_E(x)}$ in Sec. 4.1. Then, we will modify his method in order to determine $\overline{n(x)}$ in Sec. 4.2. As we will see, this involves an integration of $\overline{n_E(x)}$ over the energy E, weighted with a suitably defined energy distribution depending on the intial state $\psi_0(x)$ of the wavepacket at time $t = 0$.

4.1 DENSITY-DENSITY AUTOCORRELATION FUNCTION AT FIXED ENERGY: METHOD OF BEREZINSKII

We give in this section a short introduction into the diagrammatic method of Berezinskii. The technique was originally developed in [20] for a one-dimensional white noise potential, and later extended by Gogolin to the case of correlated random potentials with short correlation length [21], [22]. As in these original works, we consider an infinitely extended system (without periodic boundary conditions).

4.1.1 *Average intensity propagator*

To start with, we recall the definition of the density-density autocorrelation function $\overline{n_E(x)}$ at fixed energy, see Eq. (3). Let us define the following quantity, which is almost the same as Eq. (3), but without ensemble average in the numerator:

$$n_E(x,x') = \sum_{n=0}^{\infty} |\phi_n(x)|^2 |\phi_n(x')|^2 \delta(E_n - E)/\overline{\rho_E}. \tag{88}$$

Eq. (88) describes the product of the densities $|\psi(x)|^2$ and $|\psi(x')|^2$ at points x and x', respectively, for an eigenstate $|\phi_n\rangle$ with energy $E_n = E$.

As explained in Subs. 2.2.2, the average density of states $\overline{\rho_E}$ appearing in the denominator serves as a normalization factor. It will be determined at the end of the calculation by the condition that the state $\overline{n_E(x-x')}$ be normalized on average. The ensemble average product of densities $\overline{n_E(x-x')}$ (which due to statistical translational invariance, depends only on the difference $x - x'$) describes the (normalized) density-density autocorrelation function.

The diagrammatic method relies on the fact that Eq. (88) can be expressed as follows:

$$\begin{aligned} n_E(x,x') &= \lim_{\omega\to 0} \frac{\omega}{2\pi i \overline{\rho_E}} G^{(+)}(x,x',E+\omega) \\ &\quad \times \Big(G^{(-)}(x',x,E) - G^{(+)}(x',x,E) \Big), \end{aligned} \tag{89}$$

in terms of retarded and advanced Green functions:

$$G^{(\pm)}(x,x',E) = \langle x|[E - H \pm i\eta]^{-1}|x'\rangle, \tag{90}$$

introduced in Sec. 3.3, see Eq. (48). The equivalence of Eqs. (88) and (89) is proven in Appendix A.

Taking the disorder average of Eq. (89), the product of two retarded Green functions can be assumed to vanish due to the random phase of $G^{(+)}(x,x',E)$, see the discussion after Eq. (61). In contrast, the product of a retarded and an advanced Green function survives the disorder average since the phases of $G^{(+)}(x,x',E+\omega)$ and $G^{(-)}(x',x,E)$ compensate each other (in the limit $\omega \to 0$) in each single realization of the random potential. This leads to:

$$\overline{n_E(x-x')} = \lim_{\omega\to 0} \frac{\omega}{2\pi i \overline{\rho_E}} \overline{G^{(+)}(x,x',E+\omega) G^{(-)}(x',x,E)}. \tag{91}$$

We therefore introduce the average intensity propagator:

$$\Phi(x,x',E,\omega) = \overline{G^{(+)}(x,x',E+\omega) G^{(-)}(x',x,E)}, \tag{92}$$

in terms of which the density-density autocorrelation function at fixed energy reads:

$$\overline{n_E(x-x')} = \lim_{\omega\to 0} \frac{\omega}{2\pi i \overline{\rho_E}} \Phi(x, x', E, \omega). \tag{93}$$

4.1.2 *Essential diagrams*

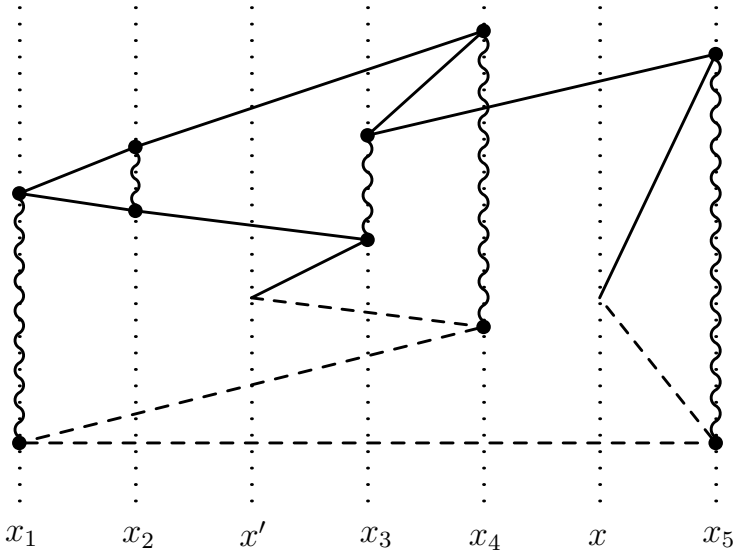

Fig. (10) Example of a diagram which contributes to the average intensity propagator $\Phi(x, x', E, \omega) = \overline{G^{(+)}(x, x', E+\omega)G^{(-)}(x', x, E)}$ in Berezinskii's approach. The solid (or dashed) lines represent free-particle Green functions $G_0^{(+)}(E+\omega)$ (or $G_0^{(-)}(E)$), respectively. The dots connected by vertical wavy lines denote the two-point correlation function of the random potential.

In order to represent the average intensity propagator in terms of diagrams, the Green functions are expanded in powers of the random potential V:

$$G^{(\pm)}(E) = G_0^{(\pm)}(E) + G_0^{(\pm)}(E) V G_0^{(\pm)}(E) + \ldots, \tag{94}$$

with free-particle Green functions $G_0^{(\pm)}(E)$, see Eq. (51). This expansion results from the iterative solution of the Lippmann-Schwinger equation, Eq. (58).

Thus, the Green functions $G^{(+)}(E)$ and $G^{(-)}(E)$ are written as a sum of infinitely many terms, each of which can be represented as a diagram, where retarded (advanced) Green functions are represented, e. g., by solid (dashed) lines, and the random potential V by a dot. Performing the disorder average of the product $G^{(+)}(E+\omega)G^{(-)}(E)$, dots be-

come connected by wavy lines indicating two-point correlation functions of the random potential (also called 'vertices' in the following). An example of such a diagram contributing to the average product $\overline{G^{(+)}(E+\omega)G^{(-)}(E)}$ is given in Fig. (10).

To clarify the diagrammatic notation, we first give the explicit expression of the diagram shown in Fig. (10):

$$\begin{aligned}
&\Phi^{(\mathrm{F10})}(x,x',E,\omega) = \\
&\int_{-\infty}^{x'} \mathrm{d}x_1 \int_{-\infty}^{x'} \mathrm{d}x_1' \int_{x_1}^{x'} \mathrm{d}x_2 \int_{x_1'}^{x'} \mathrm{d}x_2' \int_{x'}^{x} \mathrm{d}x_3 \int_{x'}^{x} \mathrm{d}x_3' \int_{x_3}^{x} \mathrm{d}x_4 \int_{x_3'}^{x} \mathrm{d}x_4' \times \\
&\int_{x}^{\infty} \mathrm{d}x_5 \int_{x}^{\infty} \mathrm{d}x_5' \; G_0^{(+)}(x_3 - x', E+\omega) \; G_0^{(+)}(x_2 - x_3, E+\omega) \times \\
&G_0^{(+)}(x_1 - x_2, E+\omega) \; G_0^{(+)}(x_2 - x_1, E+\omega) \; G_0^{(+)}(x_4 - x_2, E+\omega) \times \\
&G_0^{(+)}(x_3 - x_4, E+\omega) \; G_0^{(+)}(x_5 - x_3, E+\omega) \; G_0^{(+)}(x \;\; - x_5, E+\omega) \times \\
&G_0^{(-)}(x_4' - x', E) \; G_0^{(-)}(x_1' - x_4', E) \; G_0^{(-)}(x_5' - x_1', E) \; G_0^{(-)}(x - x_5', E) \times \\
&C_2(x_1 - x_1') \; C_2(x_2 - x_2') \; C_2(x_3 - x_3') \; C_2(x_4 - x_4') \; C_2(x_5 - x_5'). \quad (95)
\end{aligned}$$

The superscript '(F10)' reminds us that this term corresponds to the diagram shown in Fig. (10). Similarly to Eq. (95), we can express each diagram contributing to the average product Φ of Green functions in terms of free-particle Green functions $G_0^{(\pm)}$, see Eq. (57), and two-point correlation functions C_2 of the random potential, see Subs. 3.2.1. Note that, for simplicity, the points $x_1', \ldots, x_5'$ are not indicated in Fig. (10). For the case of short-range correlations (i. e. small correlation length σ_c), which we will assume in the following, these points are very close to the points $x_1, \ldots, x_5$, with which they are correlated.

We now break up each Green function into two factors associated with the respective points connected by the Green function, e. g.

$$G_0^{(-)}(x_4' - x', E) = \left(\frac{i}{2p_E}\right)^{1/2} e^{-ip_E x_4'} \times \left(\frac{i}{2p_E}\right)^{1/2} e^{ip_E x'} \qquad (96)$$

for $x_4' > x'$. We then perform the integrals over $x_1', \ldots, x_5'$. Assuming a small correlation length σ_c, we may extend the limits of these integrations to $\pm\infty$. For small ω, Eq. (95) then turns into:

$$\begin{aligned}
\Phi^{(\mathrm{F10})}(x,x',E,\omega) = \frac{e^{-i\omega\frac{x+x'}{2p_E}}}{4p_E^2} \int_{-\infty}^{x'} \mathrm{d}x_1 \int_{x_1}^{x'} \mathrm{d}x_2 \int_{x'}^{x} \mathrm{d}x_3 \int_{x_3}^{x} \mathrm{d}x_4 \int_{x}^{\infty} \mathrm{d}x_5 \\
\times \frac{e^{-i\omega x_1/p_E}}{\ell_-} \left(-\frac{1}{\ell_+}\right) \left(-\frac{1}{\ell_-}\right) \frac{e^{i\omega x_4/p_E}}{\ell_-} \frac{e^{i\omega x_5/p_E}}{\ell_-}, \quad (97)
\end{aligned}$$

where the mean free paths ℓ_+ (for forward scattering) and ℓ_- (for backward scattering) are introduced as follows:

$$\frac{1}{\ell_+} = \frac{1}{2p_E^2}\int_0^\infty \mathrm{d}x\; C_2(x) \tag{98a}$$

$$\frac{1}{\ell_-} \pm \frac{i}{\ell_0} = \frac{1}{2p_E^2}\int_0^\infty \mathrm{d}x\; C_2(x) e^{\pm 2ip_E x} \tag{98b}$$

Note that the sum of the inverse mean free paths $1/\ell_\pm$ yields the inverse of the scattering mean free path in Born approximation, see Eq. (87) in Subs. 3.3.3:

$$\frac{1}{\ell_{\mathrm{Born}}} = \frac{1}{\ell_+} + \frac{1}{\ell_-}. \tag{99}$$

Moreover, as we will see later, the inverse of the backscattering mean free path

$$\frac{1}{\ell_-} = 2\gamma_{\mathrm{Born}}(E), \tag{100}$$

yields two times the Lyapunov exponent in Born approximation, see Eq. (143).

The next important approximation consists of assuming that – similar to the neglect of $\overline{G^{(+)}(E+\omega)G^{(+)}(E)}$ discussed above – only those diagrams survive the disorder average where the phase factors associated with the free-particle Green functions exactly compensate each other in the limit $\omega \to 0$. This is the case if each space interval between neighbouring vertices contains the same number of retarded and advanced Green functions. In Fig. (10), for example, there are two solid and two dashed lines between the points x_2 and x', whereas there are three solid and three dashed lines between x' and x_3, etc. In the corresponding equation, see Eq. (97), we see that all phases appearing in the exponents vanish in the limit $\omega \to 0$. We will call a diagram of this type 'essential diagram'.

4.1.3 *Summation of essential diagrams*

After these introductory steps, the main part of Berezinskii's paper is concerned with performing the sum over all these diagrams, which yields the desired analytical expression for $\overline{n_E(x-x')}$. For this purpose, we first note that all essential diagrams contributing to the average intensity propagator Φ can be systematically constructed in terms of certain elementary vertices displayed in Fig. (11). In the above example, Fig. (10), a vertex of type f) is present at x_1, b) at x_2, c) at x_3 and e) at x_4 and x_5. In the second line of Eq. (97), we recognize the terms accociated

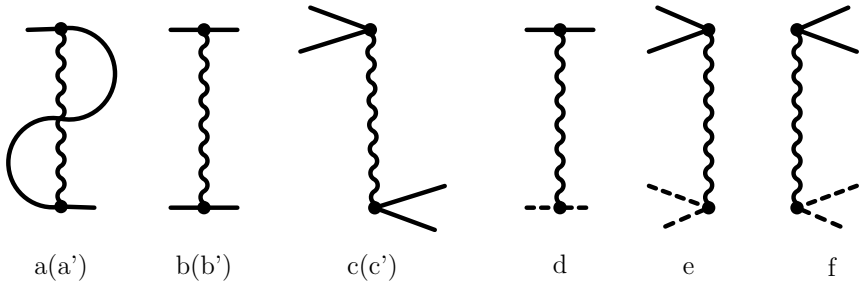

Fig. (11) Types of vertices entering in the essential diagrams for the average intensity propagator [21]. Solid (dashed) lines represent $G_0^{(\pm)}$, whereas two dots connected by a wavy line denote the two-point correlation function C_2. Diagrams (a',b',c') are the same as (a,b,c), but with solid lines replaced by dashed lines. The vertices correspond to the following factors: a) $-1/2\ell_- - 1/2\ell_+ - i/2\ell_0$, a') $-1/2\ell_- - 1/2\ell_+ + i/2\ell_0$ b,b') $-1/\ell_+$, c,c') $-1/\ell_-$, d) $1/\ell_+$, e) $e^{i\omega y/p_E}/\ell_-$, f) $e^{-i\omega y/p_E}/\ell_-$.

to each of these vertices. Additionally, Eq. (97), also contains the factors associated to the initial and final points x' and x.

Let us now assume $x > x'$. In each essential diagram, we then distinguish the following three parts: the left-hand part lying to the left of x', the right-hand part lying to the right of x, and the central part between x' and x. Note that the left and right parts always contain an even number of solid (and of dashed) lines, and the central part an odd number. We define $\tilde{R}_m(x)$ ($\tilde{L}_{m'}(x)$) as the sum of all right-hand (left-hand) diagrams containing $2m$ ($2m'$) solid and dashed lines at the boundary with the central part. Similarly, $Z_{m',m}(x',x)$ denotes the sum of all central parts with $2m+1$ ($2m'+1$) solid and dashed lines at the boundary with the right-hand (left-hand) part. The factors corresponding to the points x and x' are treated separately and not included in $\tilde{R}$, Z, or $\tilde{L}$. With this convention (which is slightly different from the one in Berezinskii's paper, where these factors are partly included in Z), the average product of Green functions results as follows:

$$\Phi(x,x',E,\omega) = \Phi_R(x,x',E,\omega) + \Phi_L(x,x',E,\omega), \tag{101}$$

where

$$\Phi_R(x,x',E,\omega) = \frac{e^{-\frac{i\omega x'}{2p_E}}}{4p_E^2} \sum_{m,m'=0}^{\infty} \tilde{L}_{m'}(x') Z_{m',m}(x',x) \times \left(e^{\frac{i\omega x}{2p_E}} \tilde{R}_m(x) + e^{-\frac{i\omega x}{2p_E}} \tilde{R}_{m+1}(x) \right) \tag{102}$$

and

$$\Phi_L(x,x',E,\omega) = \frac{e^{\frac{i\omega x'}{2p_E}}}{4p_E^2} \sum_{m,m'=0}^{\infty} \tilde{L}_{m'+1}(x') Z_{m',m}(x',x) \times \left(e^{\frac{i\omega x}{2p_E}} \tilde{R}_m(x) + e^{-\frac{i\omega x}{2p_E}} \tilde{R}_{m+1}(x) \right) \quad (103)$$

The two contributions, Eqs. (102,103), correspond to the cases where the particle leaves the initial point x' towards the right-hand or left-hand side, respectively. Each of these contributions, in turn, is a sum of two terms corresponding to the particle arriving at the final point x from the left-hand or right-hand side, respectively. Fig. (10), for example, contributes to the second term $\tilde{L}_1(x')Z_{10}(x',x)\tilde{R}_1(x)$ in Eq. (102) (i. e. $m = 1$ and $m' = 0$). As shown in [20], the two contributions, Eqs. (102, 103), are identical in the limit $\omega \to 0$ (which is associated with the limit $m, m' \to \infty$, where the difference between $\tilde{L}_{m'}(x')$ and $\tilde{L}_{m'+1}(x')$ can be neglected).

Differential equations for $\tilde{R}$, $\tilde{L}$ and Z can be obtained by considering infinitesimal shifts of the initial and final points x' and x, and counting all possibilities of inserting one of the vertices displayed in Fig. (11) in the corresponding infinitesimal interval. It is easy to verify that all terms associated with $1/\ell_+$ and $1/\ell_0$ counterbalance each other: let us denote the number of solid and dashed lines by k (where $k = 2m$ in the case of $\tilde{R}$ and $\tilde{L}$, whereas $k = 2m+1$ in the case of Z). We then may attach the vertex a to any of the k solid lines, and the vertex a' to any of the k dashed lines. Similarly, vertex b [or b'] may be attached to $k(k-1)/2$ different pairs of two solid (or two dashed) lines, and vertex d to k^2 different pairs of one solid and one dashed line. In total, this amounts to $k(-1/2\ell_- - 1/2\ell_+ - i/2\ell_0 - 1/2\ell_- - 1/2\ell_+ + i/2\ell_0) - k(k-1)/\ell_+ + k^2/\ell_+ = -k/\ell_-$, i. e., all terms with ℓ_+ and ℓ_0 vanish. We are left with vertices c, c', e and f. Fig. (12 a) shows an insertion of vertex f in the interval $[x - \mathrm{d}x, x]$, which amounts to a change of the index m from $\tilde{R}_{m+1}(x)$ to $\tilde{R}_m(x - \mathrm{d}x)$ (where $m = 2$ in this example). As explained in Fig. (12 b), there are in total m^2 different ways of introducing the vertex f. Repeating the same analysis for the other vertices and for Z instead of $\tilde{R}$, we arrive at the following set of differential equations:

$$-\frac{\mathrm{d}\tilde{R}_m}{\mathrm{d}x} = \frac{1}{\ell_-}\left(m^2 \tilde{R}_{m-1} e^{i\omega x/p_E} + m^2 \tilde{R}_{m+1} e^{-i\omega x/p_E} - 2m^2 \tilde{R}_m \right) \quad (104a)$$

$$\frac{\mathrm{d}Z_{m',m}}{\mathrm{d}x} = \frac{1}{\ell_-}\Big(m^2 Z_{m',m-1} e^{-i\omega x/p_E} + (m+1)^2 Z_{m',m+1} \times e^{i\omega x/p_E} - \left(m^2 + (m+1)^2 \right) Z_{m',m} \Big) \quad (104b)$$

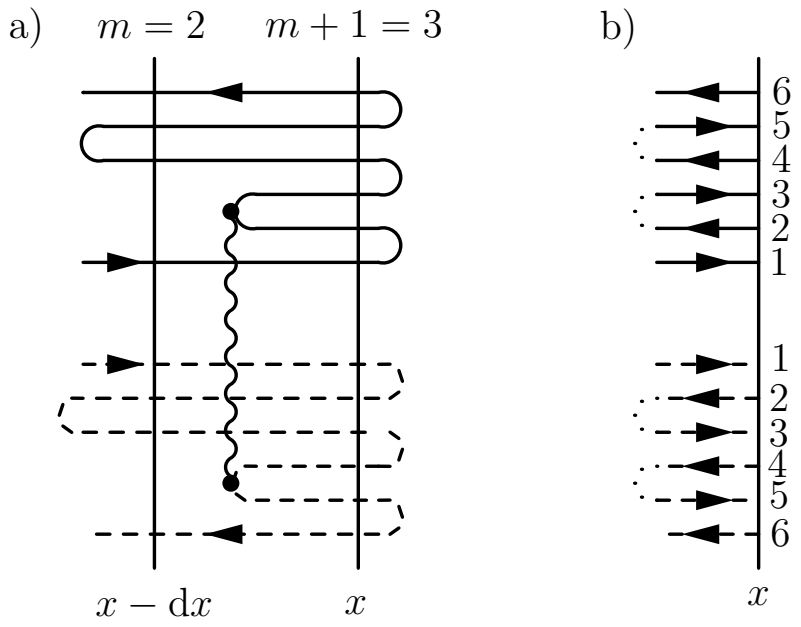

Fig. (12) (a) The vertex displayed in Fig. (11 f) is inserted between x and $x - \mathrm{d}x$ and thus changes the number of solid and dashed lines from $2(m+1) = 6$ at x to $2m = 4$ at $x - \mathrm{d}x$ (where $m = 2$). All other vertices (outside this interval) are not displayed in the figure. (b) Following the solid and the dashed line in the direction of the arrows indicated in (a) (i. e. from the initial to the final point), we count the order in which the lines pass through the point x from 1 to 6. The dotted lines indicate the places where vertex Fig. (11 f) can be inserted, such that the given order is respected. The example shown in a) results if the vertex is inserted between 2 and 3 for the solid lines and between 4 and 5 for the dashed lines, respectively. In total, there are $m^2 = 4$ different possibilities for inserting vertex Fig. (11 f).

The left-hand part follows through the symmetry relation $\tilde{L}_m(x) = \tilde{R}_m(-x)$. Furthermore, due to translational symmetry, $\tilde{R}_m(x)$ can be shown to fulfill $\tilde{R}_m(x) = e^{i\omega m x/p_E} R_m$ with position-independent coefficients R_m, which are given by

$$i\omega\ell_- R_m + m\left(R_{m+1} + R_{m-1} - 2R_m\right) = 0 \tag{105}$$

for $m \geq 1$ and $R_0 = 1$ (trivial multiplication with 1 if no vertices are present in the right-hand part). Eq. (104b) is supplemented with the boundary condition $Z_{m',m}(x', x) = \delta_{m',m}$ for $x = x'$. Eqs. (104a) and (104b) can now be solved by treating m as a continous variable $p = -im\omega\ell_-$ (which is justified in the limit $\omega \to 0$ where m tends to infinity) and then solving differential equations in p [20]–[22]. The final result for

the asymptotic density $\overline{n_E(x-x')}$ following from Eqs. (93, 101-103) then reads [22]:

$$\begin{aligned}\overline{n_E(x-x')} &= \frac{\pi^2\gamma_{\text{Born}}(E)}{8}\int_0^\infty du\; u\sinh(\pi u)\left[\frac{1+u^2}{1+\cosh(\pi u)}\right]^2 \\ &\times \exp\{-(1+u^2)\gamma_{\text{Born}}(E)|x-x'|/2\},\end{aligned} \tag{106}$$

where we used Eq. (100). The normalization constant turns out as $\overline{\rho_E} = 1/(2\pi p_E)$, i. e., the density of states for a free particle.

4.1.4 *Discussion*

A crucial element of Berezinskii's derivation is the ability to introduce a spatial ordering between the positions of vertices, i. e., $x_1 < x_2 < x' < x_3 < x_4 < x < x_5$ in Fig. (10). For this reason, the method of Berezinskii is restricted to one-dimensional systems and cannot be generalized to higher dimensions.

Furthermore, even for one-dimensional systems, the method is not exact, since it considers only a certain class of diagrams, which we called the 'essential diagrams'. The approximate character of this method manifests itself in the fact that the Born approximation $\gamma_{\text{Born}}(E)$ of the Lyapunov exponent appears in the final result, Eq. (106). As we will see in Subs. 5.3.2, however, the Born approximation is only valid for high energies.

We therefore expect that a much more accurate expression of $\overline{n_E(x)}$ is obtained if $\gamma_{\text{Born}}(E)$ in Eq. (106) is replaced by the exact value $\gamma(E)$ of the Lyapunov exponent. This leads to Eq. (5), as already anticipated in Subs. 2.2.2. This procedure is consistent with the one-parameter theory of localization [9], according to which the behaviour of physical quantities should be governed by a single parameter, e. g. by the Lyapunov exponent $\gamma(E)$. Although we are not aware of a rigorous proof, we expect that this one-parameter scaling hypothesis is valid, in our case, at least for distances larger than the correlation length σ_c of the random potential. This expectation will be confirmed by numerical simulations in Chapter 7.

4.2 GENERALIZATION OF BEREZINSKII'S METHOD TO WAVE PACKETS

We now turn towards the generalization of Berezinskii's method to the case of wave packets.

4.2.1 *Average intensity propagator with two different source points*

Similarly to Eq. (91), we can express the asymptotic average particle density in terms of Green functions as follows:

$$\begin{aligned}\overline{n(x)} &= \lim_{\omega\to 0}\frac{\omega}{2\pi i}\int_{-\infty}^{\infty}\mathrm{d}E\int_{-\infty}^{\infty}\mathrm{d}x''\mathrm{d}x'''\langle x''|\psi_0\rangle\langle\psi_0|x'''\rangle \\ &\quad\times\overline{G^{(+)}(x,x'',E+\omega)G^{(-)}(x''',x,E)}. \end{aligned} \tag{107}$$

The equivalence of Eq. (107) with our original definition of $\overline{n(x)}$ introduced in Subs. 3.1.3, see Eq. (24), is demonstrated in Appendix A. As compared to Eq. (91) for $\overline{n_E(x)}$, this expression exhibits additional integrals over the energy E and the two source points x'' and x'''. Moreover, the average product of Green functions now contains two different source points x'' and x''' instead of a single source point x' in Eq. (89). We therefore generalize Berezinskii's intensity propagator, see Eq. (92) as follows:

$$\tilde{\Phi}(x,x'',x''',E,\omega) = \overline{G^{(+)}(x,x'',E+\omega)G^{(-)}(x''',x,E)} \tag{108}$$

such that

$$\begin{aligned}\overline{n(x)} &= \lim_{\omega\to 0}\frac{\omega}{2\pi i}\int_{-\infty}^{\infty}\mathrm{d}E\int_{-\infty}^{\infty}\mathrm{d}x''\mathrm{d}x'''\langle x''|\psi_0\rangle\langle\psi_0|x'''\rangle \\ &\quad\times\tilde{\Phi}(x,x'',x''',E,\omega) \end{aligned} \tag{109}$$

In the following, our aim is to establish a relation between $\tilde{\Phi}(x,x'',x''',E,\omega)$ and $\Phi(x,x',E,\omega) = \tilde{\Phi}(x,x',x',E,\omega)$, which will allow us to generalize Berezinskii's technique to the case of wave packets.

4.2.2 *Neglect of disorder in the vicinity of the source points*

An example of a diagram contributing to $\tilde{\Phi}(x,x'',x''',E,\omega)$ is shown in Fig. (13). Let us first assume, for simplicity, that no vertices (i. e. no scattering events by the random potential) occur in the region between the two source points x'' and x'''. Obviously, it is almost identical to the corresponding Berezinskii diagram in Fig. (10). However, the free propagators $G_0^{(+)}(x'-x_3,E+\omega)$ and $G_0^{(-)}(x'-x_4,E)$ describing the initial propagation from the source x' to the first scattering event at x_3 (for the solid line) or x_4 (for the dashed line) in Fig. (10), must now be replaced by $G_0^{(+)}(x''-x_3,E+\omega)$ and $G_0^{(-)}(x'''-x_4,E)$ in Fig. (13), respectively. Taking into account the explicit form of the free-particle Green functions, Eq. (57) with $p_E=\sqrt{E}$, the shifts of the initial positions from x' to x'' and from x' to x''', respectively, lead, in total, to an exponential factor:

$$e^{ip_E(x'''-x'')} = \frac{G_0^{(+)}(x''-x_3,E)G_0^{(-)}(x'''-x_4,E)}{G_0^{(+)}(x'-x_3,E)G_0^{(-)}(x'-x_4,E)}, \tag{110}$$

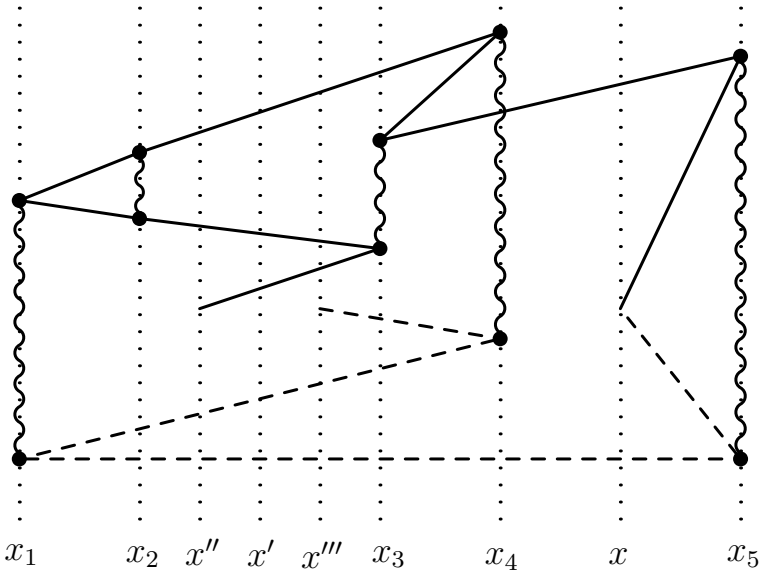

Fig. (13) Diagram contributing to the intensity propagator $\tilde{\Phi}(x, x'', x''', E, \omega) = \overline{G^{(+)}(x, x'', E+\omega)G^{(-)}(x''', x, E)}$ with two source points x'' and x''', as it appears in the case of wave packets. The diagram is almost identical to the one shown in Fig. (10), except for the fact that the source point x' of Fig. (10) is replaced by two different source points x'' and x'''. As compared to Fig. (10), this introduces an additional factor $e^{ip_E(x'''-x'')}$.

for $x'' < x' < x''' < x_{3,4}$ (where the limit $\omega \to 0$ was taken). In other words, the contribution of diagram Fig. (13) is given by the contribution of diagram Fig. (10) times the above factor, Eq. (110). The same factor applies if x'' and x''' are exchanged, i.e. for diagrams in which $x''' < x' < x'' < x_{3,4}$, whereas the complex conjugate factor $e^{-ip_E(x'''-x'')}$ is obtained in the cases where the particle initially propagates to the left-hand side, i.e. $x_{3,4} < x'' < x' < x'''$ or $x_{3,4} < x''' < x' < x''$.

Hence, if we decompose, similarly as in Eq. (101) the propagator into two parts:

$$\tilde{\Phi}(x, x'', x''', E, \omega) = \tilde{\Phi}_R(x, x'', x''', E, \omega) + \tilde{\Phi}_L(x, x'', x''', E, \omega), \quad (111)$$

corresponding to initially right- or left-propagating particles, we obtain:

$$\tilde{\Phi}_R(x, x'', x''', E, \omega) = e^{ip_E(x'''-x'')}\Phi_R(x, x', E, \omega), \quad (112)$$

$$\tilde{\Phi}_L(x, x'', x''', E, \omega) = e^{-ip_E(x'''-x'')}\Phi_L(x, x', E, \omega) \quad (113)$$

Inserting these relations into Eq. (109) and using Eq. (93), we see that:

$$\begin{aligned}\overline{n(x)} &= \int_{-\infty}^{\infty} \mathrm{d}E \int_{-\infty}^{\infty} \mathrm{d}x'' \mathrm{d}x''' \overline{n_E\left(x - \frac{x''+x'''}{2}\right)} \\ &\times \langle x''|\psi_0\rangle\langle\psi_0|x'''\rangle \underbrace{\frac{e^{ip_E(x'''-x'')} + e^{-ip_E(x'''-x'')}}{4\pi p_E}}_{=-\Im\left\{G_0^{(+)}(x'''-x'',E)\right\}/\pi}, \end{aligned} \tag{114}$$

where a factor $1/(2\pi p_E)$ results from the normalization factor $\overline{\rho_E} = 1/(2\pi p_E)$ (resulting as the density of states for a free particle in 1D, as mentioned above) in Eq. (93), and another factor $1/2$ from the distinction between diagrams where the particle initially propagates to the left or to the right-hand side, respectively, which, as discussed in the paragraph after Eq. (103) above, give exactly the same contribution $\overline{n_E(x-x')}/2$ to the total density, if the initial point x' is chosen in a symmetric way, i.e. $x' = \frac{x''+x'''}{2}$.

We recognize the last term of Eq. (114) as the negative imaginary part of the free-particle Green function, Eq. (57), dividided by π, which, in turn, is related to the spectral function:

$$\begin{aligned} A_0(p,E) &= -\frac{1}{\pi}\int_{-\infty}^{\infty} \mathrm{d}x''\, e^{-ip(x''-x''')}\Im\{G_0^{(\pm)}(x''-x''',E)\}, \\ &= \delta(E-p^2), \end{aligned} \tag{115}$$

of a free particle, see also Eq. (11) Together with the definition of the initial state's Wigner function, see Eq. (10), Eq. (114) turns into:

$$\overline{n(x)} = \int_{-\infty}^{\infty} \mathrm{d}E \int_{-\infty}^{\infty} \mathrm{d}p\mathrm{d}q\; W(q,p) A_0(p,E) \overline{n_E(x-q)}. \tag{116}$$

This reproduces Eq. (9) – apart from the fact that the average spectral function $A(p,E)$ in the presence of the random potential is approximated by the spectral function $A_0(p,E)$ of the free particle.

4.2.3 *Including disorder in the vicinity of the source points*

Remember, however, that our above derivation neglects the presence of the random potential in the vicinity of the source! The remaining diagrams, i. e., those which also contain vertices between x'' and x''' are treated in Appendix B. As shown there – under the assumption of a spatially confined initial wave packet (with width a much smaller than the localization length) – the above relations Eqs. (112,113) are replaced by:

$$\tilde{\Phi}_R(x,x'',x''',E,\omega) = e^{i\tilde{p}_E(x'''-x'')}\Phi_R(x,x',E,\omega), \tag{117}$$

$$\tilde{\Phi}_L(x,x'',x''',E,\omega) = e^{-i\tilde{p}_E^*(x'''-x'')}\Phi_L(x,x',E,\omega) \tag{118}$$

where $\tilde{p}_E$ denotes the complex effective wave vector, which determines the average Green function according to Eq. (77). Correspondingly (as discussed in Appendix B), the free particle Green function $G_0^{(\pm)}(x'' - x''', E)$ is replaced by the average Green function $\overline{G^{(\pm)}(x'' - x''', E)}$ in Eq. (114), and $A_0(p, E)$ by $A(p, E)$ in Eq. (116) (see Chapter 6). This concludes the derivation of our final result, Eq. (9).

According to this result, two ingredients are required in order to evaluate the average asymptotic density $\overline{n(x)}$: first, the Lyapunov exponent $\gamma(E)$ determines the shape of the density profile $\overline{n_E(x)}$ at fixed energy, see the discussion in Subs. 4.1.4 above. Second, the spectral function $A(p, E)$ is needed in order to calculate the energy distribution of the initial wavepacket $\psi_0(x)$. The following Chapters 5 and 6 will be concerned with finding accurate analytical expressions for these two quantities.

5

LYAPUNOV EXPONENT

The Lyapunov exponent defines the inverse of the localization length, and thus represents a crucial quantity describing exponential localization of wave functions. In one-dimensional uncorrelated random potentials, all energy eigenfunctions are exponentially localized, and thus exhibit a non-zero Lyapunov exponent, which, in general, depends on the corresponding energy of the eigenfunction. In this chapter, we will derive an analytical expression of the Lyapunov exponent valid in good approximation for random potentials which exhibit either weak fluctuations or a short correlation length (or both). As explained in the previous chapter (see the discussion in Subs. 4.1.4), this expression will be used to obtain the shape of the asymptotic density profile at fixed energy, see Eq. (5).

First, we will define the Lyapunov exponent in Sec. 5.1, and state Oseledets' theorem [57],[1] which guarantuees that, in the presence of a random potential without correlations, all eigenfunctions are exponentially localized. We present a numerical method for determining the Lyapunov exponent in a one-dimensional correlated potential in Sec. 5.2, which we then compare with a perturbative analytical expression obtained from the Born approximation in Sec. 5.3. This expression, however, fails for small energies, where it exhibits a divergence, whereas the numerically determined Lyapunov exponent remains finite for all energies. We therefore review works of Thouless [23] and Halperin [25], who found an exact expression for the Lyapunov exponent, valid for all energy ranges in the case of a white noise potential, see Sec. 5.4. This expression is also valid, with good approximation, for random potentials with a finite correlation length σ_c in the regime of small energies, where the wave length of the particle is much larger than σ_c. On the basis of this result, we finally construct an interpolation between the exact white noise result (valid at low energies) and the Born approximation (valid at large energies) in Sec. 5.5. By comparison with numerical data, we show that this interpolation well describes the Lyapunov exponent in the entire range of energies, for random correlated potentials which satisfy the condition $V_0\sigma_c^2 \ll 1$. This condition implies that the kinetic energy of a particle with wavelength comparable to the correlation length σ_c is much larger than the typical size V_0 of the potential's fluctuations.

1 With previous work on random multiplication of matrices by Furstenberg [58] and Furstenberg-Kesten [59].

5.1 DEFINITION

For a one-dimensional uncorrelated random potential $V(x)$, all eigenfunctions $\psi_E(x)$ are exponentially localized [4]. The rate of exponential decay defines the Lyapunov exponent

$$\gamma(E) = -\lim_{x\to\infty} \overline{\ln\left(||\psi_E(x)||\right)}/|x|. \tag{119}$$

In this definition, $||.||$ describes a norm, which is chosen as the absolute value $|.|$ if the wave function is complex, whereas $||\psi_E(x)|| = \sqrt{\psi_E(x)^2 + [\partial_x\psi_E(x)]^2/E}$, see Eq. (129) below, if $\psi_E(x)$ is required to be real [52]. Note that the definition given by Eq. (119) is based on the average of the logarithm of $||\psi_E(x)||$. The average intesity $\overline{||\psi_E(x)||^2}$ decays with a different exponent, which can be shown to be given by $\gamma(E)/2$ [60], see also Eq. (7). For this reason, as we already mentioned after Eq. (7), the definition of the localization length based on the decay of the average intensity, see Eq. (1), differs from definition $L_{\rm loc}(E) = 1/\gamma(E)$ based on the decay of the average logarithm, see Eq. (119), which we will use in the following.

The Lyapunov exponent is also very well known in the context of chaotic, dynamical system, where it quantifies the sensitivity with respect to small changes of the initial conditions. These deviations are also obtained from the multiplication of matrices which, for a chaotic system, are similar to random matrices [61]. With the purpose of understanding the meaning of the Lyapunov exponent, we first review Oseledets' [57] and Furstenberg's [58] multiplicative ergodic theorem (MET). After that, we will apply it to the one-dimensional Schödinger equation, as it has already been done in many previous works on one-dimensional disordered systems [62]–[66].

Oseledets' and Furstenberg's multiplicative ergodic theorem (MET)

The Oseledets' and Furstenberg's MET affirms that, for a sequence $\{\mathbf{P}_n\}$ of independently and identically distributed random $d \times d$ matrices, there exists a matrix Γ defined as:

$$\Gamma \equiv \lim_{N\to\infty} \left(\mathbb{P}_N^T \mathbb{P}_N\right)^{\frac{1}{2N}} \geq 0 \tag{120}$$

where $\mathbb{P}_N = \mathbf{P}_N \mathbf{P}_{N-1} \cdots \mathbf{P}_1$. According to Eq. (120), each sequence $\mathbb{P}_N$ converges with probability 1 to the same matrix Γ. If $\{U_1, ..., U_d\}$ and $\{\gamma_1, ..., \gamma_d\}$ are the eigenvectors and eigenvalues of Γ respectively, then, for every vector $\mathbf{x}$ on the d-dimensional space, the quantity γ defined as:

$$\gamma(\mathbf{x}) \equiv \lim_{N\to\infty} \frac{1}{N} \log \|\mathbb{P}_N \mathbf{x}\|, \tag{121}$$

fulfills $\gamma(\mathbf{x}) = \max(\gamma_i, ..., \gamma_j)$, where $\{U_i, ..., U_j\}$ is the subset of the eigenvector spaces on which $\mathbf{x}$ has a non-zero projection.

The main point established by Oseledec's and Furstenberg's MET is the fact that the norm of any vector $\mathbf{x}$ diverges exponentially fast under repeated action of the matrix $\mathbb{P}_N$. The rate of the asymptotic exponential divergence is determined by the set $\{\gamma_i, ..., \gamma_j\}$ consisting of the Lyapunov characteristic exponents of $\mathbb{P}_N$. More precisely, the divergence is dominated by the component of $\mathbf{x}$ on $\{U_i, ..., U_j\}$ which has the fastest growing rate [67].

5.2 NUMERICAL DETERMINATION

To apply Oseledets' and Furstenberg's MET to the one-dimensional Schödinger equation, we transform the continuous time-independent Eq. (18), which describes non-interacting particles with energy $E = p_E^2$ in a one-dimensional disordered potential, to a discrete equation with a spatial stepsize $\Delta x \ll \sigma_c, E^{-1/2}$:

$$\psi_E^{n+1} = [(V^n - E)(\Delta x)^2 + 2]\psi_E^n - \psi_E^{n-1},$$

where $\psi_E^n = \psi_E(n\Delta x)$ and $V^n = V(n\Delta x)$ represent the complex state ψ_E and the real potential V at the point $n \cdot \Delta x$, respectively. Therefore, their matrix representation is:

$$\begin{pmatrix} \psi_E^{n+1} \\ \psi_E^n \end{pmatrix} = \begin{pmatrix} [(V^n - E)(\Delta x)^2 + 2] & -1 \\ 1 & 0 \end{pmatrix} \begin{pmatrix} \psi_E^n \\ \psi_E^{n-1} \end{pmatrix} = \mathbf{P}_{2\times 2}^n \begin{pmatrix} \psi_E^n \\ \psi_E^{n-1} \end{pmatrix}. \tag{122}$$

The matrix $\mathbf{P}_{2\times 2}^n$ in Eq. (122) is symplectic, therefore the condition:

$$\det \mathbb{P}_{N_L} = 1, \quad \text{where } \mathbb{P}_{N_L} = \mathbf{P}_{2\times 2}^{N_L} ... \mathbf{P}_{2\times 2}^1, \tag{123}$$

is fulfilled for all total numbers of sites N_L. Hence, the determinant of Γ equals 1, see Eq. (120), and with this, in the limit $N_L \to \infty$, the eigenvalues of $\mathbb{P}_{N_L}$ converge to $\{\gamma_1, \gamma_2\} = \{e^{-\gamma N_L}, e^{+\gamma N_L}\}$ with Lyapunov exponent γ.

Alternatively, the Lyapunov exponent can also be extracted from determining the transmission of an incident plane wave through a random potential with length $L = N_L \Delta x$. For this purpose, we solve Eq. (122) with boundary conditions: $\psi_E^{(0)} = 1 + r$ and $\psi_E^{(1)} = e^{ip_E \Delta x} + re^{-ip_E \Delta x}$ (where r denotes the reflection amplitude), and $\psi_E^{(N_L)} = t$ and $\psi_E^{(N_L+1)} = te^{ip_E \Delta x}$ (where t denotes the transmission amplitude). The transmision probability $T = |t|^2$ then results from the matrix $\mathbb{P}_{N_L}$ as follows [5]:

$$T(E) = \frac{4 \sin^2(\sqrt{E} \cdot \Delta x)}{|\mathbb{P}_{21} - \mathbb{P}_{12} + \mathbb{P}_{22} e^{-i\sqrt{E} \cdot \Delta x} - \mathbb{P}_{11} e^{i\sqrt{E} \cdot \Delta x}|^2}. \tag{124}$$

Finally, the Lyapunov exponent is obtained as [68]:

$$\gamma(E) = -\lim_{N_L\to\infty} \frac{1}{2N_L} \ln T(E). \tag{125}$$

As already mentioned above, the localization length is defined as the inverse of the Lyapunov exponent, i. e., $L_{loc}(E) = \big(\gamma(E)\big)^{-1}$.

Numerically, we choose $\Delta x = 0.1\sigma_c$ and $N_L = 8000$, and then determine the Lyapunov exponent

$$\gamma(E) = -\frac{1}{2N_L} \ln\big[T(E)\big].$$

We take realizations of disordered potentials with finite length (i. e. $L = 8000\Delta x$), and then average $\gamma(E)$ over 2000 different realizations. The averaging is needed to obtain a more accurate numerical value, since $\gamma(E)$ is independent of the realization of the potential only in the limit $N_L \to \infty$. For $V_0\sigma_c^2 = 0.0165$ and $V_0\sigma_c^2 = 0.0325$, the numerical results for $\gamma(E)$ are shown in Fig. (15) below.

5.3 PERTURBATION THEORY

5.3.1 *Phase formalism*

Eqs. (124,125) are useful for numerical computations of the Lyapunov exponent. An analytical expression of the Lyapunov exponent can be obtained in the frame of perturbation theory [52]. For this purpose, let us consider the polar representation of the real-valued solution $\psi_E(x)$ of the stationary Schrödinger equation Eq. (18), which introduces amplitude and phase coordinates (r, θ) as follows:

$$\psi_E(x) = r(x)\sin[\theta(x)], \tag{126}$$

$$\partial_x\psi_E(x) = \sqrt{E}\, r(x)\cos[\theta(x)]. \tag{127}$$

for $E > 0$. Fig. (14) shows an example of a real-valued function $\psi_E(x)$, which exhibits oscillations between positive and negative values (black line), and the corresponding amplitude (red line), which is strictly positive, and can be used to describe the localization of the wave packet.

We now consider a solution of the Schrödinger Eq. (18) for a given initial condition $r_0 = r(0)$ and $\theta_0 = \theta(0)$. The corresponding Lyapunov exponent describes the exponential decay of the amplitude $r(x)$:

$$\gamma(E) = -\lim_{|x|\to\infty} \frac{\overline{\ln[r(x)/r_0]}}{|x|}. \tag{128}$$

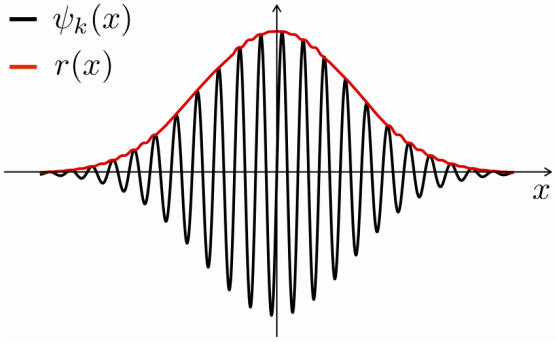

Fig. (14) Real-valued wave function $\psi_E(x)$ (black line), and its amplitude $r(x)$ (red line) defined by Eqs. (126,127) in the phase formalism.

With the purpose of finding an analytic expression of $\ln[r(x)/r_0]$, we first solve Eqs. (126,127) for the amplitude $r(x)$:

$$r(x) = \sqrt{\psi_E^2(x) + \frac{(\partial_x \psi_E(x))^2}{E}}, \tag{129}$$

and then calculate its partial logarithmic derivative:

$$\partial_x \ln[r(x)] = \frac{\partial_x r(x)}{r(x)} = \frac{\partial_x \psi_E(x)}{r^2(x)} \left[\psi_E(x) + \frac{\partial_x^2 \psi_E(x)}{E}\right]. \tag{130}$$

Inserting Eqs. (18) and (126,127) in Eq. (130), we conclude:

$$\ln[r(x)/r_0] = \frac{1}{2\sqrt{E}} \int_0^x \mathrm{d}x' V(x') \sin[2\theta(x')], \tag{131}$$

which is a function of the phase variable $\theta(x)$.

The latter is obtained after dividing Eq. (127) by Eq. (126):

$$\frac{\partial_x \psi_E(x)}{\psi_E(x)} = \sqrt{E}\ \cot[\theta(x)]. \tag{132}$$

To deduce an equation for $\theta(x)$, we take the derivative of both sides of the last expression with respect to x and, after that, we use Eq. (18) to obtain:

$$-\frac{\sqrt{E}\partial_x \theta(x)}{\sin^2[\theta(x)]} = V(x) - E(1 + \cot^2[\theta(x)]). \tag{133}$$

Thereby, we conclude a differential equation for $\theta(x)$:

$$\partial_x \theta(x) = \sqrt{E} - \frac{V(x)}{\sqrt{E}} \sin^2[\theta(x)], \tag{134}$$

with formal solution:

$$\theta(x) = \theta_0 + \sqrt{E}x - \frac{1}{\sqrt{E}} \int_0^x \mathrm{d}x' V(x') \sin^2[\theta(x')], \tag{135}$$

where $\theta_0 = \theta(0)$ is an initial condition. This phase angle was introduced by H. Prüfer in [69].

5.3.2 *Born approximation*

For weak random potentials, Eq. (135) can be solved iteratively, which yields an expansion of its solution in powers of $V(x)$. Choosing $\theta_0 = 0$, we get for the lowest two orders:

$$\theta^{(0)}(x) = \sqrt{E}\, x, \tag{136}$$

$$\theta^{(1)}(x) = -\frac{1}{\sqrt{E}} \int_0^x \mathrm{d}x' V(x') \sin^2 [\theta^{(0)}(x')], \tag{137}$$

Expanding the expression $\sin [2\theta(x)]$, with $\theta(x) \simeq \theta^{(0)}(x) + \theta^{(1)}(x)$, in Eq. (131) up to first order in $\theta^{(1)}(x)$, i.e. $\sin [2\theta(x)] \simeq \sin [2\theta^{(0)}(x)] + 2\cos [2\theta^{(0)}(x)]\theta^{(1)}(x)$, we conclude the two first orders of $\ln [r(x)/r_0]$ as:

$$\ln^{(1)}[r(x)/r_0] = \frac{1}{2\sqrt{E}} \int_0^x \mathrm{d}x' V(x') \sin^2 [2\sqrt{E}x'], \tag{138}$$

$$\ln^{(2)}[r(x)/r_0] = -\frac{1}{E} \int_0^x \mathrm{d}x' \int_0^{x'} \mathrm{d}x'' V(x')V(x'') \times \cos [2\sqrt{E}x'] \sin^2 [\sqrt{E}x'']. \tag{139}$$

Performing the disorder average according to the definition from Eq. (128) and assuming $\overline{V(x)} = 0$, the average over Eq. (138) is zero, while the result of Eq. (139) is:

$$\ln^{(2)}[r(x)/r_0] = -\frac{1}{E} \int_0^x \mathrm{d}x' \int_{-x'}^0 \mathrm{d}x_1 C_2(x_1) \cos [2\sqrt{E}x'] \sin^2 [\sqrt{E}(x' + x_1)]. \tag{140}$$

We now exchange the order of integration, i.e. $\int_0^x \mathrm{d}x' \int_{-x'}^0 \mathrm{d}x_1 \cdots = \int_{-x}^0 \mathrm{d}x_1 \int_{-x_1}^x \mathrm{d}x' \ldots$, and perform the integral over x'. Since $C_2(x_1)$ decays to zero for large values of x_1, we may, in the limit of large x, change the limits for the integral over x_1 from $(-x, 0)$ to $(-\infty, 0)$. Then, we use Eq. (128) together with:

$$\lim_{x\to\infty} \frac{1}{x} \int_{-x_1}^x \mathrm{d}x' \cos [2\sqrt{E}x'] \sin^2 [\sqrt{E}(x' + x_1)] = -\frac{1}{4} \cos[2\sqrt{E}x_1] \tag{141}$$

and, finally, the fact that $C_2(x_1)$ and $\cos [\sqrt{E}x_1]$ are even functions of x_1, to arrive at our final result for the Lyapunov exponent in Born approximation:

$$\gamma_{\text{Born}}(E) = \frac{1}{8E} \int_{-\infty}^{\infty} \mathrm{d}x_1 C_2(x_1) \cos (2\sqrt{E}x_1). \tag{142}$$

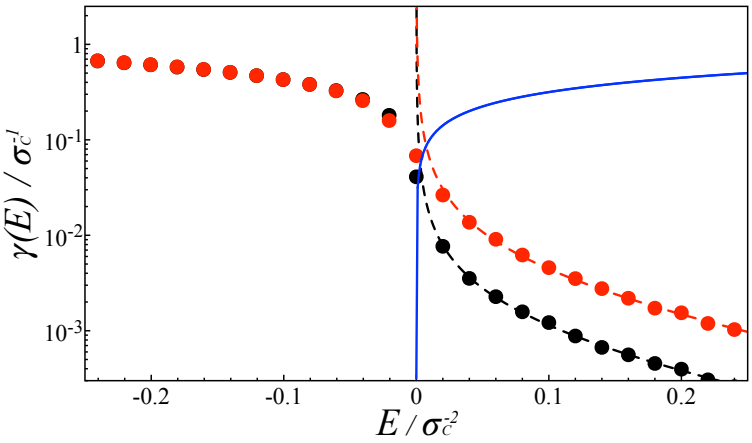

Fig. (15) Lyapunov exponent (in units of σ_c^{-1}) for a Gaussian correlated potential, see Eq. (30), as a function of energy (in units of σ_c^{-2}) for two different strengths of the random potential, $V_0\sigma_c^2 = 0.0165$ (black) and $V_0\sigma_c^2 = 0.0325$ (red), both of which fulfill the condition $V_0\sigma_c^2 \ll 1$ of a weak random potential. For both values of the potential, the Born approximation, Eq. (142) (dashed lines), agrees well with the result of numerical transfer matrix calculations (dots) in the range of high energies, but exhibits a divergence at $E \to 0$. In order to demonstrate the range of validity $\sqrt{E} \gg \gamma(E)$, we plot $\sqrt{E}$ as a blue curve.

For the case of the speckle potential, Eq. (38), the result of Eq. (142) is given by Eq. (2), as already announced in Chapter 2.

For the case of a random potential with Gaussian correlation function, see Eq. (30), we obtain:

$$\gamma_{\text{Born}}(E) = \sqrt{\frac{\pi}{2}} \frac{\sigma_c V_0^2}{4E} e^{-2\sigma_c^2 E}, \tag{143}$$

This expression is compared with numerical data, obtained by the transfer matrix method as explained in Sec. 5.2 for 2000 disordered potentials of length $L = 800\sigma_c$, in Fig. (15). We see that the Born approximation gives a good prediction for the Lyapunov exponent for large energies. More precisely, we estimate that the Born approximation is valid for $\sqrt{E} \gg \gamma(E)$, see the blue line in Fig. (15). For weak random potentials, i. e., if $V_0\sigma_c^2 \ll 1$, Eq. (143) is therefore valid if $E \gg (\sigma_c V_0^2)^{2/3}$. For small energies, however, we observe huge deviations between the Born approximation and the numerics. First, the Born approximation is defined only for positive energies, see Eq. (127). Second, it exhibits a divergence for $E \to 0$, which is not present in the numerial data. As already mentioned in Chapter 2, these shortcomings of the Born approximation are one reason for the fact that previous theoretical attempts fail to describe the center of the localized density profile, which is determined by small (and negative) energies.

5.4 EXACT EXPRESSION FOR UNCORRELATED POTENTIALS

In order to cure the shortcomings of the Born approximation discussed above, we are now looking for an analytical expression of the Lyapunov exponent which is valid, in particular, also in the regime of small energies. For this purpose, we will rely on the fact that an exact, analytical theory exists for one-dimensional white-noise potentials. This theory will turn out to be useful also for correlated potentials in the regime of small energies, where the wavelength of the particle is so long that it effectively cannot distinguish a correlated potential (with correlation length much smaller than the wavelength) from a white-noise potential.

5.4.1 *Thouless' relation between Lyapunov exponent and density of states*

The Thouless relation, see Eq. (152) below, which plays a major role in this thesis, can be easily derived from the Green function formalism presented in Chapter 3. Using the notation of Thouless' paper [23], we consider a particle on a one-dimensional lattice with lattice sites $n = 1, \ldots, N$. The Schrödinger equation reads:

$$E_n \psi_n^\alpha - V_{n,n+1}\psi_{n+1}^\alpha - V_{n-1,n}\psi_{n-1}^\alpha = E_\alpha \psi_n^\alpha, \tag{144}$$

where E_n is the energy of the n-site, $V_{n,n+1}$ or $V_{n-1,n}$ the coupling between the sites (n) and $(n+1)$, or $(n-1)$ and (n), respectively, and ψ_{n-1}, ψ_n, and ψ_{n+1} are the real amplitudes for the eigenstate with eigenvalue E_α.

As discussed in Sec. 5.2 above, also our continuous Schrödinger Eq. (18) can be brought into this form by discretization on a sufficiently fine lattice. In this case, we obtain $V_{n,n\pm1} = 1/(\Delta x)^2$ and $E_n = V(n\Delta x) - 2/(\Delta x)^2$.

The Green function for Eq. (144) reads:

$$(E - E_n)G_{nm}(E) + V_{n,n+1}G_{n+1m}(E) + V_{n-1,n}G_{n-1m}(E) = \delta_{nm}. \tag{145}$$

In the following, we will be interested in the element $G_{1N}(E)$ describing propagation from one side of the chain to the other side. From Eq. (145) we can deduce that $G_{1N}(E)$ are elements of the inverse of the $N \times N$-matrix $E\mathbb{I} - \mathbb{H}$, where $\mathbb{I}$ is the unit matrix and $\mathbb{H}$ is the Hamiltonian of the whole system. Since the cofactor of the matrix element $(E\mathbb{I} - \mathbb{H})_{1N}$ is $\prod_{i=1}^{N-1} V_{i,i+1}$, we obtain:

$$G_{1N}(E) = \frac{\prod_{i=1}^{N-1} V_{i,i+1}}{\det(E\mathbb{I} - \mathbb{H})} = \frac{\prod_{i=1}^{N-1} V_{i,i+1}}{\prod_{\alpha=1}^{N}(E - E^\alpha)} = \frac{\left(\frac{1}{(\Delta x)^2}\right)^{N-1}}{\left(\prod_{\alpha=1}^{N}(E - E^\alpha)\right)\Delta x}.$$

(146)

On the other hand, we can also express $G_{1N}(E)$ in terms of the eigenstates $\{|\psi^\alpha\rangle\}$ and eigenenergies $\{E^\alpha\}$ of the Hamiltonian H:

$$G_{1N}(E) = \langle 1|G(E)|N\rangle = \sum_{\alpha=1}^{N} \langle 1|\psi^\alpha\rangle\langle\psi^\alpha|G(E)|\psi^\alpha\rangle\langle\psi^\alpha|N\rangle \tag{147}$$

If $c_1(E^\alpha) = \langle 1|\psi^\alpha\rangle$ and $c_N(E^\alpha) = \langle N|\psi^\alpha\rangle$ denote the overlap of $|\psi^\alpha\rangle$ with sites 1 and N, respectively, and using Eq. (48), we can conclude:

$$G_{1N}(E) = \sum_{\alpha=1}^{N} \frac{c_1(E^\alpha)c_N^*(E^\alpha)}{E - E^\alpha}. \tag{148}$$

According to Eq. (148), G_{1N} has a pole of residue $c_1(E^\beta)c_N^*(E^\beta)$ at $E = E^\beta$ (for each $\beta = 1, ..., N$.) On the other hand, the same residue can also be extracted from Eq. (146). This yields:

$$c_1(E^\beta)c_N^*(E^\beta) = \frac{1}{\left(\prod_{\alpha\neq\beta}^{N}(E^\beta - E^\alpha)\right)(\Delta x)^2}. \tag{149}$$

Following the Anderson theorem [4], the wave function amplitudes for one single energy state in a one-dimensional disordered potential decay exponentially, with the Lyapunov exponent as decay rate. Let us assume that the eigenstate $|\psi^\beta\rangle$ is localized around site N_0. Then, the decay between the sites 1 and N_0, and between N_0 and N, respectively, are given by $c_1(E^\beta) \propto e^{-(N_0-1)\gamma(E^\beta)\Delta x}$ and $c_N(E^\beta) \propto e^{-(N-N_0)\gamma(E^\beta)\Delta x}$. Taking the logarithm of the absolute value of Eq. (149), and neglecting terms which vanish for $N \to \infty$, yields:

$$\gamma(E^\beta) = \frac{1}{(N-1)\Delta x} \sum_{\alpha\neq\beta} \ln|E^\beta - E^\alpha|. \tag{150}$$

In order to perform the continuum limit, we replace the sum over all eigenstates by an integral over the density of states $\rho(E)$:

$$\frac{1}{(N-1)\Delta x} \sum_{\alpha} \to \int \mathrm{d}E\, \rho(E).$$

Moreover, we consider the difference between $\gamma(E^\beta)$ for a disordered potential and $\gamma_0(E^\beta)$ for a free particle:

$$\gamma(E^\beta) - \gamma_0(E^\beta) = \int_{-\infty}^{\infty} \mathrm{d}E^\alpha\, [\rho(E^\alpha) - \rho_0(E^\alpha)] \ln|E^\beta - E^\alpha|, \tag{151}$$

in order to avoid a divergence of $\gamma(E^\beta)$ for high energies, where $\rho(E^\alpha) \approx \rho_0(E^\alpha)$. From the Green function of a free particle, see Eq. (57), we know that $\gamma_0(E) = 0$ for $E \geq 0$, whereas $\gamma_0(E) = \sqrt{-E}$ for $E < 0$.

Integration by parts finally yields [23]:

$$\gamma(E) - \gamma_0(E) = \mathcal{P} \int_{-\infty}^{\infty} dE' \frac{N(E') - N_0(E')}{E' - E}, \tag{152}$$

where $\mathcal{P}$ denotes the Cauchy principal value, $N(E) = \int_{-\infty}^{E} \mathrm{d}E'\, \rho(E')$ the cumulative density of states, and and $N_0(E) = \Re\{\sqrt{E}\}/\pi$ the cumulative density of states of a free particle.

Eq. (152) can be read as a Kramers-Kronig relation between the quantities $N(E)$ and $\pi\gamma(E)$. In other words, if there exists a complex function $F(z)$ which is analytic in the upper half of the complex plane and tends to $i\sqrt{z}/\pi$ as $|z| \to \infty$, and if the imaginary part of this function coincides with the cumulative density of states, i. e., $N(E) = \Im\{F(E)\}$, then the Lyapunov exponent is given by π times the real part of this function, i. e., $\gamma(E) = \pi\Re\{F(E)\}$ [24].

5.4.2 *Average density of states for uncorrelated potentials: Halperin's method*

In the previous subsection, we have derived the general relation Eq. (152) between the Lyapunov exponent and the cumulative density of states, which is valid for an arbitrary, one-dimensional disordered system. In a second step, we will now present an exact result for the average cumulative density of states for the case $C_2(x) = D\delta(x)/2$ of a white-noise potential with strength $D/2$. This result has been derived by Halperin in [25].

Halperin's strategy is based on the fact that the cumulative density of states:

$$N(E) = \int_{-\infty}^{E} \mathrm{d}E'\, \rho(E'), \tag{153}$$

is equal to the density of zeros of any real solution $\psi_E(x)$ of the Schrödinger equation, Eq. (18) [70]–[72]. Let us therefore consider a solution $\psi_E(x)$ of Eq. (18) with arbitrary boundary condition $\psi_E(0) = \xi_0$ and $\psi'_E(0) = \eta_0$ in the interval $0 \leq x \leq L$. We define

$$z(x; E) = \frac{\psi'_E(x)}{\psi_E(x)}. \tag{154}$$

Since $\psi_E(x)$ is a random function (depending on the realization of the potential $V(x)$ in the Schrödinger equation), we can define the probability density of $z(x; E)$:

$$P_0(z, x) = \overline{\delta(z - z(x; E))}. \tag{155}$$

As shown in [25], $P_0(z,x)$ fulfills the following differential equation in the case of white noise $C_2(x) = D\delta(x)/2$:

$$\frac{\partial P_0}{\partial x} = \left[D\frac{\partial^2}{\partial z^2} + \frac{\partial}{\partial z}(z^2+2E)\right]P_0, \tag{156}$$

with initial value:

$$P_0(z,0) = \delta(z-\eta_0/\xi_0). \tag{157}$$

For large x, the solution of Eq. (156) assumes a stationary distribution $p_0(z)$ (independent of x and the boundary conditions ξ_0, η_0) given by [25]:

$$\left[D\frac{\partial^2}{\partial z^2} + \frac{\partial}{\partial z}(z^2+2E)\right]p_0(z) = 0, \tag{158}$$

with normalization condition:

$$\int_{-\infty}^{\infty} \mathrm{d}z\ p_0(z) = 1, \tag{159}$$

and boundary condition:

$$\lim_{z\to\infty} z^2 p_0(z) = \lim_{z\to-\infty} z^2 p_0(z). \tag{160}$$

Finally, the cumulative average density of states is obtained as [70]:

$$\overline{N(E)} = \lim_{z\to\infty} z^2 p_0(z). \tag{161}$$

This relation can be understood as follows. Acording to Eq. (154), large values of $z(x;E)$ are reached if x is close to a point x_i where $\psi_E(x_i) = 0$. In this case

$$z(x;E) = \frac{\psi_E'(x)}{\psi_E(x)} \approx \frac{1}{x-x_i}. \tag{162}$$

On the other hand, as stated above, the cumulative density of states is equal to the density of zeros of $\psi_E(x)$. In other words, the probability to find a zero of $\psi_E(x)$ in an interval $[x, x+\mathrm{d}x]$ is given by $\overline{N(E)}\mathrm{d}x$. Thereby, the expectation value in Eq. (155) can be evaluated as follows:

$$P_0(z,x) = \overline{N(E)}\int_{x-\Delta x}^{x} \mathrm{d}x_i \delta\left(z - \frac{1}{x-x_i}\right) = \frac{\overline{N(E)}}{z^2}, \text{ if } z > 1/\Delta x. \tag{163}$$

which finally yields Eq. (161).

In [25], an analytic solution for Eqs. (158-160) is derived, from which $\overline{N(E)}$ follows as:

$$\overline{N(E)} = \frac{(D/4)^{1/3}}{\pi^2\left\{\mathrm{Ai}^2\left[-E\left(\frac{16}{D^2}\right)^{1/3}\right] + \mathrm{Bi}^2\left[-E\left(\frac{16}{D^2}\right)^{1/3}\right]\right\}}, \tag{164}$$

where Ai and Bi denote Airy functions of the first and second kind, respectively.

This result can be written as the imaginary part of the following complex function:

$$F(E) = \frac{D^{1/3}}{4^{1/3}\pi} \frac{\mathrm{Ai}'\left[-E\left(\frac{16}{D^2}\right)^{1/3}\right] + i\mathrm{Bi}'\left[-E\left(\frac{16}{D^2}\right)^{1/3}\right]}{\mathrm{Ai}\left[-E\left(\frac{16}{D^2}\right)^{1/3}\right] + i\mathrm{Bi}\left[-E\left(\frac{16}{D^2}\right)^{1/3}\right]}, \tag{165}$$

which fulfills all the conditions discussed in the paragraph after Eq. (152) above. Therefore, the Lyapunov exponent results from the real part of this function as follows:

$$\gamma(E) = \left(\frac{D}{4}\right)^{1/3} \frac{M'\left[-E\left(\frac{16}{D^2}\right)^{1/3}\right]}{M\left[-E\left(\frac{16}{D^2}\right)^{1/3}\right]}, \tag{166}$$

where $M(y) = \sqrt{\mathrm{Ai}^2(y) + \mathrm{Bi}^2(y)}$.

5.5 INTERPOLATION METHOD FOR CORRELATED POTENTIALS

Eq. (166) is exact for the white noise potential. Our idea is now to choose the strength D of the white noise in such a way that, for a given energy E, the Lyapunov exponent of the white noise potential agrees with the one of our correlated potential. For this purpose, we first look at the asymptotic bevaviour of $\gamma(E)$, given by Eq. (166), for large energies:

$$\gamma(E) \underset{E\to\infty}{\longrightarrow} \frac{D}{16E}. \tag{167}$$

In order to reproduce the result of the Born approximation, we therefore choose $D = 16E\gamma_{\mathrm{Born}}(E)$, or, taking into account Eqs. (142,143):

$$\begin{aligned} D &= 2\int_{-\infty}^{\infty} \mathrm{d}x\; C_2(x)\cos\left(2\sqrt{E}x\right), \\ &= 2\sqrt{2\pi}\sigma_c V_0^2 e^{-2\sigma_c^2 E}. \end{aligned} \tag{168}$$

As already mentioned above, the Born approximation is valid for large energies $E \gg E_{\mathrm{min}}^{(1)}$, where $E_{\mathrm{min}}^{(1)} = (\sigma_c V_0^2)^{2/3}$. On the other hand, we can also define a regime of low energies $E \ll E_{\mathrm{max}}^{(2)}$ where $E_{\mathrm{max}}^{(2)} = \sigma_c^{-2}$. This corresponds to the condition that the wave length $\lambda_E = 2\pi/p_E$ is much larger than the correlation length σ_c. In this regime, the wave is not able to resolve the correlations of the potential, which can therefore be approximated by a white noise potential $C_2(x) = D\delta(x)/2$, with

$D/2 = \int_{-\infty}^{\infty} \mathrm{d}x\, C_2(x) = 2\sqrt{2\pi}\sigma_c V_0^2$. This again agrees with Eq. (168) for $E\sigma_c^2 \ll 1$. Thus, Eq. (168) together with Eq. (166) yields a good approximation for the Lyapunov exponent, both, for high and for low energies. Moreover, remember that we assumed $V_0\sigma_c^2 \ll 1$, which is equivalent to $E_{\mathrm{min}}^{(1)} \ll E_{\mathrm{max}}^{(2)}$. Since this implies that the two above regimes overlap, our approximation is expected to hold in the entire range of energies.

This expectation is confirmed by numerical calculations of the Lyapunov exponent using the transfer matrix method [5], see Fig. (16). We see that our above analytical expression, Eq. (166) together with Eq. (168) (solid lines), agrees well with the numerical results (dots) in the entire range of energies, in particular also for negative energies. In contrast, the Born approximation (dashed lines) exhibits a divergence at low energies.

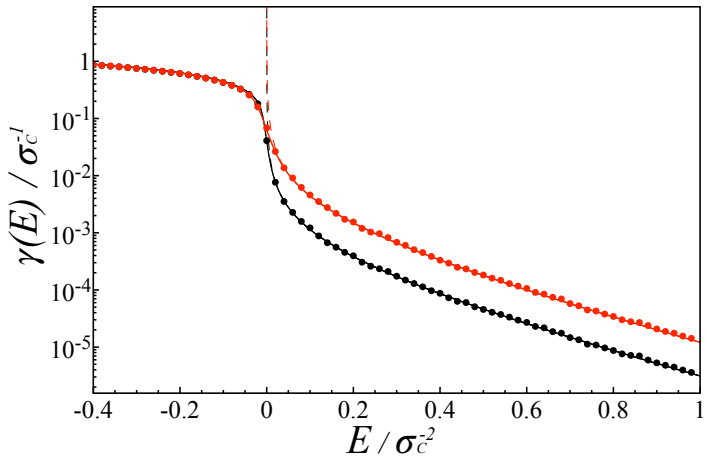

Fig. (16) Lyapunov exponent (in units of σ_c^{-1}) as a function of energy (in units of σ_c^{-2}) for two different strengths of the random potential, $V_0\sigma_c^2 = 0.0165$ (black) and $V_0\sigma_c^2 = 0.0325$ (red – light gray), both of which fulfill the condition $V_0\sigma_c^2 \ll 1$ of a weak random potential. Our analytical prediction (solid lines), based on the exact expression for a white noise potential, Eq. (166), with noise strength D chosen according to Eq. (168), agrees well with the result of numerical transfer matrix calculations (dots) in the entire range of energies, and for both values of the potential. In contrast, the Born approximation, Eq. (143) (dashed lines) exhibits a divergence at $E \to 0$.

6

SPECTRAL FUNCTION

The discussion in Sec. 2.2 made clear that previous attempts [27], [28] to describe the average asymptotic density profile of a wavepacket expanding in a one-dimensional disordered potential, using the ansatz given by Eq. (9), fail in the center of the distribution. This failure has its origin in the divergence, at small values of the energy, of the expressions for the Lyapunov coefficient and the spectral function used in [28] and [27]. In the previous chapter, we discussed the importance of the Lyapunov exponent as a quantity that characterizes the exponentially decaying eigenstates of the Hamiltonian, Eq. (15), for a particle in a disordered potential. Moreover, we found an analytical expression, see Eqs. (166 – 168), for a one-dimensional Gaussian random potential fulfilling the condition $V_0\sigma_c^2 \ll 1$, that agrees well with the numerics for all energies.

In the present chapter, we will consider the spectral function $A(p, E)$ describing the relation between energy and momentum in the presence of a random potential, which is another ingredient needed to determine the asymptotic density profile according to Eq. (9). In order to accomplish this task, we first present the general definition of the spectral function and introduce, as an example, the spectral function for the free particle and the corresponding energy probability distribution $P(E)$ with respect to a given initial state in Sec. 6.1. Afterwards, we calculate the average spectral function in the presence of a random potential using the Born approximation (as also proposed in [28]), and show that this expression diverges in the low energy regime, and vanishes for negative energies. However, we expect that the existence of negative energies – originating from cases where the particle is trapped inside a deep well of the random potential – will play an important role for correctly describing the center of the asymptotic density profile. To treat this problem, we will develop a version of the self-consistent Born approximation in Sec. 6.3. In contrast to the standard self-consistent Born approximation [73], [74], our version, where only the diverging part $1/\sqrt{E}$ of the self-energy is treated in a self-consistent way, allows us to finally derive an analytical expression for the spectral function, which does not diverge for low energies.

6.1 DEFINITION

The average spectral function $A(p, E)$ describes the relation between energy and momentum in the presence of the random potential. In order

to motivate this function, let us start with the following definition of the average energy distribution with respect to a given initial state $|\psi_0\rangle$:

$$P(E) = \overline{\langle\psi_0|\delta(E-H)|\psi_0\rangle} = \overline{\sum_n |\langle\psi_0|\phi_n\rangle|^2 \delta(E-E_n)} \tag{169}$$

describing the ensemble-averaged overlap of the initial state with energy eigenstates of a given energy E. Due to energy conservation, this distribution remains constant as a function of time, i.e. the same function $P(E)$ also describes the energy distribution with respect to the state $|\psi(t)\rangle = \exp(-itH)|\psi_0\rangle$ at time t. Using the representation

$$\delta(E-E_n) = -\lim_{\eta\to 0}\frac{1}{2\pi i}\left(\frac{1}{E-E_n+i\eta} - \frac{1}{E-E_n-i\eta}\right) \tag{170}$$

of the δ-function, and

$$\frac{1}{E-E_n+i\eta} = \langle\phi_n|G^{(\pm)}(E)|\phi_n\rangle, \tag{171}$$

see Eq. (48), we can reformulate Eq. (169) in terms of average Green functions:

$$P(E) = -\frac{1}{2\pi i}\left\langle\psi_0\left|\overline{G_E^{(+)} - G_E^{(-)}}\right|\psi_0\right\rangle, \tag{172}$$

see Eq. (48). Now, we make use of the fact that, due to translational invariance induced by the average, the average Green function is diagonal in momentum space, see Eq. (72), in order to arrive at:

$$\begin{aligned} P(E) &= -\frac{1}{2\pi i}\int_{-\infty}^{\infty} \mathrm{d}p\ |\tilde{\psi}_0(p)|^2 \left(\tilde{G}^{(+)}(p,E) - \tilde{G}^{(-)}(p,E)\right) \\ &= \int_{-\infty}^{\infty} \mathrm{d}p\ |\tilde{\psi}_0(p)|^2\ A(p,E) \end{aligned} \tag{173}$$

where we defined the spectral function:

$$A(p,E) = -\frac{1}{\pi}\Im\{\overline{\tilde{G}^{(+)}(p,E)}\}. \tag{174}$$

Since, as explained in Sec. 3.3.3, the average Green function can be expressed in terms of the self-energy $\Sigma^{(+)}(p,E)$, see Eq. (67), we can rewrite the spectral function as:

$$A(p,E) = -\frac{1}{\pi}\frac{\Im\{\tilde{\Sigma}^{(+)}(p,E)\}}{[E-p_E^2-\Re\{\tilde{\Sigma}^{(+)}(p,E)\}]^2 + \Im\{\tilde{\Sigma}^{(+)}(p,E)\}^2}, \tag{175}$$

where $\Re\{\tilde{\Sigma}^{(+)}(p,E)\}$ and $\Im\{\tilde{\Sigma}^{(+)}(p,E)\}$ are the real and imaginary part of the self-energy.

From Eq. (173), we see that the spectral function can be used to transform the momentum distribution $|\tilde{\psi}_0(p)|^2$ into an energy distribution. In other words, the function $A(p,E)$ denotes the probability that a state with momentum p has energy E. Indeed, $A(p,E)$ fulfills all requirements of a probability distribution (for E): first, it is positive, i.e. $A(p,E) \geq 0$, and second, it is normalized:

$$\int_{-\infty}^{\infty} \mathrm{d}E\; A(p,E) = 1. \tag{176}$$

The normalization, Eq. (176), follows from Eq. (173), since, according to Eq. (169), also $P(E)$ is normalized for every normalized initial state $|\psi_0\rangle$.

After integration over the momentum p, the spectral function $A(p,E)$ yields the average density of states $\overline{\rho_E}$, see Eq. (4):

$$\overline{\rho_E} = \int_{-\infty}^{\infty} \frac{\mathrm{d}p}{2\pi}\; A(p,E). \tag{177}$$

This follows from Eqs. (173) when choosing the initial state $|\psi_0\rangle = |x\rangle$ as a position eigenstate, which exhibits a constant momentum distribution $|\tilde{\psi}_0(p)|^2 = 1/(2\pi)$. Then, the energy distribution $P(E)$, see Eq. (169), reduces to the average density of states $\overline{\rho_E}$, see Eq. (4).

Spectral function of a free particle

Following the definition for the spectral density given in Eq. (174), but applying it to the free particle Green function or Eq. (54), we obtain:

$$A_0(p,E) = -\frac{1}{\pi}\Im\{\tilde{G}_0^{(+)}(p,E)\} = \frac{1}{\pi}\frac{\eta}{(E-p)^2-\eta^2} = \delta(E-p^2), \tag{178}$$

where the Dirac δ-function is obtained via Eq. (170) in the limit $\eta \to 0$. Thereby, we have reproduced Eq. (11).

In [27], the spectral density is approximated by the free particle description, see Eq. (11). The corresponding approximation for the energy distribution, Eq. (173), when we use the Fourier transform of Eq. (19) as initial momentum distribution, is:

$$P_0(E) = \begin{cases} \frac{a}{\sqrt{2\pi E}} e^{-a^2 E/2}, & \text{for } E > 0. \\ 0, & \text{for } E < 0, \end{cases} \tag{179}$$

where a is the width of the initial wavepacket in position space.

The spectral density of a free particle results as:

$$\rho_0(E) = \int_{-\infty}^{\infty} \frac{\mathrm{d}p}{2\pi}\; A_0(p,E) = \begin{cases} \frac{1}{2\pi\sqrt{E}}, & \text{for } E > 0. \\ 0, & \text{for } E < 0, \end{cases} \tag{180}$$

Note that, both, the energy distribution $P_0(E)$, see Eq. (179), and the density of states $\rho_0(E)$, see Eq. (180), for a free particle in one dimension diverge like $1/\sqrt{E}$ as the energy E tends to zero, and vanish for $E < 0$.

6.2 BORN APPROXIMATION

The Born approximation is the simplest method in order to evaluate the effect of the random potential on the average spectral function. Above, we have seen that the spectral function can be expressed in terms of the self-energy, see Eq. (175). As explained in Sec. 3.3.3, the self-energy, in turn, results from a sum over all irreducible diagrams, see Eq. (65). The Born approximation consists of taking only the first term, which amounts to an expansion of the self-energy up to second order in the potential V, i. e., $\Sigma^{(+)}_{\text{Born}}(E) = \overline{VG^{(+)}_0(E)V}$. Moreover, we use the approximation, already introduced in Sec. 3.3.3, according to which the dependence of the self-energy on the momentum p is neglected by setting $p = p_E = \sqrt{E}$. Thereby, we obtain:

$$\Sigma^{(+)}_{\text{Born}}(E) = \int_{-\infty}^{\infty} \mathrm{d}x\; C_2(x)\; e^{ip_E x} G^{(+)}_0(x, E), \tag{181}$$

$$= \frac{d(E)}{i\sqrt{E}}, \tag{182}$$

where:

$$d(E) = \frac{\pi\sigma_c V_0^2}{4}\left[1 + e^{-2E\sigma_c^2}\left(1 + i\,\mathrm{erfi}\left(\sqrt{2E}\sigma_c\right)\right)\right], \tag{183}$$

with imaginary error function $\mathrm{erfi}(z)$. Similarly as in the case of the Lyapunov exponent, Eq. (143), the Born approximation is valid only for high energies, and a divergence proportional to $1/\sqrt{E}$ is observed for $E \to 0$, see Eq. (182).

Fig. (17) shows a plot of the real and the imaginary part of $d(E)$. For large E, the function $d(E)$ converges to a constant value $\pi\sigma_c V_0^2/4$. According to Eq. (182), this gives rise to a self-energy with negative imaginary part and vanishing real part. For $E < 0$, the function $d(E)$ assumes real, positive values, see Fig. (17). Since $i\sqrt{E} = -\sqrt{|E|}$ for $E < 0$, also the imaginary part of the self-energy vanishes in this case. Therefore, in the Born approximation, the spectral function $A(p, E)$, as well as the average density of states $\overline{\rho_E}$, vanish for negative energies $E < 0$.

6.3 SELF-CONSISTENT BORN APPROXIMATION

A more precise estimation, which yields a non-vanishing density of states also for negative energies, is obtained by the self-consistent Born

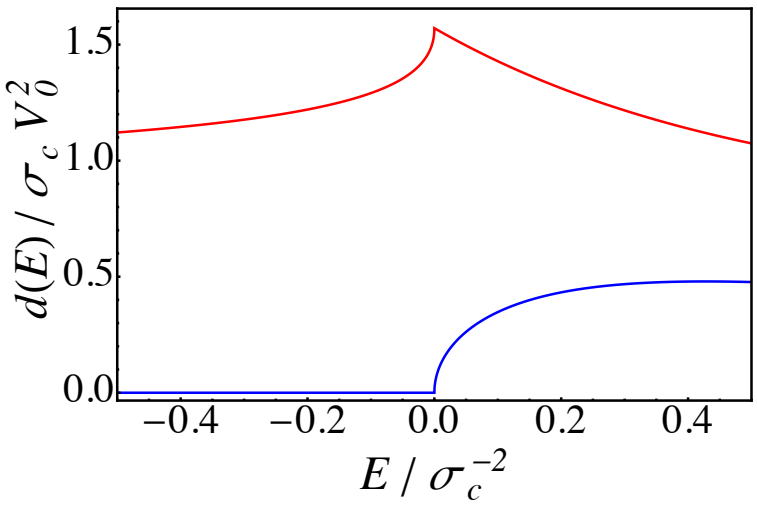

Fig. (17) $d(E)$ (in units of $\sigma_c V_0^2$) as a function of energy (in units of σ_c^{-2}). The red curve is the real part of $d(E)$, while the blue curve is the imaginary part of $d(E)$.

approximation, where the free-particle Green function $G_0^{(+)}(E)$ in Eq. (181) is replaced by the average Green function $\overline{G^{(+)}(E)}$, Eq. (77), which, in turn, depends on the self energy, see Eq. (78). The resulting self-consistent equation for $\Sigma(E)$, however, cannot be analytically solved.

Since, as pointed out above, the divergence of the Born approximation at low energies arises from the denominator $1/p_E = 1/\sqrt{E}$ in Eq. (182), our approach in order to obtain an analytical result is to treat only this denominator in a self-consistent way. We therefore replace $1/p_E \to 1/\tilde{p}_E$, i.e. $1/\sqrt{E} \to 1/\sqrt{E - \Sigma^{(+)}(E)}$, see Eq. (78), in the denominator of Eq. (182), and obtain the following self-consistent equation for Σ:

$$\Sigma^{(+)}(E) = \frac{d(E)}{i\sqrt{E - \Sigma^{(+)}(E)}}. \tag{184}$$

This equation has the following unique solution with negative imaginary part:

$$\Sigma^{(+)}(E) = [d(E)]^{2/3} \left(\frac{\epsilon}{3} + \frac{(-1)^{2/3}\epsilon^2}{3\left(\epsilon^3 + \frac{3}{2}\left(9 + \sqrt{81 + 12\epsilon^3}\right)\right)^{1/3}} - \frac{1}{3}(-1)^{1/3}\left(\epsilon^3 + \frac{3}{2}\left(9 + \sqrt{81 + 12\epsilon^3}\right)\right)^{1/3} \right), \tag{185}$$

where:

$$\epsilon = \frac{E}{[d(E)]^{2/3}}. \tag{186}$$

Together with Eq. (175), this concludes our analytic calculation of the spectral function. For large E, the result of the self-consistent Born approximation converges to the one of the ordinary Born approximation, see also Fig. (18) in the subsequent chapter. For $E < 0$, the imaginary part of $\Sigma^{(+)}$ as given by Eq. (185) vanishes for $E < E_{\min}$, where $E_{\min}$ is determined by the condition:

$$-\frac{3}{2^{2/3}} = \frac{E_{\min}}{[d(E_{\min})]^{2/3}} \tag{187}$$

For $V_0\sigma_c^2 \ll 1$, we may replace $d(E_{\min}) \simeq d(0) = \pi\sigma_c V_0^2/2$ in Eq. (187), and obtain:

$$E_{\min}\sigma_c^2 \simeq -3\left(\frac{\pi}{4}\right)^{2/3}\left(V_0\sigma_c^2\right)^{4/3} \tag{188}$$

Finally, the energy distribution $P(E)$ of our wave packet is extracted from the spectral function according to Eq. (173). Using the Fourier transform of our initial state, Eq. (19), the integral over p can be performed analytically:

$$P(E) = \frac{a}{\sqrt{\pi}}\Im\left\{\frac{e^{a^2\left(\Sigma^{(+)}(E)-E\right)}\operatorname{erfc}\left(a\sqrt{\Sigma^{(+)}(E)-E}\right)}{\sqrt{\Sigma^{(+)}(E)-E}}\right\}, \tag{189}$$

with complementary error function $\operatorname{erfc}(z)$. As we have checked, this expression, with $\Sigma^{(+)}(E)$ given by Eq. (185), yields a normalized distribution [25], i. e., $\int_{-\infty}^{\infty} \mathrm{d}E\; P(E) = 1$, which underlines the consistency of our approach. Its quality in terms of agreement with numerical data will be discussed in Subs. 7.3.1.

7 COMPARISON BETWEEN THEORY AND NUMERICS

In this chapter, we present the numerical results for the average asymptotic density $\overline{n(x)}$ of a wave packet in a one-dimensional disordered potential, starting from a spatially strongly confined Gaussian wave packet as initial state, and we compare it with the theoretical description developed in the previous Chapters 4-6.

First, we give a short summary of the theoretical description in Sec. 7.1, where, for the sake of clarity, we collect all relevant equations needed for the theoretical calculation of the average density profile in a single subchapter.

The algorithm used for the numerical calculations is briefly discussed in Sec. 7.2. Finally, the numerical and theoretical results are presented and compared with each other in Sec. 7.3, first for the energy distribution $P(E)$ (Subs. 7.3.1), and then for the asymptotic density profile $\overline{n(x)}$ (Subs. 7.3.2). We will see that, for the range of parameters for which the theory has been developed (i.e. initial size a of the wavepacket much smaller than the localization length, $a \ll L_{\mathrm{loc}}$, and a random potential with small standard deviation and/or short correlation length, $V_0\sigma_c^2 \ll 1$), a good overall agreement between theory and numerics is achieved without any fitting parameter. Small deviations resulting from the finite size of the numerical system are explained in Subs. 7.3.3, where we present a comparion between theory and numerics in different energy intervals.

7.1 SUMMARY OF THEORETICAL RESULTS

As explained in the previous chapters, we consider a particle in a one-dimensional random potential, described by the Hamiltonian

$$H = p^2 + V(x),$$

($\hbar = 2m = 1$), see Eq. (15). The initial state is a Gaussian wave packet with width a:

$$\psi_0(x) = \langle x|\psi_0\rangle = \left(\frac{1}{\pi a^2}\right)^{1/4} e^{-x^2/(2a^2)},$$

see Eq. (19). The random potential $V(x)$ is modelled as a Gaussian stochastic process, see Subs. 3.2.2, with mean value $\overline{V(x)} = 0$ and Gaussian two-point correlation function:

$$\overline{V(x)V(x')} = V_0^2 e^{-|x-x'|^2/(2\sigma_c^2)},$$

(standard deviation V_0 and correlation length σ_c), see Eq. (30).

Our purpose is to describe the average density profile in the limit of long times:

$$\overline{n(x)} = \lim_{T\to\infty} \frac{1}{T} \int \mathrm{d}t \; \overline{|\langle x\,|e^{-iHt}|\,\psi_0\rangle|^2}$$

see Eqs. (21,22). Using the diagrammatic method of Berezinskii in Chapter 5, we arrived at Eq. (9) as one of the central results of this thesis. For the case of an initially strongly confined wave packet, we can neglect the dependence of $\overline{n_E(x-q)}$ on the initial position q. The integral over q in Eq. (9) then yields the momentum distribution $|\tilde{\psi}(p)|^2 = \int \mathrm{d}q \; W(q,p)$, and the integral over p the energy distribution $P(E)$, see Eq. (173). Furthermore, in order to compare with numerical results (see below), we take into account periodic boundary conditions (with period L) and modify Eq. (9) as follows:

$$\overline{n(x)} = \int_{-\infty}^{\infty} \mathrm{d}E \; P(E) \sum_{j=-\infty}^{\infty} \overline{n_E(x+jL)}, \quad -\frac{L}{2} \ll x \ll \frac{L}{2}. \tag{190}$$

where $P(E)$ denotes the energy distribution of our wave packet, and $n_E(x)$ the density-density autocorrelation function at fixed energy. The latter is given by:

$$\begin{aligned} \overline{n_E(x)} \;&=\; \frac{\pi^2\gamma(E)}{8} \int_0^\infty du \; u \sinh(\pi u) \left[\frac{1+u^2}{1+\cosh(\pi u)}\right]^2 \\ &\times\; \exp\{-(1+u^2)\gamma(E)|x|/2\} \end{aligned}$$

see Eq. (5). The Lyapunov exponent $\gamma(E) = 1/L_{\mathrm{loc}}(E)$ was obtained in Chapter 5 by an interpolation between the Born approximation and the exact result for white noise (valid in the entire range of energies under the condition $V_0\sigma_c^2 \ll 1$):

$$\gamma(E) = \left(\frac{D(E)}{4}\right)^{1/3} \frac{M'\left[-E\left(\frac{16}{D(E)^2}\right)^{1/3}\right]}{M\left[-E\left(\frac{16}{D(E)^2}\right)^{1/3}\right]},$$

where $M(y) = \sqrt{\mathrm{Ai}^2(y) + \mathrm{Bi}^2(y)}$, see Eq. (166), and

$$D(E) = 2\sqrt{2\pi}\sigma_c V_0^2 e^{-2\sigma_c^2 E}$$

see Eq. (168). Finally, the energy distribution was obtained using a modified version of the self-consistent Born approximation in Chapter 6:

$$P(E) = \frac{a}{\sqrt{\pi}} \Im \left\{ \frac{e^{a^2\left(\Sigma^{(+)}(E)-E\right)} \mathrm{erfc}\left(a\sqrt{\Sigma^{(+)}(E)-E}\right)}{\sqrt{\Sigma^{(+)}(E)-E}} \right\}$$

see Eq. (189), where the self-energy is given by:

$$\Sigma^{(+)}(E) = [d(E)]^{2/3} \left(\frac{\epsilon}{3} + \frac{(-1)^{2/3}\epsilon^2}{3\left(\epsilon^3 + \frac{3}{2}\left(9 + \sqrt{81 + 12\epsilon^3}\right)\right)^{1/3}} - \frac{1}{3}(-1)^{1/3}\left(\epsilon^3 + \frac{3}{2}\left(9 + \sqrt{81 + 12\epsilon^3}\right)\right)^{1/3} \right),$$

see Eq. (185), with:

$$\epsilon = \frac{E}{[d(E)]^{2/3}}$$

and

$$d(E) = \frac{\pi\sigma_c V_0^2}{4}\left[1 + e^{-2E\sigma_c^2}\left(1 + i\,\mathrm{erfi}\left(\sqrt{2E}\sigma_c\right)\right)\right],$$

see Eq. (183) and Eq. (186).

Except for Eq. (5) and Eq. (190), all results are given in an explicit and analytical form. The former two equations correspond to one-dimensional integrations, which can easily be performed numerically. Moreover, the function $n_E(x)$ defined by Eq. (5) is scale-invariant. Therefore, it is sufficient to evaluate this function, the shape of which is shown in Fig. (5), one single time for a given energy E_0. Then, $n_E(x)$ for arbitrary E can be obtained as $n_E(x) = \frac{\gamma_E}{\gamma_{E_0}} n_{E_0}\left(\frac{\gamma_E}{\gamma_{E_0}} x\right)$. In summary, our theory thus allows us to reduce the computation of the average asymptotic density profile to a single, one-dimensional integral given by Eq. (190).

7.2 NUMERICAL ALGORITHM

Below, we will test the validity of our theory presented above by comparison with numerical results obtained from exact diagonalization of the Hamiltonian, Eq. (15), for individual realizations of the random potential $V(x)$. The numerical algorithm for producing Gaussian random potentials with the correlation function given above has already been explained in Subs. 3.2.2. We then calculate the spectrum $\{E_n\}$ and corresponding eigenfunctions $\{|\phi_n\rangle\}$ for many different realizations of the random potential $V(x)$. From these, the desired quantities are extracted as follows:

$$P(E) = \overline{\sum_{n=1}^{M} |\langle\psi_0|\phi_n\rangle|^2\,\delta(E - E_n)}$$

for the energy distribution, see Eq. (169), and

$$\overline{n(x)} = \sum_{n=1}^{M} \overline{|\langle x|\phi_n\rangle\langle\phi_n|\psi_0\rangle|^2}$$

see Eq. (24) for the asymptotic density profile. (The latter depends only on the eigenfunctions, and not on the energies.) To compute the ensemble average, the diagonalization must be repeated for a large ensemble (typically, several hundreds or thousands) of random Hamiltonians.

For the diagonalization, we use a finite-element discrete variable representation (FEDVR) [75]–[77]. Our system of length $L = 800\sigma_c$ (i. e. much larger than the correlation length σ_c) is divided into 10^4 finite elements of size $0.08\sigma_c$ (i. e. much smaller than σ_c). Each element, in turn, is discretized using 5 basis functions (among them 2 bridge functions which connect this element to the neighbouring ones) [76], [77]. Thereby, the Hamiltonian is represented as a matrix of dimension $M = 4 \times 10^4$, which can be diagonalized numerically. As already mentioned in Subs. 3.1.2, we use periodic boundary conditions, i. e., the point $x = -L/2$ is identical to the point $x = L/2$. More details concerning the basis functions in the finite-element discrete variable representation are explained in Appendix C.

7.3 RESULTS

7.3.1 *Energy distribution*

Let us start with the energy distribution $P(E)$ discussed in Chapter. 6.

Fig. (18) shows the numerical result (dotted lines) together with our analytical prediction, Eq. (189) (solid lines), for initial width $a = \sqrt{2}\sigma_c$ and two different values of the potential $V_0 = 0.0165\sigma_c^{-2}$ (black) and $V_0 = 0.0325\sigma_c^{-2}$ (red). In addition, we also show the energy distribution of a free particle, Eq. (115) (blue dashed line). As expected, all curves agree well for energies larger than V_0. For smaller energies, the free-particle distribution exhibits a divergence if $E \to 0$. In contrast, our version of the self-consistent Born approximation reproduces well the numerical distribution in the entire range of positive energies. For negative energies, the agreement is less precise, due to the fact that, as discussed in Sec. 6.3, our analytical result exhibits a sharp cutoff at a certain minimum energy $E_{\min}\sigma_c^2 \simeq -3\left(\frac{\pi}{4}\right)^{2/3}\left(V_0\sigma_c^2\right)^{4/3}$, see Eq. (188), whereas the numerical distribution decays smoothly with decreasing energy. We note that a more accurate description in the range of negative energies can be achieved by a recently developed semiclassical approach [78]. This difference, however, does not significantly affect the shape of the asymptotic state, which, according to our theory, depends on $P(E)$ only through the energy dependence of the Lyapunov exponent $\gamma(E)$, which is not very pronounced in the relevant regime of negative energies, see Fig. (16).

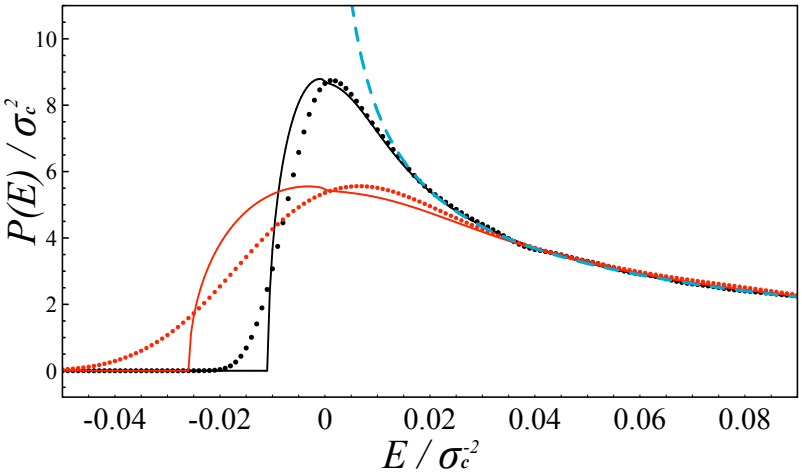

Fig. (18) Energy probability distribution, $P(E)$ (in units of σ_c^2), as a function of energy (in units of σ_c^{-2}) for width $a = \sqrt{2}\,\sigma_c$ of the initial wave packet and two different strengths of the random potential, $V_0 = 0.0165\sigma_c^{-2}$ (black) and $V_0 = 0.0325\sigma_c^{-2}$ (red). The results of the numerical diagonalization (dotted lines), averaged over 2000 realizations of the random potential and, in addition, smoothed by an exponentially moving average with smoothing constant 0.007, agree well with our analytical prediction (solid lines) based on the self-consistent Born approximation, Eq. (189), for positive energies. For negative energies, the theory exhibits a sharp cutoff which is not present in the numerical data. For large energies ($E > V_0$), all curves converge to the distribution $P_0(E)$ of a free particle (blue dashed line).

7.3.2 *Asymptotic average density*

We now turn towards the main result of this thesis concerning the asymptotic average density $\overline{n(x)}$ defined in Sec. 2.1. Fig. (19) shows a comparison of our theoretical prediction based on Eq. (190) with the result extracted from numerically determined eigenfunctions according to Eq. (24). In addition, we also show the result of a simplified theory (used in [27]), where the energy distribution $P(E)$ in Eq. (190) is replaced by the free-particle distribution $P_0(E)$, see Eq. (115), and the Lyapunov exponent $\gamma(E)$ entering in Eq. (5) is replaced by its Born approximation $\gamma_{\text{Born}}(E)$, see Eq. (143).

Overall, we see that our theory (solid lines) gives a good description of the numerical data (squares), both, in the wings of the spatial profile and, remarkably, also close to the center of the wave packet (inset). Due to Eq. (8), our theory predicts a linear decay of the profile at small x, which can be evaluated by integrating Eq. (8) over E, see Eq. (190). (Note that only the term $j = 0$ gives a significant contribution in the center.) In contrast, the simplified theory agrees with our improved theory in the

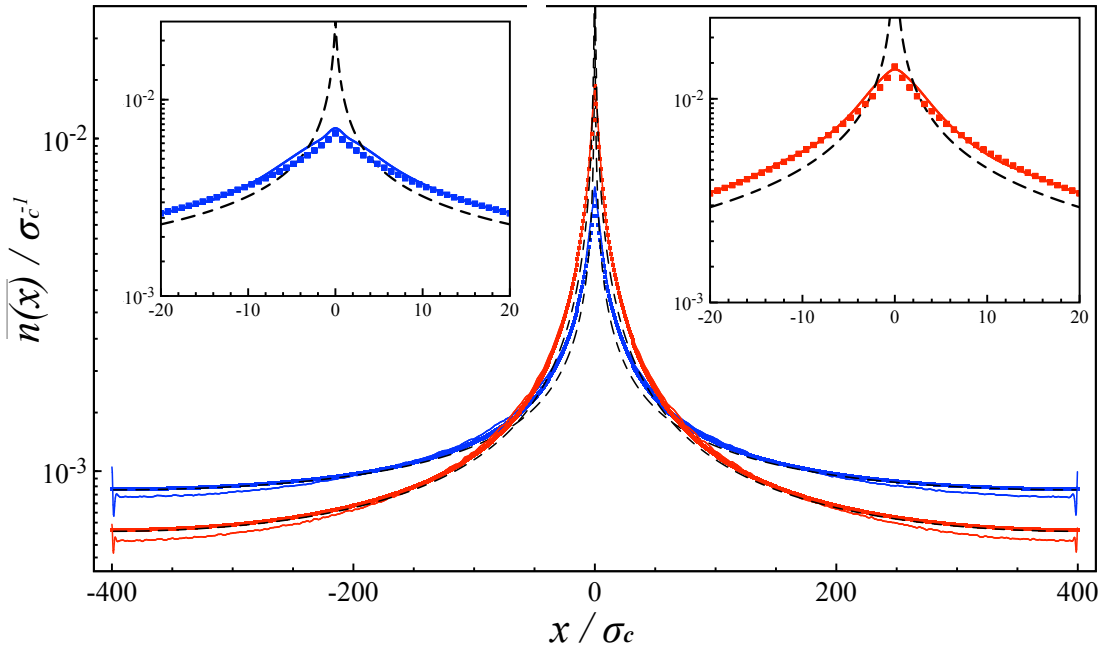

Fig. (19) Numerical and analytical results for the asymptotic average density, $\overline{n(x)}$ (in units of σ_c^{-1}), as a function of position (in units of σ_c) for width $a = \sqrt{2}\,\sigma_c$ of the initial wave packet and two different strengths of the random potential, $V_0 = 0.0165\sigma_c^{-2}$ (blue) and $V_0 = 0.0325\sigma_c^{-2}$ (red). The numerical result given by Eq. (24) (solid lines), averaged over 2000 realizations of the random potential, agrees well with our theoretical description, Eq. (190) (squares), in particular also close to the center of the wave packet, without any fitting parameter. In contrast, a simplified version of the theory (black dashed lines) using the spectral distribution $P_0(E)$ of a free particle instead of $P(E)$, and the Born approximation $\gamma_{\text{Born}}(E)$ instead of the Lyapunov exponent $\gamma(E)$, predicts an unphysical divergence of the density at $x = 0$ (see inset).

wings, but fails in the center where it predicts an unphysical divergence as $x \to 0$.

Upon closer inspection, however, we note a small deviation between theory and numerics in the wings of the profile. Furthermore, the numerical data exhibit an interference feature at $x \simeq L/2$ and $x \simeq -L/2$, which is absent in our theory.

Before explaining the reason for these deviations, however, let us shortly comment on the behaviour of density fluctuations around the mean value depicted in Fig. (19). In the numerical data, we have averaged over 2000 realizations of the random potential. Such a large ensemble is necessary to obtain a precise estimate (with an accuracy of about two percent) of the average profile $\overline{n(x)}$ in the center, i. e. for $x \simeq 0$. The center of the profile is subject to large fluctuations, since it sensitively depends on the shape of the random potential at $x \simeq 0$. On

the other hand, the fluctuations become smaller for larger x, which is consistent with the fact that the localization length (which determines the exponential decay of the energy eigenfunctions at large distances) is a self-averaging quantity [60].

7.3.3 *Agreement theory vs. numerics in different energy intervals*

To explain the reason for the small differences between theory and numerics in Fig. (19), we split the average asymptotic density into different energy intervals, i. e., we define:

$$\overline{n^{(i)}(x)} = \overline{\sum_{n=1}^{\infty} |\langle x|\phi_n\rangle\langle\phi_n|\psi_0\rangle|^2 \theta(E_n - E_i)\theta(E_{i+1} - E_n)}, \tag{191}$$

with Heaviside function $\theta(E)$.

Eq. (191) is similar to Eq. (24), except for the fact that the sum is restricted to eigenstates with energies $E_n \in [E_i, E_{i+1}]$ inside a certain energy interval. We choose $E_1 = -\infty$, $E_2 = 0$, $E_3 = 0.103$, $E_4 = 0.178$ and $E_5 = 0.278$, $E_6 = 0.403$ and $E_7 = \infty$ (all in units of σ_c^{-2}), such that $\overline{n(x)} = \sum_{i=1}^{6} \overline{n^{(i)}(x)}$. The corresponding theoretical expression is constructed in a similar way from Eq. (190):

$$\overline{n^{(i)}(x)} = \int_{E_i}^{E_{i+1}} \mathrm{d}E\ P(E) \sum_{j=-\infty}^{\infty} \overline{n_E(x + jL)}. \tag{192}$$

Fig. 20(a-f) shows the corresponding comparison between theory and numerics in these six intervals. We observe very good agreement for negative energies, see Fig. (20 a), where the asymptotic density is strongly localized due to the presence of bound states in the random potential. This result is remarkable for two reasons: first, it shows that the deviations between the theoretical and the numerical energy distribution $P(E)$, see Subs. 7.3.1, have no significant impact on the spatial density profile. Second, remember that our theoretical approach is based on a diagrammatic method which takes into account only a certain class of diagrams (called 'essential diagrams' in Appendix A). As explained in the original article of Berezinskii [20], this restriction is, a priori, justified only for large energies. As our results show, however, the resulting expression for the spatial density profile $\overline{n_E(x)}$, Eq. (5), is valid also for low (and even negative) energies – provided that an accurate value of the Lyapunov exponent $\gamma(E)$ is used in Eq. (5). As mentioned in the discussion at the end of Subs. 4.1.4, this confirms the hypothesis of the one-parameter theory of localization [9], according to which the behaviour of physical quantities (e.g., the asymptotic density profile) should be governed by a single parameter (e.g. by the Lyapunov exponent $\gamma(E)$).

A similar reasoning applies to the interval of small positive energies, see Fig. 20(b). Deviations between theory and numerics become apparent, however, for larger energies, see Fig. 20(c-f). These can be traced back to the finite system size. Indeed, our simple way of taking into account the periodic boundary conditions, see the sum over j in Eq. (190), after first having calculated the density according to a theory which is valid for an infinite system, neglects the occurrence of interferences in the finite, periodic system, e. g., interference between amplitudes of paths which propagate to the right-hand side ($x = L/2$) or to the left-hand side ($x = -L/2$) respectively, or between paths which perform several 'loops' inside the periodic system. Such processes become relevant at high energies where the influence of the random potential becomes less important, and the particle behaves approximately like a free particle. To confirm this explanation, we also show the asymptotic density of a free particle within the corresponding energy intervals, where these interferences are clearly visible.

We note that our approach of taking into account the boundary conditions only at the end of the calculation (after having applied a theory valid for an infinite system) is only justified for the case of periodic boundary conditions, since the latter most closely resemble the behaviour of an infinite system (apart from the interferences discussed above). In case of different boundary conditions, which are not considered in this thesis (e. g. Neumann or Dirichlet), the diagrammatic calculation of $n_E(x)$ would have to be modified such as to include these conditions already from the start. Of course, the boundary conditions will affect the wings of the density profile close to the boundaries, whereas its center, which is determined by energy components with localization lengths much smaller than the system size, will essentially remain unaffected. Moreover, the fact that a rather good agreement between theory and numerics is observed in the entire range of energies in Fig. (20), proves that the localized density profile is not sensitive to the precise form of the initial state – provided that the initial state is strongly confined in position space, as assumed in the derivation of Eq. (9), and restricted to an energy range where the finite-size interference effects (see above) remain small.

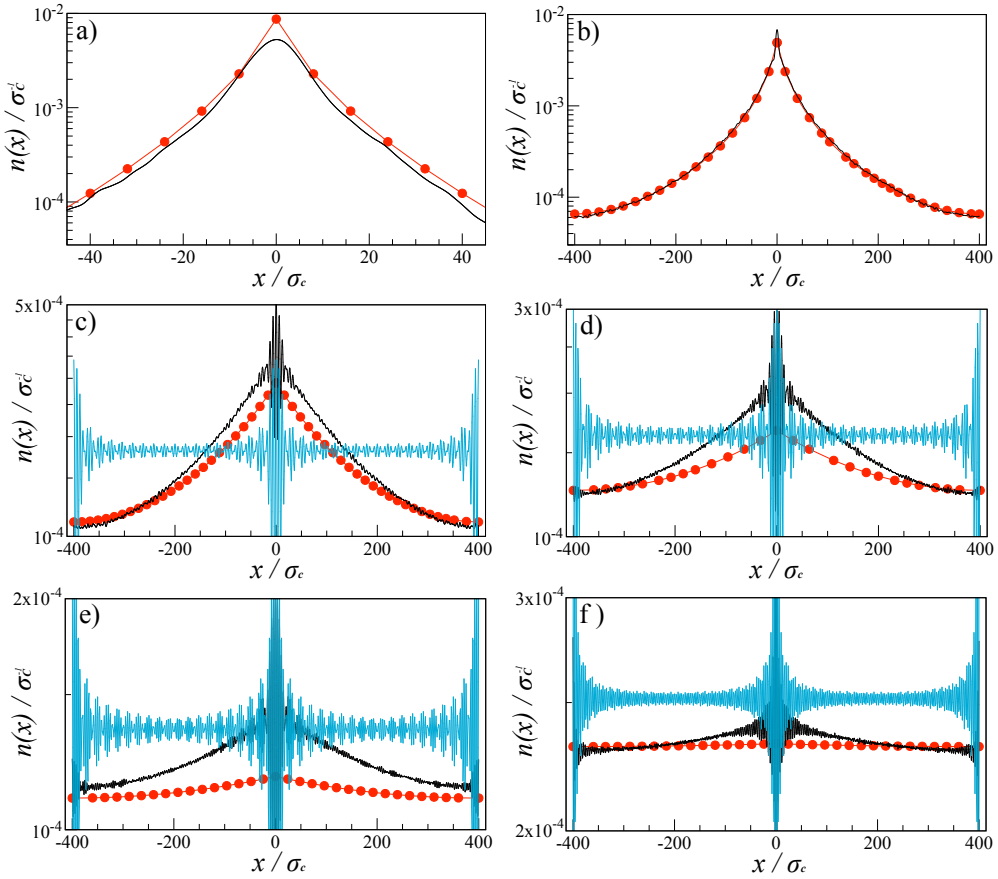

Fig. (20) Comparison between numerical (black) and theoretical (red line with dots) density profiles, $\overline{n^{(i)}(x)}$ (in units of σ_c^{-1}), as a function of position (in units of σ_c), see Eqs. (191,192), respectively, in different energy windows a) $(E_1, E_2) = (-\infty,\ 0)$, b) $(E_2, E_3) = (0,\ 0.103)$, c) $(E_3, E_4) = (0.103,\ 0.178)$, d) $(E_4, E_5) = (0.178,\ 0.278)$, e) $(E_5, E_6) = (0.278,\ 0.403)$, and f) $(E_6, E_7) = (0.403,\ \infty)$ (energies in units of σ_c^{-2}), for width $a = \sqrt{2}\sigma_c$ of the initial wave packet and strength $V_0\sigma_c^{-2} = 0.0325$ of the random potential. The numerical values have been extracted from the same data as the one used in Fig. (19) (red lines). Whereas good agreement is observed for low energies (a,b), differences are visible at larger energies (c-f), where the numerical data exhibits oscillations close to $x \simeq 0$ and $x \simeq \pm L/2$, which are not present in our theory. These oscillations can be traced back to interferences occurring due to the finite size of our system ($L = 800\sigma_c$) and the periodic boundary conditions, as can be deduced by comparion with the corresponding density of a free particle in the same energy windows (blue line).

8 INFLUENCE OF INTERACTIONS

As we already discussed in Sec. 2.1, the experiments that motivate this thesis were performed with an initially spatially trapped Bose-Einstein condensate (BEC), which starts to expand in a one-dimensional random potential as soon as the trap is released. After a certain time, the expansion of the condensate comes to a halt and a quasi-stationary density profile is observed. In Subs. 2.1.2 we discussed that, since the 1D random potential is in the weak disorder regime, the BEC quasi-stationary density profile can be understood as originating from destructive interference between multiply reflected wave amplitudes. In this regime, the supression of transport is therefore a consequence of Anderson localization [4], and cannot be understood in terms of classical reflection at high potential barriers. In the previous chapters, one of the main aims of the present thesis was achieved, i. e., to improve the existing theoretical description of Anderson localization in one-dimensional random potentials, in such a way, that we are able to describe the complete density profile of the asymptotic state. However, remember that the description in Chapters 3-7 is based on the linear Schrödinger equation for a single particle, see Eq. (16), and therefore does not consider the interactions between the bosons.

In this chapter, we will discuss the influence of interactions on the density profile of the BEC. We will treat these interactions on a mean-field level by including a nonlinear term into the Schrödinger equation, which is thereby transformed into the Gross-Pitaevskii equation (GPE) [79], [80], see Sec. 8.1. An important and fundamental question is whether the effect of Anderson localization still persists in the presence of nonlinearity. In other words, will there still exist a long-time asymptotic state as defined in Eq. (21), or will the condensate continue to expand even at long times? In Sec. 8.2, we will shortly summarize the result of previous works based on a discretized version of the Gross-Piatevskii equation. As we will see there, a sufficiently strong nonlinearity is indeed able to destroy the effect of Anderson localization, and induce a slow sub-diffusive spreading of the wave packet. For our case of a continous and correlated one-dimensional random potential, we would, in principle, expect a similar behaviour. Finding the answer to this question, however, would require to propagate the Gross-Pitaevskii equation for extremely long times (which is more difficult for a continous, disorderd system than for a discrete system).

In the present thesis, we will therefore restrict ourselves to a regime of intermediate time scales, which are, on the one hand, longer than the time scale needed to reach the stationay state for the linear system, but, on the other hand, shorter than the time scale of the sub-diffusive spreading mentioned above. Indeed, from an intuitive point of view, the strongest impact of the nonlinearity is expected at short times, where the density of the condensate is highest. In previous works [27], [28] (see also the corresponding discussion in Chapter 2), it was therefore suggested to describe the expansion of the condensate in two phases, see Sec. 8.3: at short times, the expansion is driven by the repulsive interaction between the atoms, and the influence of the disorder is neglected during this phase. At a certain time t_i, almost the entire interaction energy has been converted into kinetic energy. In the second stage, the interactions are therefore neglected, whereas the disorder becomes important. Our approach to calculate the density profile at intermediate times is to use the linear theory developed in the previous chapter – but using a suitably defined energy distribution $P_g(E)$, see Sec. 8.5, which is now a function of the interaction parameter g, in contrast to the old $P(E)$ introduced in Sec. 6.3.

8.1 GROSS-PITAEVSKII EQUATION

The general Hamiltonian for a system of N identical, interacting bosons is

$$H = \sum_{i=1}^{N} \left(\mathbf{p}_i^2 + V_{ext}(\mathbf{r}_i) \right) + \frac{1}{2} \sum_{i=1}^{N} \sum_{j \neq i}^{N} V(|\mathbf{r}_i - \mathbf{r}_j|), \tag{193}$$

where $\mathbf{p}_i^2$ is the kinetic energy of the i-th particle, V_{ext} represent the external potential and $V(|\mathbf{r}_i - \mathbf{r}_j|)$ is the interaction potential between i-th and j-th particles.

In order to reduce the N-particle description to an equation involving only single-particle wave functions, the mean-field ansatz is applied, according to which the N-particle state $|\Psi(t)\rangle$ at time t is approximated by a product of identical single-particle states $|\psi(t)\rangle$

$$|\Psi(t)\rangle \approx |\psi(t)\rangle \otimes |\psi(t)\rangle \otimes |\psi(t)\rangle \cdots \otimes |\psi(t)\rangle. \tag{194}$$

Furthermore, we assume that the interaction V in Eq. (193) is a short-range interaction, which can be treated as a point-like interaction potential. Under these assumptions, the time evolution of the single-particle state follows the Gross-Pitaevskii equation [79], [81], [82]

$$i\partial_t \psi(\mathbf{r}, t) = \left(-\nabla^2 + V_{ext}(\mathbf{r}) + \tilde{g}|\psi(\mathbf{r}, t)|^2 \right) \psi(\mathbf{r}, t), \tag{195}$$

where $\tilde{g}$ quantifies the strength of the interaction.

The corresponding time-independent equation, which can be used to determine the ground state of N interacting bosons in a trap reads [80], [81], [83]:

$$\left(-\nabla^2 + V_{ext}(\mathbf{r}) + \tilde{g}|\psi(\mathbf{r})|^2 \right)\psi(\mathbf{r}) = \mu\psi(\mathbf{r}), \tag{196}$$

with chemical potential μ. In this case, the mean-field description, see Eq. (194), is valid in the limit $N \to \infty$ and $\tilde{g} \to 0$ such that $N\tilde{g} =$ constant, see [80] for a rigorous derivation.

In the time-dependent case, the same limit ensures the validity of the time-dependent GPE Eq. (195), at finite times t [79]. It is important to note, however, that the limits $N \to \infty$ and $t \to \infty$ do not commute, i. e., for a given (large but finite) number N of particles, the GPE Eq. (195) may loose its validity in the limit $t \to \infty$, since collisions between particles may produce an increasing number of non-condensed particles [84]–[86].

Finally, we note that, in case of narrow transverse confinement (see Sec. 2.1), the GPE Eq. (195) can be reduced to the one-dimensional equation:

$$i\partial_t\psi(x,t) = \left(-\partial_x^2 + V_{ext}(x) + g|\psi(x,t)|^2 \right)\psi(x,t), \tag{197}$$

with effective interaction strength g (which depends on $\tilde{g}$ and the frequency $\omega_\perp$ of the transverse confining potential). We assume repulsive interactions $g > 0$ in the following.

This equation fulfills the properties of norm and energy conservation, i. e.

$$\partial_t N[\psi(t)] = 0 \tag{198a}$$

and

$$\partial_t E[\psi(t)] = 0, \tag{198b}$$

where the norm is defined as:

$$N[\psi(t)] = \int \mathrm{d}x\ |\psi(x,t)|^2, \tag{199}$$

and the energy by the following Gross-Pitaevskii energy functional:

$$E[\psi(t)] = \int \mathrm{d}x\ \psi^*(x)\left[\partial_x^2 + V_{ext}(x) + \frac{g}{2}|\psi(x,t)|^2\right]\psi(x,t). \tag{200}$$

Usually, the state ψ is normalized to the total number N of particles, i. e. $N[\psi] = N$. In order to compare with the non-interacting case, however, we will, in the following, use wavefunctions with norm 1, i. e. $N[\psi] = 1$, and rescale the strength of interactions, i. e. $g \to Ng$, in order to account for the number of particles.

8.2 LONG-TIME BEHAVIOUR: SUB-DIFFUSIVE SPREADING

Although, as discussed above, the Gross-Pitaevskii equation is, in principle, valid only for finite times, it is interesting, from a fundamental point of view, to investigate the behaviour of its solution in the limit of long times. This question has been addressed in [26] for a non-linear Schrödinger equation based on the discrete Anderson model (DANSE):

$$i\frac{\partial \psi_n}{\partial t} = E_n\psi_n + g|\psi_n|^2 + V(\psi_{n+1} + \psi_{n-1}), \tag{201}$$

where g characterizes the non-linearity, V is the hopping element between two lattice neighbors, and (as in the Anderson model [4]), the onsite-energies E_n are uniformly randomly distributed in the interval $[-E_0/2, E_0/2]$.

Eq. (201) is a discrete version of the above Gross-Pitaevskii equation for a particle in a continuous potential, see Eq. (197). The problem studied in [26] with Eq. (201) is the spreading of a field initially localized at site 0 (i. e. $|\psi_n(0)|^2 = \delta_{n,0}$), where, in all the numerical experiment, the total probability is normalized to unity, i. e., $\sum_n |\psi_n(t)|^2 = 1$. In [26], the authors compute the second moment in order to characterize the spreading of the wave packet over the lattice:

$$\sigma(t) = \overline{(\Delta n)^2} = \sum_n (n - \overline{\Delta n})^2 |\psi_n(t)|^2, \tag{202}$$

where $\overline{\Delta n} = \sum_n n|\psi_n(t)|^2$.

Figs. (21) and (22) show the dependence of $\log_{10}\sigma$ on time t for different values of the nonlinearity g and the strength E_0 of the disorder. In Fig. (21), the logarithm of σ was averaged over 8 realizations of the disorder, whereas the simulation was performed for a single disorder realization in Fig. (22).

In Fig. (21), the values of g are 0 (dots) and 1 (lines), while the values of E_0 are 2 (red) and 4 (blue). In the linear case ($g = 0$), the second moment σ reaches a stationary value at $t \simeq 96/E_0^2$. Before this time, the linear (dots) and the non-linear spreading (lines with $g = 1$) behave in a similar way, as was already predicted in [87]. From $t = 96/E_0^2$ on, the continuos lines ($g = 1$) exhibit no saturation of σ, and the wave packet continues to expand until $t = 10^8$ (the longest time considered in the simulation). This result is interpreted as a destruction of Anderson localization by the nonlinearity. The dashed lines show numerical fits $\log_{10}\sigma(t) = \alpha \log_{10} t + \eta$, where $\alpha = 0.344 \pm 0.003$, $\eta = 1.76 \pm 0.02$ were obtained for $\log_{10} t \in [3, 8]$ and $E_0 = 2$, while $\alpha = 0.306 \pm 0.002$, $\eta = 0.94 \pm 0.01$ were obtained for $\log_{10} t \in [2, 8]$ and $E_0 = 4$. The black line shows the theoretical slope $\alpha = 0.4$ characterizing the exponent of subdiffusive spreading as predicted by [88].

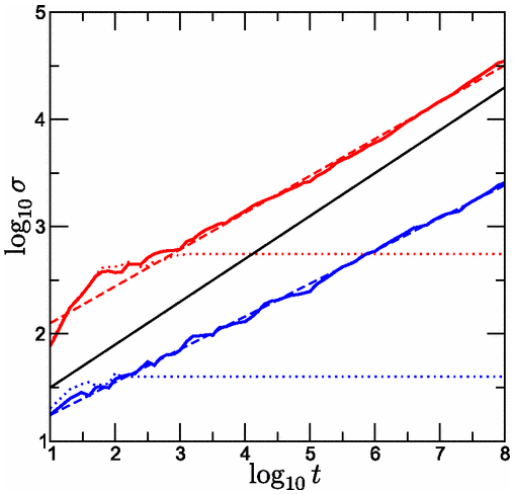

Fig. (21) Second moment σ characterizing the spreading of the wave packet, see Eq. (202), as a function of time t (taken from [26]). For $E_0 = 2$ (red curves) and $E_0 = 4$ (blue curves), the plot shows $\log_{10}\sigma(t)$ for $g = 0$ (dots) and $g = 1$ (continuos lines). The values of $\log_{10}\sigma(t)$ are averaged over 8 disorder realizations.

Fig. (22) shows analogous results for $E_0 = 4$ and $g = 1, 0.1, 0.03$ and 0 (blue, red, green curves and black dots respectively). In the linear case $g = 0$ (black curve), and also for the smallest value $g = 0.03$ of the nonlinearity (curve), the suppression of transport due to Anderson localization manifests itself in the saturation of the value of $\log_{10}\sigma(t)$ at $\log_{10} t \approx 3$. Starting from $g = 0.1$ there is a slow increase of σ with time, and a faster increase at $g = 1$. Evidently, no saturation of $\sigma(t)$ at $g = 1$ is observed. These results suggest that there is a certain critical value of the nonlinearity (for the parameters in the Fig. (22) the critical g value is around 0.1), above which the nonlinearity leads to a destruction of Anderson localization. In a later work [89], however, it was found that, also for small values of g, a subdiffusive spreading will eventually be observed at very long times, i. e., even longer than the ones plotted in Fig. (22). Physically, the destruction of Anderson localization due to nonlinearity is associated with the appearance of chaos caused by the nonlinear term in the equation of motion [89].

The main difference of the discrete Anderson model used in Eq. (201) with respect to our scenario of wave packet dynamics in a continous random potential can be summarized by the different dispersion relations: $E_k = 2V\cos(ka)$ (with lattice spacing a) for the lattice, whereas $E_k = k^2$ for the continous system (in the absence of disorder and nonlinearity). In particular, the kinetic energy is bounded from above in the lattice, whereas no such bound exists in the continuous system. A similar conclusion applies to the localization length in the presence of disorder (bounded in the lattice, but not in the continuum case). Since, however,

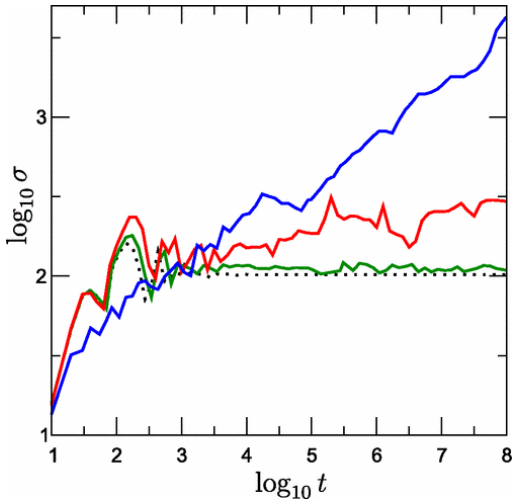

Fig. (22) (Taken from [26]) Dependence of the spreading σ on time t for $E_0 = 4$ and for different values of the nonlinearity strength $g = 1, 0.1, 0.03$ and 0 (blue, red, green solid lines and black dots, respectively). The simulations were performed only for a one disorder realization.

in the continous case, the energy range is also restricted to a certain extent by the choice of the initial state, we do not expect that these differences fundamentally affect the mechanism of sub-diffusive spreading discussed above. Nevertheless, we will not pursue this question further in this thesis, for the following two reasons: First, from a numerical point of view, it is difficult to propagate the Gross-Pitaevskii equation for sufficiently long times, where the subdiffusive spreading is expected to become relevant. Second, as discussed above, the description of the many-particle quantum system in terms of the Gross-Pitaevskii equation looses its validity in the regime of long times.

8.3 INTERMEDIATE TIMES: QUASI-STATIONARY STATE

In the following, we will hence restrict ourselves to times which are, on the one hand, longer than the time needed to reach the stationay state in the linear case, but, on the other hand, shorter than the time scale of the sub-diffusive spreading mentioned above. As we will verify by numerical simulation in Chapter 9, the density profile of the condensate for such intermediate times assumes a quasi-stationary state which is almost constant as a function of time.

Two stages of expansion

In order to describe the influence of the nonlinearity on this quasi-stationary density profile, we will use an idea proposed in [27], [28],

according to which the expansion of the condensate can be split into two stages:

i) In the first stage, the expansion of the condensate is driven by the repulsive (for $g > 0$) interactions between the particles. During this time, the disorder potential is neglected.

ii) At a certain time t_i (which will be discussed below), almost all of the interaction energy is converted into kinetic energy. After that time, the dynamics of the condensate is described by the linear Schrödinger equation of the disordered potential.

The evolution during stage *ii)* can be treated by the techniques which we developed in Chapters 3-7. The role of the interactions in stage *i)* is to modify the form of the initial state assumed at the beginning of stage *ii)*. The calculation of this initial state requires the solution of the Gross-Pitaevskii equation in the absence of disorder.

Inverted parabola as an initial state

As an example, we first discuss the scenario treated in [28]. The time evolution of the condensate wave function is determined by the following Gross-Pitaevskii equation:

$$i\partial_t\psi(x) = \left(p^2 + V_{ho}(x) + V(x) + g|\psi|^2 - \mu\right)\psi(x), \tag{203}$$

where p^2 is the kinetic term, $V_{ho}(x) = \omega^2 x^2/4$ is the trapping potential, $V(x)$ is the disordered potential, g is the coupling parameter or interaction term and μ is the chemical potential. The wave function is normalized to the total number of atoms ($\int \mathrm{d}x\, |\psi|^2 = N$). The dynamics is governed by Eq. (203) in the weakly interacting regime, i. e., $g/2 \ll n$, where n is the 1D density of atoms.

An interacting BEC is first produced in the harmonic trap $V_{ho}(x)$, and in the absence of disorder. Assuming the Tomas-Fermi regime, i. e. $n \gg \omega/g$, the phase of the wavefunction in Eq. (203) is uniform and the BEC density at time $t = 0$ is a truncated inverted parabola:

$$n_0(x) = |\psi(x)|^2 = \left(\frac{\mu}{g}\right)\left[1 - \left(\frac{x}{L_{\mathrm{TF}}}\right)^2\right]_{\oplus}, \tag{204}$$

where $L_{\mathrm{TF}} = \sqrt{4\mu/\omega^2}$ and $[f(x)]_{\oplus} = f(x)$ for $f(x) > 0$ and 0 otherwise (see also Subs. 3.1.2.)

At time $t = 0$, the trapping potential $V_{ho}(x)$ is switched off. The expansion stage *i)* is driven by the interactions, still in absence of the

disorder potential. Due to the fact that the initial state is given as a stationary solution of Eq. (203) in the presence of a harmonic trapping potential, the evolution of the condensate at later times (without the trapping potential) can be obtained by using the scaling approach [90], [91], according to which the expanding BEC acquires a dynamical phase and the wave function is rescaled as

$$\psi(x,t) = \frac{\psi(x/b(t),0)}{\sqrt{b(t)}} \exp\left(\frac{ix^2\dot{b}(t)}{4b(t)}\right), \tag{205}$$

where the scaling parameter $b(t)$ fulfills $b(0) = 1$ and $b(t) \approx \sqrt{2}\omega t$ for $t \gg 1/\omega$ [30].

For the second expansion stage ($t > t_i$) the disordered potential is suddenly switched on and the interactions off. The disorder-averaged asymptotic density profile is described by Eq. (9), where the Wigner function of the initial state is extracted from Eq. (205) at time t_i. For $t_i \gg 1/\omega$, the Wigner function is given by:

$$W_i(q,p) \approx D_i(p)\delta\left(q - \frac{2b(t_i)}{\dot{b}(t_i)}\right). \tag{206}$$

where $D_i(p) = (3N/4p_m(t_i))[1-(p/p_m(t_i))^2]_{\oplus}$ is the momentum distribution, with $p_m(t_i) = (1/\xi)[\dot{b}(t_i)/\sqrt{2}\omega]$ and $\xi = 1/\sqrt{2\mu}$ [28].

8.4 EFFECTIVE GAUSSIAN INITIAL STATE

As discussed in Subs. 3.1.2, we consider in the present thesis a Gaussian state $\psi_0(x)$ as initial state at time $t = 0$, see Eq. (19). According to the expansion stage *i)* described above, we first have to solve the Gross-Pitaevskii equation for this initial state in the absence of disorder. Since the Gaussian state is not a stationary solution of the Gross-Pitaevskii equation for a harmonic trapping potential, the scaling approach [90], [91] cannot be applied to obtain the required solution.

Instead, we obtain an approximate analytical solution by assuming that the wave function remains Gaussian at all times during the first expansion stage. Furthermore, we use the property of energy conservation discussed in Sec. 8.1 above. In the absence of disorder during stage *i)*, the Gross-Pitaevskii energy functional with respect to a Gaussian state with width a, see Eq. (19), reads:

$$E[\psi_0] = \frac{1}{2a^2} + \frac{g}{a\sqrt{\pi}}, \tag{207}$$

where $1/(2a^2)$ gives the average kinetic energy, whereas $g/(a\sqrt{\pi})$ is associated with the interaction energy. During the expansion stage *i)*,

the interaction energy is converted into kinetic energy, but the sum of both remains conserved, see Eq. (198b).

Our idea is now to approximate the solution of the Gross-Pitaevskii equation by the solution of the *linear* Schrödinger equation, using as initial state a Gaussian state with width a_{eff} given by:

$$\frac{1}{2a_{eff}^2} = \frac{1}{2a^2} + \frac{g}{a\sqrt{\pi}}, \tag{208}$$

The *effective Gaussian initial state* is given by Eq. (19) with a replaced by a_{eff}.

The Fourier transform of the Gaussian effective initial state is:

$$\tilde{\psi}_0^{eff}(k) = \sqrt{\sqrt{\frac{a_{eff}^2}{2\pi}}}\, e^{-a_{eff}^2 k^2/4}. \tag{209}$$

Therefore, its temporal evolution is [92]:

$$\begin{aligned}
\psi^{eff}(x,t) &= \int_{-\infty}^{\infty} \mathrm{d}k\ \tilde{\psi}_0^{eff}(k) \exp\{i(kx - k^2 t)\}, \\
&= \sqrt{\sqrt{\frac{a_{eff}^2}{2\pi}}} \int_{-\infty}^{\infty} \mathrm{d}k\ \exp\{-a_{eff}^2 k^2/4 + i(kx - k^2 t)\}, \\
&= \sqrt{\sqrt{\frac{2a_{eff}^2}{\pi}}}\, \frac{\exp\{-x^2/(a_{eff}^2 + 4it)\}}{\sqrt{a_{eff}^2 + 4it}},
\end{aligned} \tag{210}$$

with probability distribution:

$$|\psi^{eff}(x,t)|^2 = \sqrt{\frac{2}{\pi}}\, \frac{a_{eff}\ \exp\{-2a_{eff}^2 x^2/(a_{eff}^4 + 16t^2)\}}{\sqrt{a_{eff}^4 + 16t^2}}. \tag{211}$$

In the next chapter, see Sec. 9.3, we will find numerically the evolution of an initial Gaussian wave packet described by the Gross-Pitaevski equation and compare it with Eqs. (209-211).

8.5 ENERGY PROBABILITY DISTRIBUTION $P_g(E)$

To close this chapter, the energy distribution $P_g(E)$ of our effective Gaussian initial state is again extracted from the spectral function according to Sec. 6.3. This time, we use the Wigner function $W(q,p)$ of the effective Gaussian initial state, i. e., we replace a by a_{eff} in Eq. (19),

where a_{eff} fulfils Eq. (208). Like in Sec. 6.3, the integral over q and p can be performed analytically:

$$P_g(E) = \frac{a_{eff}}{\sqrt{\pi}} \Im \left\{ \frac{e^{(a_{eff})^2 \left(\Sigma^{(+)}(E) - E\right)} \operatorname{erfc}\left(a_{eff}\sqrt{\Sigma^{(+)}(E) - E}\right)}{\sqrt{\Sigma^{(+)}(E) - E}} \right\}, \tag{212}$$

with complementary error function $\operatorname{erfc}(z)$. We have checked again that this expression, with $\Sigma^{(+)}(E)$ given by Eq. (185), yields a normalized distribution [25], i. e., $\int_{-\infty}^{\infty} \mathrm{d}E \; P_g(E) = 1$, which underlines the consistency of our approach.

Fig. (23) shows the energy probability distribution for different interaction parameters $g = 0,\ 0.25,\ 0.75,\ 1.25,\ 1.75$ and 2.0 (in units of σ_c^{-1}). The value of the disordered potential is $V_0 = 0.0325\ \sigma_c^{-2}$ and the width of the initial state is given by a^{eff}, Eq. (208), where $a = \sqrt{2}\sigma_c$. The function $P_g(E)$, given by Eq. (212), is plotted with continuos lines, while, for comparison, the symbols represent the energy probability distribution for the free particle. The black lines and symbols are related to $g = 0$, and the light blue ones with $g = 2.0$. As already discussed in Chapter 2, the wave packet can be represented as a superposition of energy eigenstates, where the eigenstates associated to the smaller energy modes are confined classically in deep quantum wells for each realization of the disordered potential. On the other hand, states with higher values of the energy are subject to Anderson localization due to destructive interference after multiple reflections. As the strength g of interactions increases, $P_g(E)$ decreases in the regime of small energies (see Fig. (23a)), but, in order to ensure its normalization, it must increase (as a function of g) for large energies (see Fig. (23b)). In the next chapter, we will investigate how this dependence of the energy distribution on g affects the density profile of the quasi-stationary state, and we will verify the validity of our Gaussian effective state ansatz by comparison with numerical data.

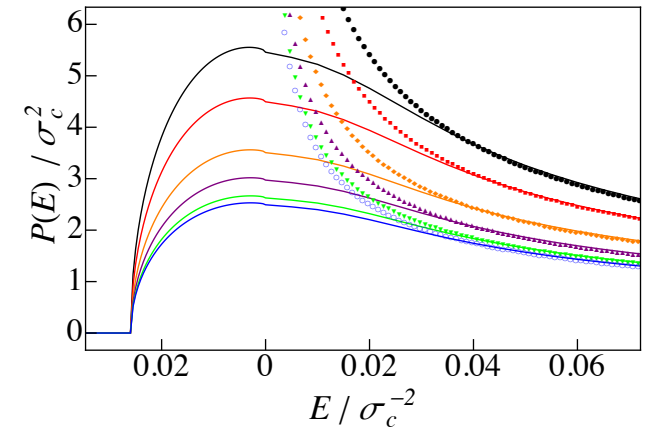

(a)

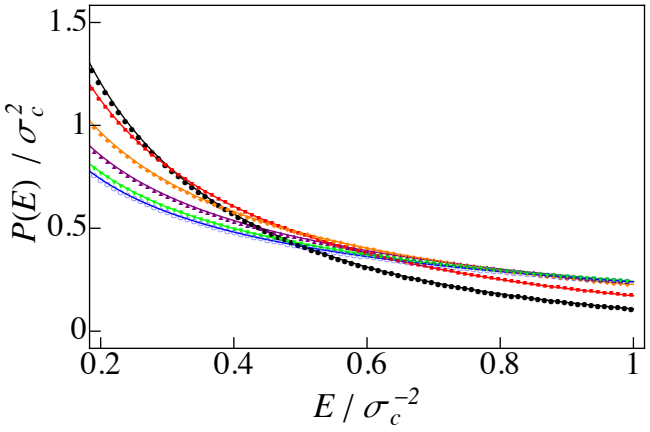

(b)

Fig. (23) Energy probability distribution $P_g(E)$ (in units of σ_c^2), for different interaction parameters $g = 0,\ 0.25,\ 0.75,\ 1.25,\ 1.75$ and 2.0 (in units of σ_c^{-1}), as a function of the energy (in units of σ_c^{-2}). The value of the disordered potential is $V_0 = 0.0325\ \sigma_c^{-2}$ and the width of the Gaussian effective initial state is given by a^{eff}, Eq. (208), with $a = \sqrt{2}\sigma_c$. $P_g(E)$ is plotted with continuos line curves. For comparison, the energy probability distribution for a free particle is marked by symbols. The black curve and symbols are related to $g = 0$ and the light blue ones to $g = 2.0$. Fig. (23a) shows the range of small energies, while Fig. (23a) refers to the large energy range.

9

NUMERICAL RESULTS WITH INTERACTIONS

In this chapter, we present the numerical results for the quasi-stationary density profile, $\overline{n_g(x)}$, of an interacting BEC in a one-dimensional disordered potential. After a short description of the numerical algorithms used for this purpose in Sec. 9.1, we first test in Sec. 9.2 the basic hypothesis put forward in the previous chapter: that there exists a regime of intermediate times, where the density profile assumes an almost constant, i. e. quasi-stationary state. As explained in Sec. 8.2, we expect that, at extremely long times after this intermediate regime, the density exhibits subdiffusive spreading. In the present thesis, however, we do not consider sufficiently long times in order to observe this effect, and restrict ourselves to the quasi-stationary regime. For the theoretical description of this quasi-stationary regime, we assume that the interactions can be neglected at large times, where, due to the spatial expansion, the density of the condensate has dropped to very small values. We test this assumption numerically by setting the interaction strength g to zero after a certain time t_i, and verifying that the resulting stationary density profile well agrees with the quasi-stationary one obtained for constant g.

In Chapter 8, we furthermore proposed that the quasi-stationary state can be described in the framework of the linear theory developed in Chapters 3-7, provided that the energy distribution associated to the initial state is suitably modified in order to account for the interaction energy. More precisely, our claim is that the solution of the nonlinear Gross-Pitaevskii equation with a Gaussian state as initial state resembles the solution of the linear Schrödinger equation with a different Gaussian state as initial state, the width of which is determined such that the expectation value of the energy is the same in both cases. In Sec. 9.3, we will test the validity of this ansatz in the absence of the disorder potential. First, we study, by numerically solving the Gross-Pitaevskii equation, how the interaction energy is progressively converted into kinetic energy, until it becomes negligibly small at time t_i. Then, we compare the linear time evolution of the wave function predicted by our Gaussian effective initial state ansatz with the solution of the Gross-Pitaevskii equation, both in position and in momentum space.

In Sec. 9.4, we finally compare the numerically obtained quasi stationary density profiles in the presence of the disorder potential with our theoretical prediction.

9.1 NUMERICAL ALGORITHMS FOR SOLVING THE GROSS-PITAEVSKII EQUATION

In this chapter, we use two different algorithms for calculating solutions of the nonlinear Gross-Pitaevskii equation Eq. (203): a fast and simple one that can be used at short times, and a more accurate one valid also at longer times.

The first one is the *Fourier propagation* scheme. It uses the fact that the kinetic energy is diagonal in momentum space, whereas the potential energy and the interaction energy are diagonal in position space (see Appendix C for more details). We divide our system of length $L = 800\sigma_c$ into 2^{15} small elements of length $dx = 0.024\sigma_c$ (i. e. much smaller than the correlation length σ_c). In the momentum representation, the small elements are $dk = 2\pi/L = 0.0079\ 1/\sigma_c$. The time propagation is discretized into small steps of length $\Delta t = 0.001\sigma_c^2$. The advantage of the Fourier propagation scheme is that it is very fast. However, for long times (of the order of $1500\sigma_c^2$), it becomes inaccurate, as evident from the fact that its solutions start to violate the conditions of norm and energy conservation, see Sec. 8.1.

For longer times, we therefore use *the second order differential scheme* (SOD), which turns out to be more accurate. In particular, the conservation of norm and energy are well fulfilled up to the largest time $T_{max} = 10000\sigma_c^2$ that we consider in this thesis. For this scheme, we use the finite-element discrete variable representation (FEDVR) already explained in Sec. 7.2: the system of length $L = 800\sigma_c$ is divided into 10^4 finite elements of size $0.08\sigma_c$ (i. e. much smaller than σ_c). Each element, in turn, is discretized using 4 basis functions. In this basis of dimension $M = 4 \times 10^4$, the Gross-Pitaevskii equation Eq. (203) is solved using a propagation scheme which is accurate up to second order in $\Delta t = 0.001\sigma_c^2$, see Appendix C for more details.

9.2 TIME-DEPENDENT EXPANSION OF THE WAVE PACKET

In Fig. (24), we show, for $a = \sqrt{2}\sigma_c$ and $V_0 = 0.0325\sigma_c^{-2}$, the time evolution of the spatial density profile without interactions, i. e., $g = 0$. To propagate the initial state Eq. (19) until times as long as $T_{max} = 10000\sigma_c^2$, we used the SOD algorithm (see the above section). The main figure in Fig. (24) shows the spatial density profile for $t = 0$ (black), $200\sigma_c^2$ (blue), $400\sigma_c^2$ (green), $600\sigma_c^2$ (orange), $800\sigma_c^2$ (purple), $1000\sigma_c^2$ (red) and $10000\sigma_c^2$ (cyan). The left inset in Fig. (24) shows the first four times, i. e., $t = 0$ (black), $200\sigma_c^2$ (blue), $400\sigma_c^2$ (green), $600\sigma_c^2$ (orange), while the right inset shows the last three times, i. e., $800\sigma_c^2$ (purple), $1000\sigma_c^2$ (red) and $10000\sigma_c^2$ (cyan). We average over 2000 samples. In the main figure and the right

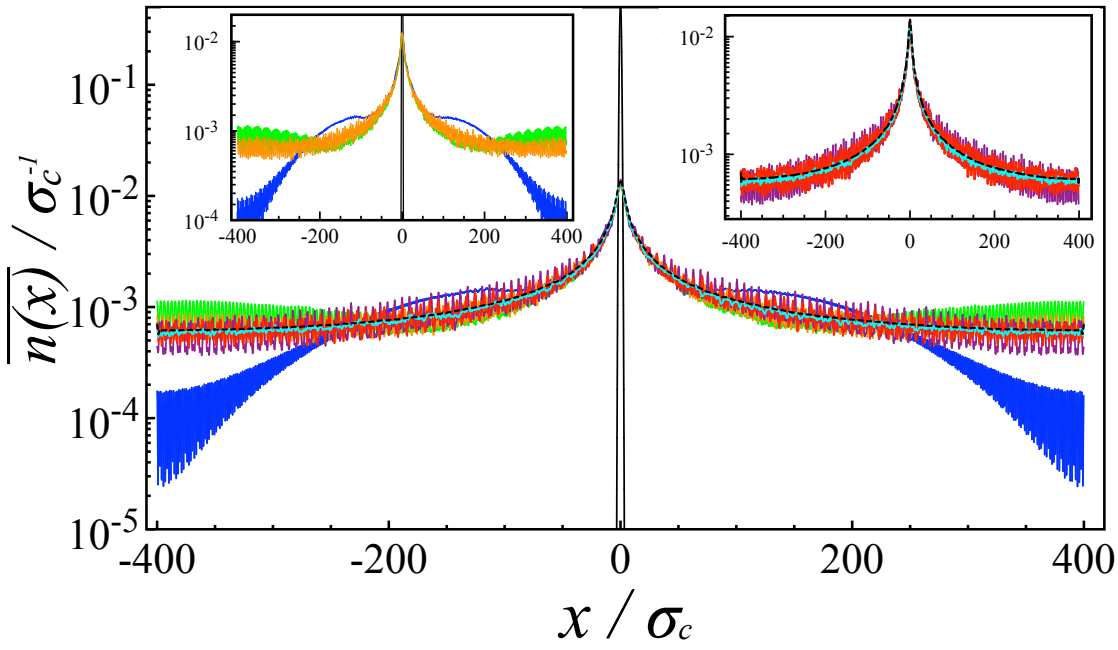

Fig. (24) Numerically obtained time dependent density profiles (in units of σ_c^{-1}) as function of position (in units of σ_c) for interaction strength $g = 0$. We perform an ensemble-averaging over 2000 realization of the random potential. The remaining parameters are: $a = \sqrt{2}\,\sigma_c$ and $V_0 = 0.0325\,\sigma_c^{-2}$. The times are t: 0 (black), $200\sigma_c^2$ (blue), $400\sigma_c^2$ (green), $600\sigma_c^2$ (orange), $800\sigma_c^2$ (purple), $1000\sigma_c^2$ (red) and $10000\sigma_c^2$ (cyan). The left inset shows the first four times, and the right inset the last three times. In the main figure and the right inset, the black dashed line is related with the stationary average spatial density profile.

inset, the black dashed line is related with the stationary average spatial density profile, which was obtained using the definition given by Eq. (21), where we performed the numeric integral between the times $T_1 = 5000\sigma_c^2$ and $T_2 = 10000\sigma_c^2$,

$$n(x) = \frac{1}{T_2 - T_1}\int_{T_1}^{T_2} \mathrm{d}t\; n(x,t). \tag{213}$$

We can see how the non-interacting spatial density profile for longer times tends to the stationary average spatial density profile. The stationary profile is reached at about $t \approx 600\sigma_c^2$ (orange curve).

In Fig. (25), we show the same plot as in Fig. (24), but now in the presence of interactions ($g = 2\sigma_c^{-1}$). Again, we see that a quasi-stationary density profile is reached, at about the time $t \approx 400\sigma_c^{-1}$.

Finally, Fig. (26) shows that the influence of interactions is indeed negligible in the regime of intermediate times where, as we have seen above, the density profile is quasi-stationary. To show this, we evaluate

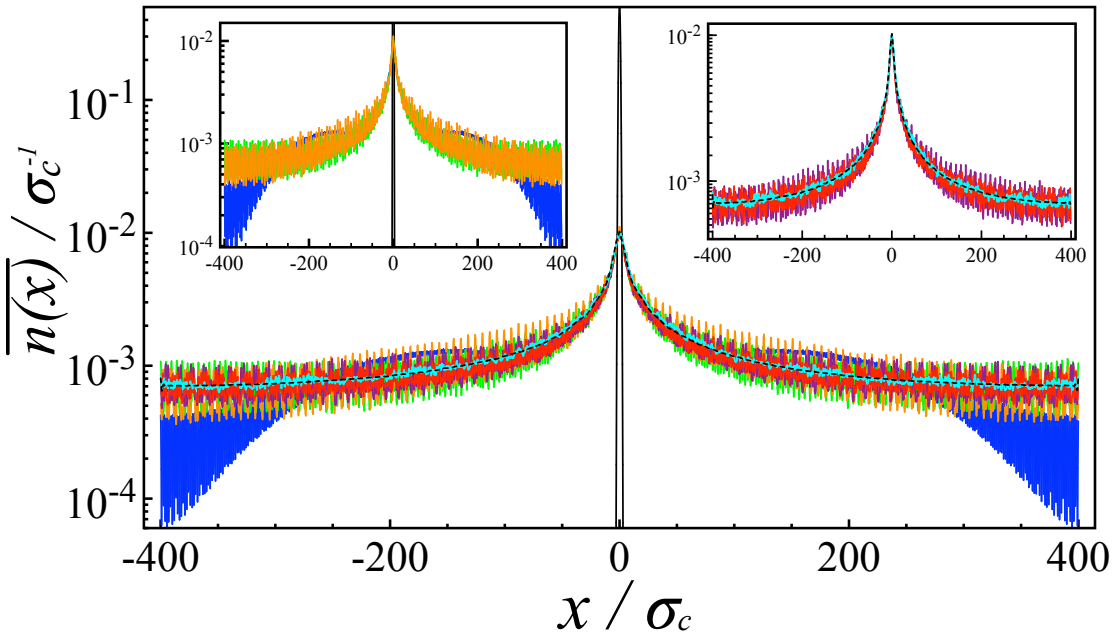

Fig. (25) Numerically obtained time dependent density profiles (in units of σ_c^{-1}) as function of position (in units of σ_c) for interaction strength $g = 2\sigma_c^{-1}$. The times are t: 0 (black), $200\sigma_c^2$ (blue), $400\sigma_c^2$ (green), $600\sigma_c^2$ (orange), $800\sigma_c^2$ (purple), $1000\sigma_c^2$ (red) and $10000\sigma_c^2$ (cyan). The left inset shows the first four times, and the right inset the last three times. In the main figure and the right inset, the black dashed line is related with the quasi-stationary average spatial density profile, which is evaluated by time-averaging $n(x,t)$ between $T_1 = 5000\sigma_c^2$ and $T_2 = 10000\sigma_c^2$, see Eq. (213), and aditionally ensemble-averaging over 2000 realization of the random potential.

the time-average density profile according to Eq. (213) with $T_1 = 5000\sigma_c^2$ and $T_2 = 10000\sigma_c^2$ for two different scenarios: one where the interaction is switched on all the time (black line), and one where we set the interaction to zero for times $t > 10\sigma_c^2$ (red line). We observe very good agreement between these two scenarios.

9.3 VALIDITY OF THE EFFECTIVE GAUSSIAN INITIAL STATE ANSATZ

In this section, we test the validity of our effective Gaussian initial state ansatz in the absence of the disorder potential. Remember that this ansatz involves two assumptions: first, that the solution of the Gross-Pitaevskii equation resembles the solution of the Schrödinger equation with a different initial state, and, second, that this different initial state is also a Gaussian state.

Before that, it is useful to examine the time scale on which the interaction energy is converted into kinetic energy when following the

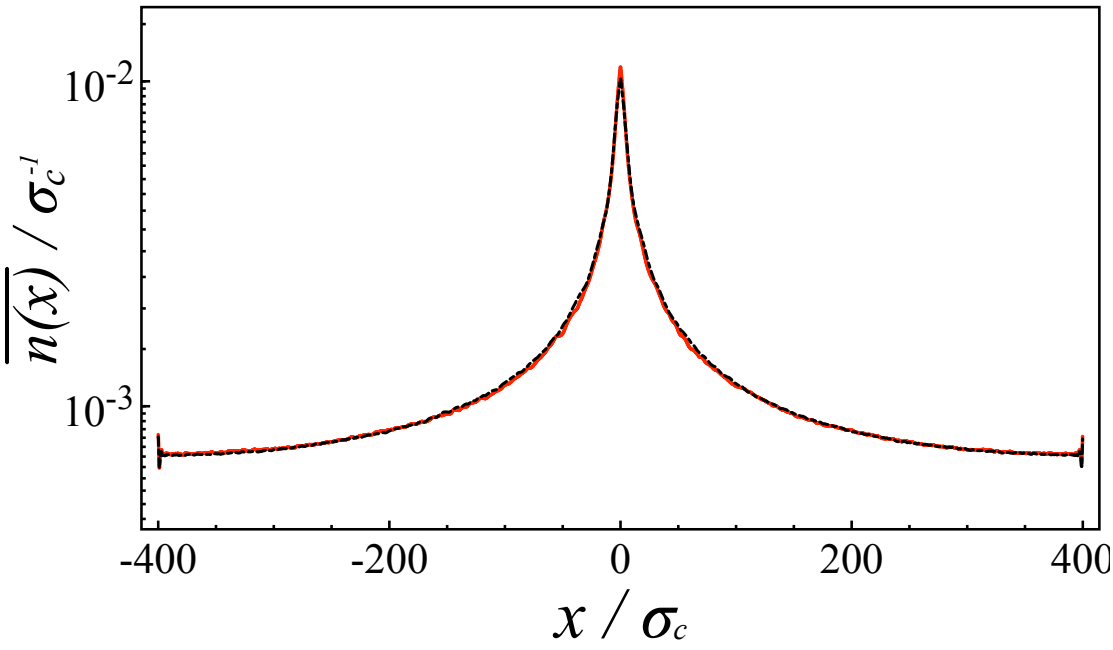

Fig. (26) Numerically obtained average quasi-stationary density profiles (in units of σ_c^{-1}) as function of position (in units of σ_c) for interaction strength $g = 2\sigma_c^{-1}$. The same values of a and V_0 as Fig. (24). The quasi-stationary state is evaluated by time-averaging $n(x,t)$ between $T_1 = 5000\sigma_c^2$ and $T_2 = 10000\sigma_c^2$, see Eq. (213), and additionally ensemble-averaging over 2000 realization of the random potential. The black dashed line is related with a scenario where the interactions are present in all time of the wave packet evolution, while the red line is related with a scenario where we switched off the interactions at $t_i = 10\sigma_c^2$. Good agreement is observed, which proves that, the interactions can indeed be neglected for $t > t_i$ (and $t < T_2$).

Gross-Pitaevskii equation. For this purpose, we study the expectation values of the kinetic energy and of the interaction energy.

$$\langle E_{kin}(t)\rangle = \int_0^L \mathrm{d}x\ \psi(x,t)\big(-\partial_x^2\big)\psi^*(x,t) \tag{214a}$$

and

$$\langle E_{int}(t)\rangle = \int_0^L \mathrm{d}x\ \frac{g}{2}|\psi(x,t)|^4, \tag{214b}$$

in the absence of disorder. The sum of both values gives the Gross-Pitaevskii energy functional, i. e.

$$\langle E_{kin}(t)\rangle + \langle E_{int}(t)\rangle = E[\psi(t)] = \text{constant}, \tag{215}$$

which is conserved, see Sec. 8.1. Fig. (27) shows these values, which monotonously increase (kinetic energy) or decrease (interaction energy),

respectively, as a function of time, for different values of g: $0.75\sigma_c^{-1}$ in Fig. (27a) and $1.25\sigma_c^{-1}$ in Fig. (27b). The dots are obtained with the Fourier propagation technique, and the lines with the SOD technique. The fact that they agree very well with each other underlines the accuracy of both approaches. At time $t_i = 10\sigma_c^2$, almost all of the interaction energy has been converted into kinetic energy. This explains why the effect of interactions becomes negligible at larger times, see also Sec. 9.2. Correspondingly, we observe only a very small difference if g is set to zero at time t_i in the SOD curve (red lines), whereas the Fourier propagation continues with constant g.

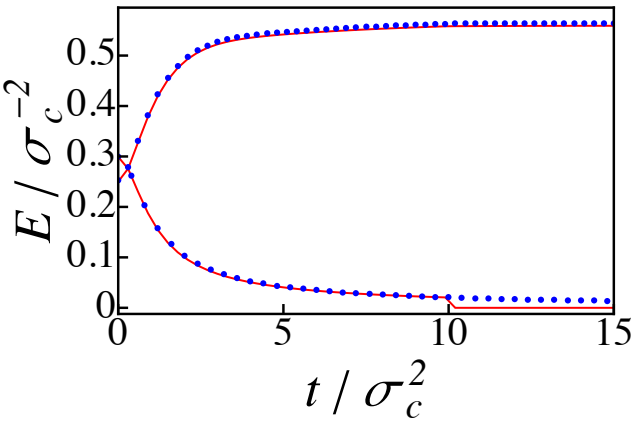

(a)

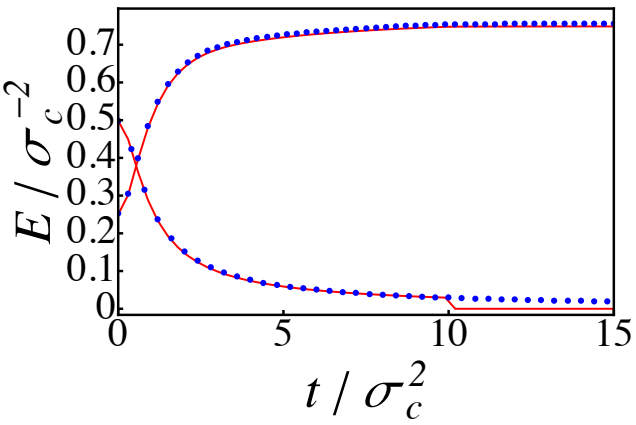

(b)

Fig. (27) Expectation values of the kinetic (upper curve) and the interaction (lower curve) energy (in units of σ_c^{-2}) for the Hamiltonian in Eq. (203) (without potential $V(x)$) as a function of time (in units of σ_c^2). The dots and lines are related to the Fourier and SOD propagation scheme, respectively. The values of g are $0.75\sigma_c^{-1}$ (Fig. (27a)) and $1.25\sigma_c^{-1}$ (Fig. (27b)). At time, $t = 10\sigma_c^2$, the interaction term in the SOD scheme is suddenly turned off. The width of the initial state, see Eq. (19), is $a = \sqrt{2}\sigma_c$.

In Fig. (28), we show, for the same parameters as in Fig. (27), the time evolution of the spatial density profile. For times smaller than $t_i = 10\sigma_c^2$, again perfect agreement between the Fourier and SOD solutions is observed (as expected), see Figs. (28a) and (28c). For larger times, the interaction is again set to zero in the SOD scheme (but not in the Fourier scheme), and almost no difference between these two cases can be seen, see Figs. (28b) and (28d).

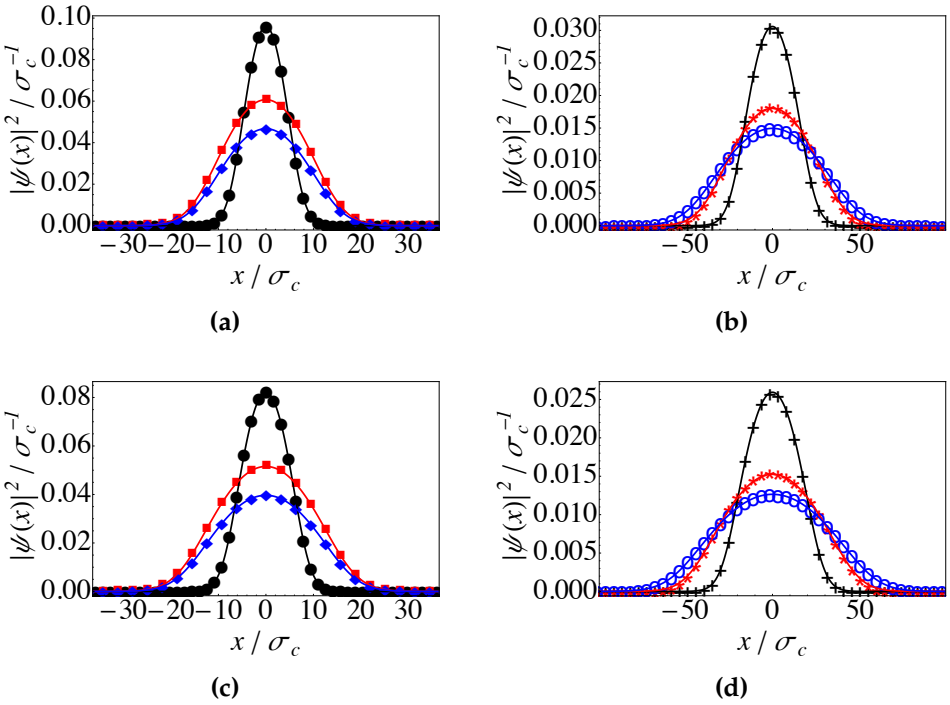

Fig. (28) Probability distributions $n(x,t) = |\psi(x,t)|^2$ (in units of σ_c^{-1}) as a function of position (in units of σ_c). The symbols (dots, squares, rhombuses, pluses, asterisks and circles) denote the solutions of the Gross-Pitaevskii equation obtained with the SOD (where the interaction is switched off at time $t_i = 10\sigma_c^2$), and the lines those obtained with the Fourier propagation scheme (where the interaction is present all the time). The plots in Figs. (28a) and (28b) are calculated for $g = 0.75\sigma_c^{-1}$ and in Figs. (28c) and (28d) are for $g = 1.25\sigma_c^{-1}$. The times are t: $4\sigma_c^2$ (dots), $6\sigma_c^2$ (squares), $8\sigma_c^2$ (rhombuses) in Figs. (28a) and (28c), and $12\sigma_c^2$ (pluses), $19\sigma_c^2$ (asterisks) and $23\sigma_c^2$ (circles) in Figs. (28b) and (28d). The width of the initial state, see Eq. (19), is $a = \sqrt{2}\sigma_c$. The disorder potential is switched off.

In Fig. (29), we compare the numerical results for the spatial density profile (lines obtained with the Fourier scheme, where g is switched on at all time) with our theoretical ansatz using the Gaussian effective initial state, i. e., Eq. (211) (symbols). This comparison is carried out at times $4\sigma_c^2$ (circles) and $23\sigma_c^2$ (squares), i. e., for the first ($0 < t \leqslant t_i$)

and second ($t > t_i$) stages respectively. Figs. (29a) and (29b) refer to $g = 0.75\sigma_c^{-1}$ and $1.25\sigma_c^{-1}$, respectively. In Fig. (29) we can see small deviations between our ansatz and the numerical results in the center of the distribution, while for long times these deviations are smaller. This behavior is expected, since, for long times, the interaction energy is transformed into kinetic energy, and we expect that the evolution of the Gaussian state, see Eq. (19), via Eq. (203) is similar to the evolution of a free particle, see Eq. (211).

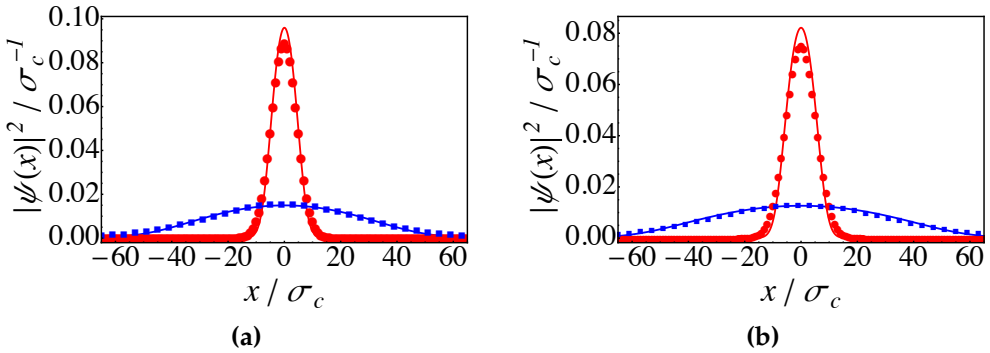

Fig. (29) Probability distributions $n(x,t) = |\psi(x,t)|^2$ (in units of σ_c^{-1}) as a function of position (in units of σ_c). Numerical results (lines obtained with the Fourier scheme, where g is switched on at all time) and theoretical ansatz (symbols) for times t: $4\sigma_c^2$ (circles) and $23\sigma_c^2$ (squares). The width of the initial initial state, Eq. (19), is $a = \sqrt{2}\sigma_c$. Figs. (29a) and (29b) refer to $g = 0.75\sigma_c^{-1}$ and $1.25\sigma_c^{-1}$, respectively. The disorder potential is switched off. The Gaussian effective state ansatz (symbols) agrees very well with the exact numerical result (lines), especially at larger times.

The Fourier technique allows us to obtain also the momentum probability distribution. Therefore, Fig. (30a) shows the numerical momentum distribution for three different times: $t = 4\sigma_c^2$ (red), $t = 12\sigma_c^2$ (blue) and $t = 200\sigma_c^2$ (black), and for $g = 0.75\sigma_c^{-1}$. The curve at $t = 200\sigma_c^2$ corresponds to a stationary state of the momentum distribution, since the interaction energy is indeed negligibly small at that time (which is more than twenty times longer than $t_i = 10\sigma_c^2$, see also Fig. (27)). (Remember that the disorder potential is still switched off!). Fig. (30b) shows the numerical results for this asymptotic momentum distribution and our Gaussian initial state ansatz given by the Eq. (209), which yields a strictly time-independent momentum distribution in the absence of disorder, for two different interaction parameters g: $0.75\sigma_c^{-1}$ (red) and $1.25\sigma_c^{-1}$ (blue). Again, we observe in Fig. (30b) very good agreement between the numerical calculation and our ansatz.

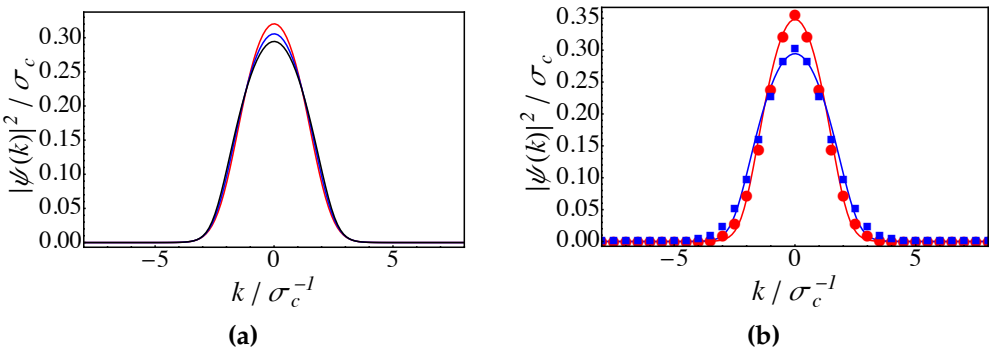

Fig. (30) (a) Numerical momentum distributions $|\psi(k,t)|^2$ for three different times: $t = 4\sigma_c^2$ (red), $t = 12\sigma_c^2$ (blue) and $t_i = 200\sigma_c^2$ (black), and for $g = 0.75\sigma_c^{-1}$. (b) Momentum probability distributions (in units of σ_c) for two different strengths of the interaction $g = 0.75\sigma_c^{-1}$ (red) and $g = 1.25\sigma_c^{-1}$ (blue). The numerically determined asymptotic long-time distribution ($t_i = 200\sigma_c^2$, red and blue lines) agree very well with our Gaussian initial state ansatz, see Eq. (209) (symbols). In (a) and (b), the lines are obtained with the Fourier scheme (where g is switched on at all time) and the width of the initial state, see Eq. (19), is $a = \sqrt{2}\sigma_c$.

9.4 QUASI-STATIONARY DENSITY PROFILE

After having established the accuracy of our Gaussian initial state ansatz in the absence of disorder, we now investigate the quasi-stationary state reached in presence of the disorder potential. According to our ansatz, this state is obtained by the same method that we employed in the linear case, see Sec. 7.1, where the width a of the initial state is replaced by the width a_{eff}, see Eq. (208), which, as discussed above, effectively takes into account the influence of the interactions at short times.

9.4.1 *Discussion of numerical results*

As already discussed in Secs. 9.1-9.2, the numerical quasi-stationary average density profile is obtained by solving the Gross-Pitaevskii equation, using the SOD algorithm, and then averaging the density $n(x,t)$ between $T_1 = 5000\sigma_c^2$ and $T_2 = 10000\sigma_c^2$, see Eq. (213).

Furthermore, we distinguish two different cases, where the disorder potential is switched off or not switched off during the initial propagation stage until time t_i. These two cases are compared to each other in Figs. (31)-(34), which show the results for the case where the interactions are switched off at time $t_i = 10\sigma_c^2$. As shown in Sec. 9.2, the same profile is obtained if the interactions are present all the time.

In every figure, the left inset plot exhibits the tails, while the right inset plot shows the center of the asymptotic average density profile. The continuous line, present in all the figures, is the asymptotic average density for $g = 0$. The width of the initial state, Eq. (19), is $a = \sqrt{2}\sigma_c$, the strength of the disordered potential $V_0 = 0.0325\sigma_c^{-2}$, and the average was performed for 2000 different disordered potential realizations. In every one of the left inset plots, we see that the numerical results for the two mentioned scenarios agree very well with each other. This is not suprising, since the tails of the profile are determined by large energies, for which the disorder potential has almost no effect at short times. On the contrary, the right inset plots show a small deviation between the numerical $\overline{n_g(x)}$ for the two different scenarios. This can be understood as follows: if the disorder is present already at time $t = 0$, the energy distribution is very sensitive to the values of the disorder potential at the initial position $x \simeq 0$ of the Gaussian wave packet. In particular, if the random potential happens to exhibit a deep minimum at $x = 0$, a large part of the wave function will be trapped in this minimum. If, on the other hand, the disorder is switched on only at time t_i, where the size of the wave packet is already much larger than the correlation length σ_c of the random potential, see Fig. (28), the fluctuations of the potential energy are much smaller, and it is less likely that the condensate is trapped in a minimum. This decreases the density at the center, as compared with the first case.

Furthermore, the numerical data exhibit interferences at $x \simeq L/2$ and $x \simeq -L/2$, which we already discussed in the linear case, see Fig. (19). Additionally, another small interference feature now arises in the center of the wave packet. In Fig. (31), it is hardly visible, but it becomes more pronounced at larger values of the interaction strength, see Figs. (31)-(34). The physical origin of this interference is the same as the one at $x \simeq L/2$ and $x \simeq -L/2$. As explained in Subs. 7.3.3, it is related to the finite size of the system in connection with periodic boundary conditions. In order to explicitly check this explanation, we performed simulations for different length of the disordered potential ($L = 600\sigma_c, 400\sigma_c, 200\sigma_c$ and $100\sigma_c$). Fig. (35) confirms that, indeed, these interferences become more pronounced for smaller system sizes.

Finally, Fig. (36) collects the data shown in Figs. (31)-(34) (with disorder potential switched on all the time) for different strength g of the interaction, such that the effect of changing g can be viewed in a single plot. Obviously, the density is reduced at the center (and, correspondingly, increased in the tails), as a consequence of stronger repulsive interactions.

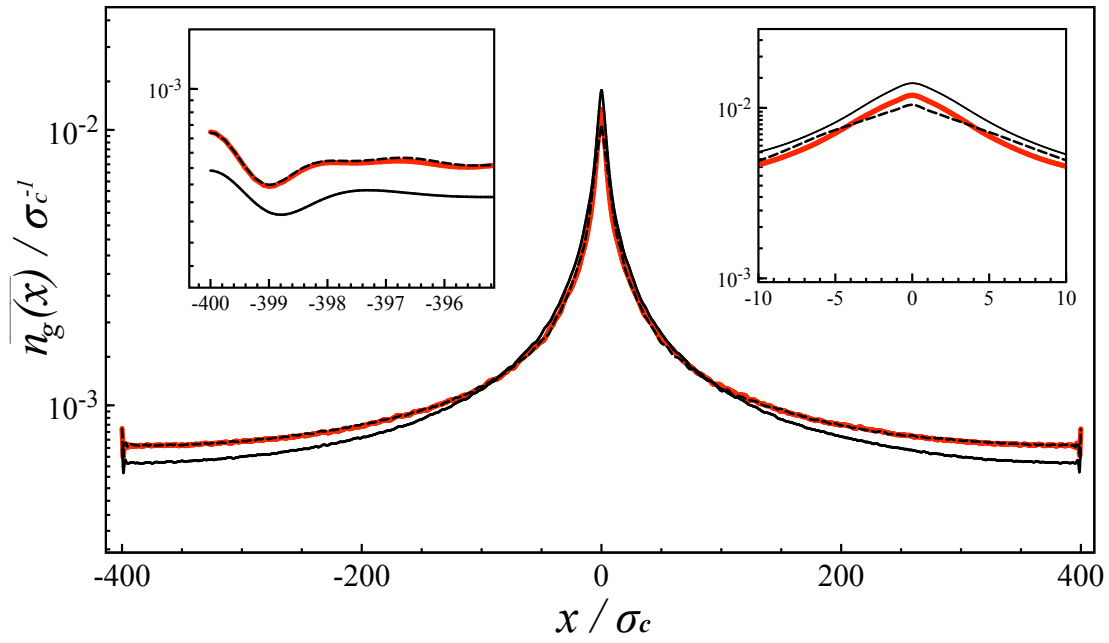

Fig. (31) Numerically obtained quasi-stationary density profiles (in units of σ_c^{-1}) as function of position (in units of σ_c) for interaction strength $g = 0.25\sigma_c^{-1}$. The dashed line refers to the scenario where the disordered potential is switched off during the first stage until time $t_i = 10\sigma_c^2$. The red line represents the other scenario, where the disorder potential is present all the time. The left inset shows the tail, and the right the center of the density profile. The black solid line is related with the case $g = 0$. The remaining parameters are: $a = \sqrt{2}\,\sigma_c$ and $V_0 = 0.0325\ \sigma_c^{-2}$. Average over 2000 disorder realizations.

9.4.2 *Comparison with theory*

We now compare the numerical results with our theoretical model. As already mentioned above, the theoretical description is the same already applied in the linear case, see Sec. 7.1, but with a different initial state, which effectively takes into account the influence of interactions.

Before presenting this comparison, let us first discuss the question to what extent the theoretical model takes into account the disorder at short times. As explained in Sec. 8.3, the effective initial state was determined under the assumption that the disorder can be neglected during the first stage of expansion. In particular, we showed in Sec. 9.3 that, in the absence of disorder, the linear evolution starting from the modified initial state closely resembles the nonlinear evolution starting from original initial state. Nevertheless, we stress that our modified initial state refers to a state at time $t = 0$, and that the linear theory summarized in Sec. 7.1 takes into account the presence of disorder *at all times*. Therefore, our theoretical ansatz should correspond to the second

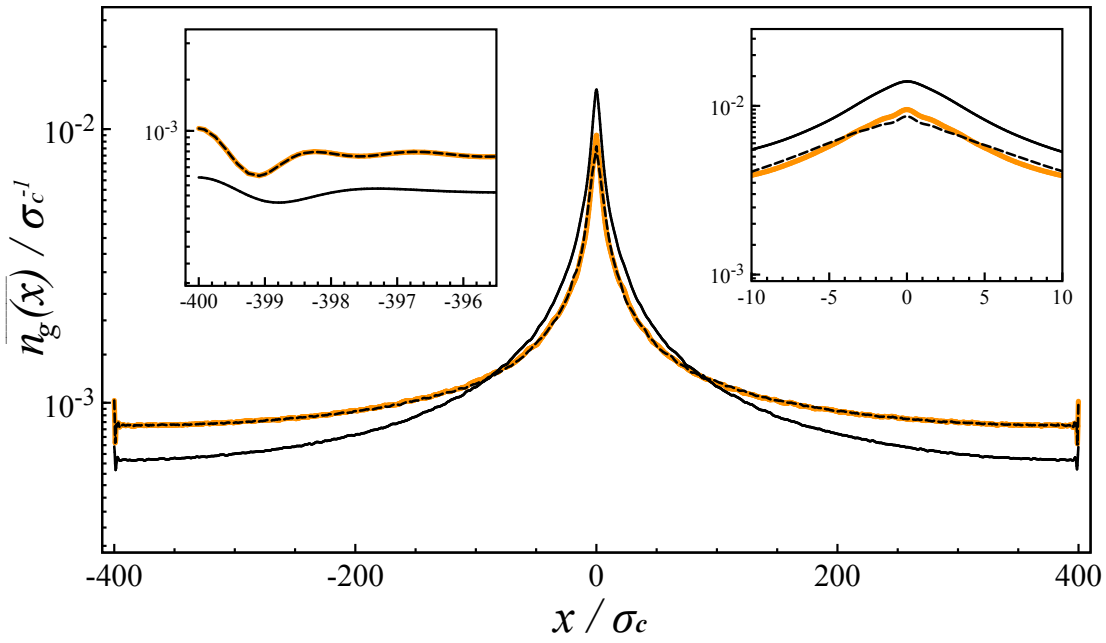

Fig. (32) Same as Fig. (31), for $g = 0.75\sigma_c^{-1}$.

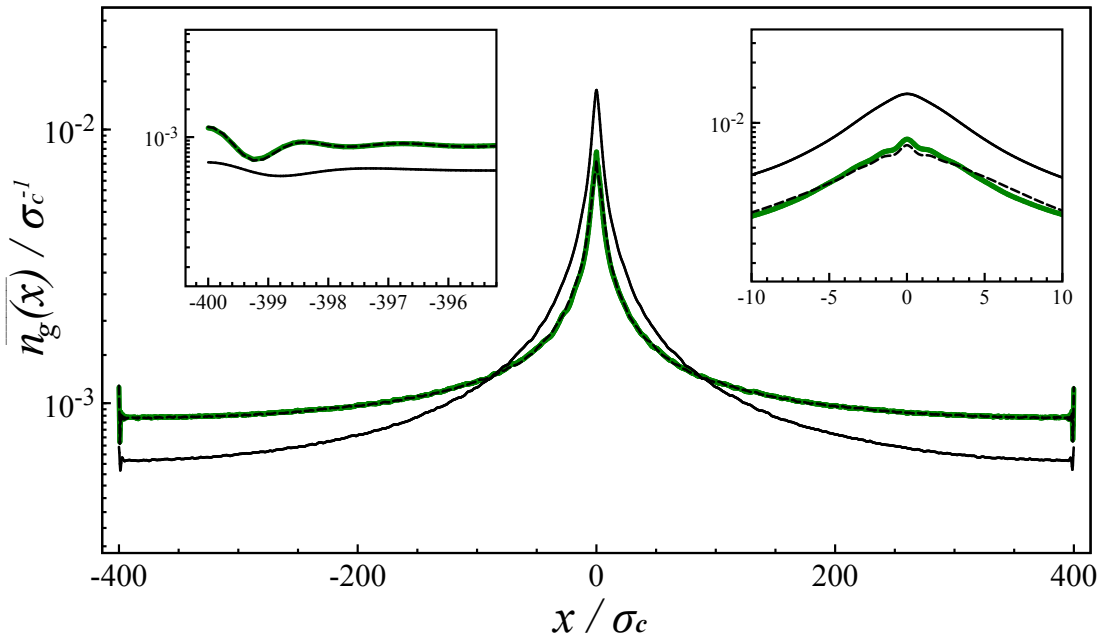

Fig. (33) Same as Fig. (31), for $g = 1.25\sigma_c^{-1}$.

scenario described above, where the disorder is present at all times. In order to describe the first scenario (disorder switched off until time t_i), we would have to take as initial state the effective state, see Eq. (210) at time $t = t_i$ instead of $t = 0$. In this case, however, the validity of Eq. (9) is questionable, since it was derived under the assumption of an initially strongly confined wave packet (see Chapter 4). We will therefore restrict

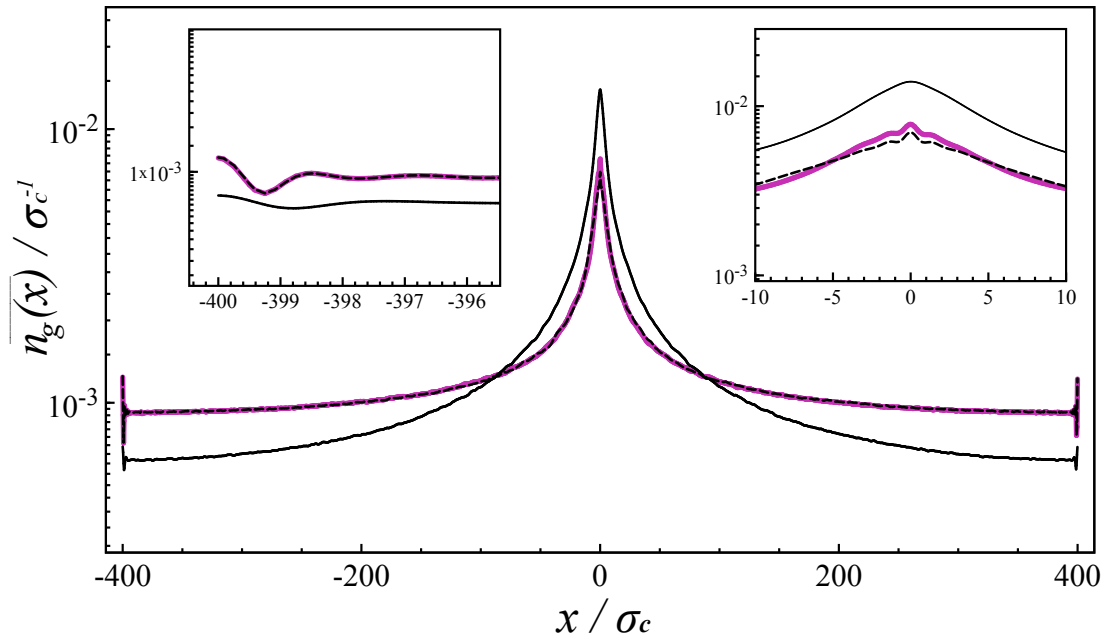

Fig. (34) Same as Fig. (31), for $g = 1.75\sigma_c^{-1}$.

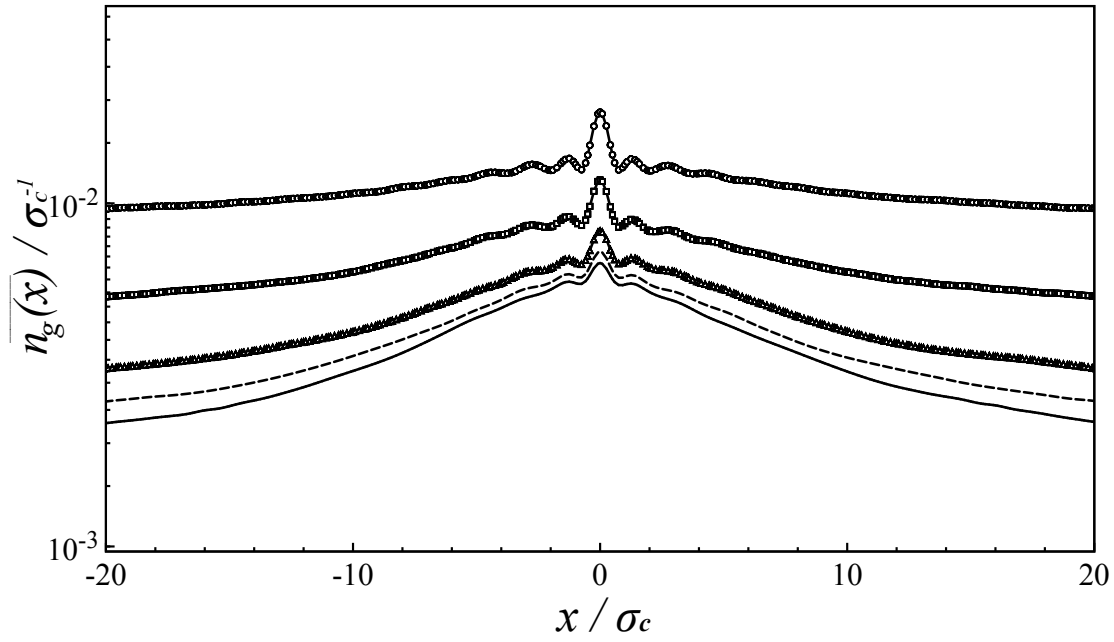

Fig. (35) Numerically obtained quasi-stationary density profiles (in units of σ_c^{-1}) as a function of position (in units of σ_c) for different system sizes L, $100\sigma_c$ (circles), $200\sigma_c$ (squares), $400\sigma_c$ (triangles), $600\sigma_c$ (dashed lines) and $800\sigma_c$ (continuos line), $g = 2\sigma_c^{-1}$, $a = \sqrt{2}\sigma_c$ and $V_0 = 0.0325\sigma_c^{-2}$. Average over 2000 realizations of the random potential. The oscillations in the center become more pronounced for smaller system sizes.

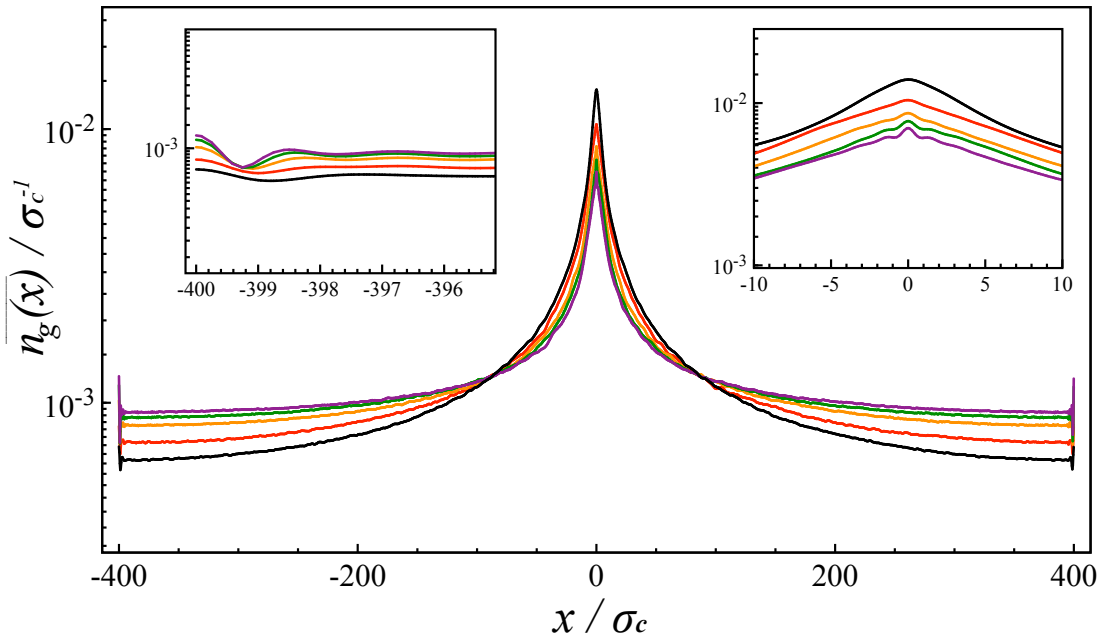

Fig. (36) Numerically obtained quasi-stationary density profiles (in units of σ_c^{-1}) as a function of position (in units of σ_c), for $g = 0$ (black), 0.25 (red), 0.75 (orange), 1.25 (green) and 1.75 (purple) (in units of σ_c^{-1}). The disorder potential is present all the time. This plot shows the same data as in Figs. (31)-(34) (dashed lines), such that the effect of varying the interaction strength can be viewed in a single plot. The density is reduced at the center (and, correspondingly, increased in the tails), as a consequence of stronger repulsive interactions.

ourselves to comparing our theory with the numerical scenario where the disorder is present all the time.

In Figs. (37) and (38), we see that our theory (dashed and dashed-dotted lines), given by Eq. (9), but using the expressions Eqs. (166) and (168) for the Lyapunov exponent, and the Eq. (212) for the spectral function, i. e., based on the effective Gaussian initial state, give us a good description of the numerical data (color), both, in the wings of the spatial profile and, remarkably, also close to the center of the wave packet (insets), for different g values (0 black, 0.25 red, 0.75 orange, 1.25 green and 1.75 purple. All in units of σ_c^{-1}). The scenario in our numerical calculus is the one already discussed in Sec. 8.3, which considers the disordered potential present for all the time.

As we already discussed, the oscillations close to $x = \pm L/2$ and, less pronounced, also close to $x \approx 0$, result from interferences due to the periodic boundary conditions, which are not included in our theoretical model.

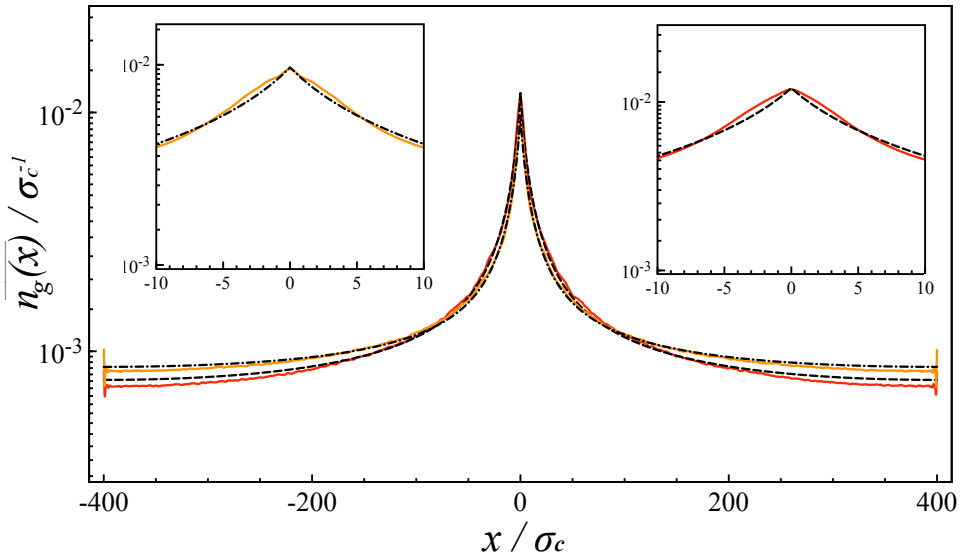

Fig. (37) Numerical quasistationary density profiles (in units of σ_c^{-1} and with the disorder potential present all the time) for interaction strength $g = 0.25\sigma_c^{-1}$ (red) and $0.75\sigma_c^{-1}$ (orange), in comparison with our theoretical description (black dashed lines for $g = 0.25\sigma_c^{-1}$, and dot-dashed lines for $g = 0.75\sigma_c^{-1}$.) Our theory is given by Eq. (9), using the expressions Eqs. (166) and (168) for the Lyapunov exponent, and Eq. (212) for the spectral function, i. e., based on the Gaussian effective initial state. Remaining parameters $a = \sqrt{2}\sigma_c$ and $V_0 = 0.0325\ \sigma_c^{-2}$. We observe good agreement between theory and numerics, both in the tails and in the center (see left and right inset for g: $0.25\sigma_c^{-1}$ and $0.75\sigma_c^{-1}$, respectively). Average over 2000 realizations of the random potential.

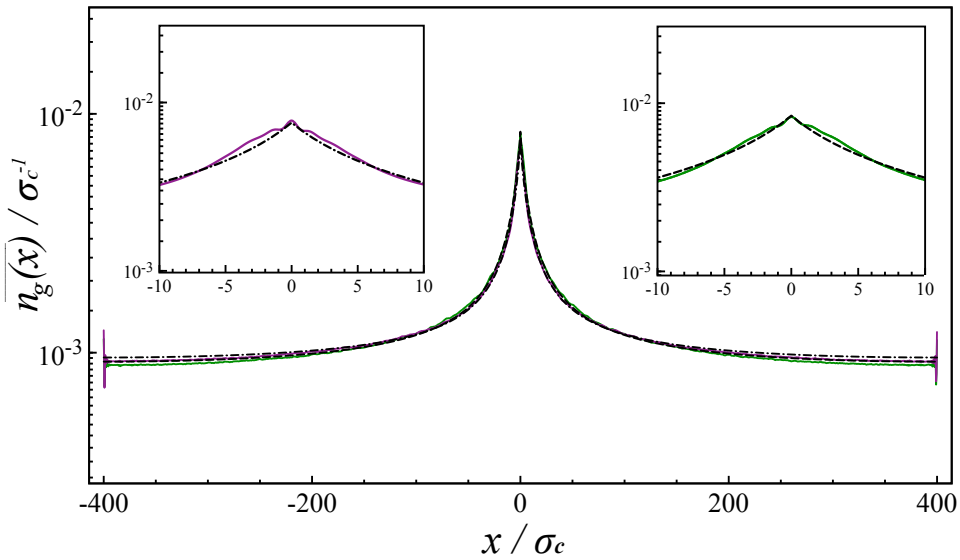

Fig. (38) Same as Fig. (37), for $g = 1.25\sigma_c^{-1}$ (green solid and black dashed lines) and $1.75\sigma_c^{-1}$ (purple solid and black dot-dashed lines).

10

SUMMARY & OUTLOOK

In the present chapter, we first present a summary of the results developed throughout this thesis in Sec. 10.1. After that, in Sec. 10.2, we discuss perspectives and futures goals of our work.

10.1 SUMMARY

The motivation of the present thesis originates from the need of obtaining an improved analytical description of the long-time localized density profile measured in experiments on Bose-Einstein condensates (BECs) in one-dimensional random potentials. In Chapter. 2, we described which are the conditions to guarantee that the main physical mechanims behind the localization processes in these experiments are multiple reflections of non-interacting waves, i. e., that the suppression of transport is due to Anderson localization.

We derived our improved analytical description of the long-time localized density profile for experimental BECs by considering the following scenario:

i) For times $0 \leq t \leq t_i$, the first stage, an initially spatially confined condensate starts to expand in a one-dimensional random potential. During this stage, almost all of the energy associated with the interactions between particles is transformed into kinetic energy. This expansion is driven by the interactions between the particles.

ii) For times $t > t_i$, the second stage, the expansion of the condensate comes to a halt, and a quasi-stationary localized density profile is observed. During this stage, the interactions can be neglected.

Similar works on discrete lattices [26], [93] suggest that, in contrast to the latter assumption, interactions lead to a subdiffusive spreading at very long times which, however, we did not investigate in this thesis.

We reviewed in Chapter 2 previous attempts to describe the localized asymptotic density profile theoretically [27], [28]. In these works, the theoretical description for the spatial expansion of the wave packet is based on a simple relation, Eq. (9), between the long-time asymptotic density of the wave packet and the density autocorrelation function of energy eigenstates, see Eq. (3), which takes into account the position and momentum uncertainty of the initial wave packet through its Wigner function, as well as its energy distribution through the spectral

function $A(p, E)$. These works are able to explain the behaviour of the asymptotic density profile in its wings (i. e. for large distances from the initial position), whereas significant deviations between theory and numerics are observed in the center of the profile (i. e. in the vicinity of the initial position) [27], [28]. This failure has its origin in the divergence, at small values of the energy, of the expressions for the Lyapunov coefficient and the spectral function used in [28] and [27].

In contrast to previous works [27], [28], our theory, which we improved with respect to a more accurate description of the Lyapunov exponent (see Chapter 5) and of the spectral function (see Chapter 6), is able to explain, for the non-interacting (and further ahead also for the interacting) case, not only the wings of the spatial density profile at large distances, but also its center in the vicinity of the initial state's position without adjustable parameters.

In order to understand the improvement in our derivation of the Lyapunov exponent in Chapter 5, we first review its definition: The Lyapunov exponent defines the inverse of the localization length, which represents an important quantity to describe the exponential localization of wave functions. Previous works on Anderson localization establish that, in one-dimensional random potentials, all energy eigenfunctions are exponentially localized under very general conditions, and thus exhibit a non-zero Lyapunov exponent, which, in general, depends on the corresponding energy of the eigenfunction. In [27] and [28], the analytical expression of the Lyapunov exponent in a one-dimensional correlated potential was obtained from the Born approximation (see Sec. 5.3). This expression, however, fails for energies close to zero and for negative energies, where it differs from the numerical Lyapunov exponent that we obtained in Sec. 5.2. In contrast, we derived an analytical expression of the Lyapunov exponent on the basis of the works of Thouless [23] and Halperin [25], who found an exact expression for the Lyapunov exponent, valid for all energy ranges in the case of a white noise potential (see Sec. 5.4). This expression is also valid, with good approximation, for random potentials with a finite correlation length σ_c in the regime of small energies, where the wave length of the particle is much larger than σ_c. Using this result, we finally constructed an interpolation between the exact white noise result (valid at low energies) and the Born approximation (valid at large energies) in Sec. 5.5. By comparison with numerical data, we show that this interpolation well describes the Lyapunov exponent in the entire range of energies, for random correlated potentials which satisfy the condition $V_0\sigma_c^2 \ll 1$. This condition implies that the kinetic energy of a particle with wavelength comparable to the correlation length σ_c is much larger than the typical size V_0 of the potential's fluctuations.

Concerning the theoretical description of the spectral function $A(p, E)$, we first calculated the average spectral function in the presence of a random potential using the Born approximation (as also proposed in [28]), which diverges in the low energy regime and vanishes for negative energies. However, from cases where the particle is trapped inside a deep well of the random potential, we expected the existence of states with negative energies, and we suspected that in our model based on Eq. (9), they also play an important role for correctly describing the center of the asymptotic density profile. To treat this problem, we developed a version of the self-consistent Born approximation (see Sec. 6.3). In contrast to the standard self-consistent Born approximation, our version, where only the diverging part $1/\sqrt{E}$ of the self-energy is treated in a self-consistent way, allowed us to finally derive an analytical expression for the spectral function which does not vanish at negative energies.

In Chapter 7, we presented numerical results for the average asymptotic state of a BEC in a one-dimensional disordered potential, $\overline{n(x)}$, and showed that they are well reproduced by our theoretical description, thereby confirming the validity of the latter.

In Chapter 8, we discussed the influence of interactions on the spatial expansion of an initially strongly confined wave packet in a one-dimensional correlated random potential. In Sec. 8.2, we discussed first the numerically observed spreading of an initially localized and interactig wave packet in a one-dimensional discrete lattice with uncorrelated disorder [26], [93]. According to these works, the interacting wave packet exhibits sub-diffusive spreading at very long times, but a quasi-stationary state is reached (for small interactions) at intermediate times. In the present thesis, we focused on the second regime.

In Chapter 9, we showed, by comparison with numerical data, that this quasi-stationary state can be well described within the theory developed for the non-interacting case, provided that the interactions are taken into account through the choice of an effective initial state.

On the analytic proof of Eq. (9)

Besides our improvements in the analytical descriptions of the Lyapunov exponent and of the spectral density, we presented in this thesis an analytic proof of Eq. (9), which is a fundamental element of our theory, since it allows us to express the asymptotic density profile $\overline{n(x)}$ of a wave packet in terms of the density autocorrelation function $\overline{n_E(x)}$ of energy eigenstates at fixed energy E.

The diagrammatic method that we used to calculate $\overline{n(x)}$ has been invented by Berezinskii in 1974 [20]. He developed this method in order to determine the density autocorrelation function $\overline{n_E(x)}$ at fixed energy E introduced in Eq. (3). As explained in Subs. 2.2.2, this function

does not only describe the exponential decay of energy eigenfunctions at large distances, but also corrections to this exponential decay relevant for small distances. We first reviewed Berezinskii's calculation of $\overline{n_E(x)}$ in Sec. 4.1. Then, we modified his method in order to determine $\overline{n(x)}$ in Sec. 4.2. As we have seen, this involves an integration of $\overline{n_E(x)}$ over the energy E, weighted with a suitably defined energy distribution depending on the initial state $\psi_0(x)$ of the wavepacket at time $t = 0$. Whereas a relation similar to Eq. (9) has already been postulated in [28], the present thesis presents a diagrammatic derivation which puts its use on firm theoretical grounds. Our derivation uses the assumption of an initially strongly confined wave packet. Therefore, its applicability to more extended initial states is still an open issue. We note that the opposite extreme case of a wave packet initially strongly confined in momentum space has been treated in [94]. As shown by numerical simulations, the asymptotic momentum distribution exhibits, in this case, two distinct peaks (a coherent backscattering and a coherent forward scattering peak [95]), and can also be described in terms of the autocorrelation function mentioned above.

10.2 OUTLOOK

The theory developed in this thesis will not only be useful for comparison with experiments on Anderson localization in one-dimensional disordered systems, but the improved theoretical insight based on the extension of Berezinskii's diagrammatic technique to the case of wave packets may also serve as a new starting point to explain the spreading of waves in nonlinear disordered systems [87], [93], and thereby to clarify the impact of nonlinearity on the phenomenon of Anderson localization. Given a precise, microscopic understanding of the underlying scattering processes in terms of diagrams, it appears to be promising to include nonlinearities in a similar way as it has been accomplished in order to describe the impact of nonlinearity [96], [97] or interactions between bosons [86], [98] on coherent backscattering.

Part I

APPENDIX

A

SOME IMPORTANT EQUIVALENCES

Equivalence of Eqs. (88) and (89)

In Subs. 4.1.1 we mentioned the equivalence of Eqs. (88) and (89). In order to prove this equivalence, let us introduce the following useful property:

$$\begin{aligned} G^{(-)}(E) - G^{(+)}(E) &= \frac{1}{E - H - i\eta} - \frac{1}{E - H + i\eta}, \\ &= \sum_{n=0}^{\infty} \left(\frac{1}{E - E_n - i\eta} - \frac{1}{E - E_n + i\eta} \right) |\phi_n\rangle\langle\phi_n|, \\ &= 2\pi i \sum_{n=0}^{\infty} \delta(E_n - E) |\phi_n\rangle\langle\phi_n|, \end{aligned} \tag{216}$$

where we used the definition of the Green operator given by Eq. (48), expressed in the basis of eigenstates $\{|\phi_n\rangle\}$ and eigenvalues $\{E_n\}$ from Eq. (15), and also, the following representation of Dirac's δ-function:

$$\delta(E_n - E) = \frac{1}{\pi} \lim_{\eta \to 0} \frac{\eta}{(E_n - E)^2 - \eta^2}, \tag{217}$$

in the limit $\eta \to 0$.

The difference between the Green propagators in Eq. (216) from positions x to x' is:

$$G^{(-)}(x', x, E) - G^{(+)}(x', x, E) = 2\pi i \sum_{n=0}^{\infty} \delta(E_n - E) \langle x'|\phi_n\rangle\langle\phi_n|x\rangle, \tag{218}$$

as well as

$$G^{(+)}(x, x', E + \omega) = \sum_{q=0}^{\infty} \frac{\langle x|\phi_q\rangle\langle\phi_q|x'\rangle}{E - E_q + \omega}, \tag{219}$$

from the position x' to x.

Using Eqs. (218) and (219), we obtain:

$$\begin{aligned} &\lim_{\omega \to 0} \frac{\omega}{2\pi i \overline{\rho_E}} G^{(+)}(x, x', E + \omega) \times \left(G^{(-)}(x', x, E) - G^{(+)}(x', x, E) \right) \\ &= \lim_{\omega \to 0} \frac{\omega}{\overline{\rho_E}} \sum_{n=0}^{\infty} \sum_{q=0}^{\infty} \delta(E_n - E) \frac{\langle x'|\phi_n\rangle\langle\phi_n|x\rangle\langle x|\phi_q\rangle\langle\phi_q|x'\rangle}{E_n - E_q + \omega}, \end{aligned} \tag{220}$$

where we replaced in the denominator E by E_n due to the δ-function $\delta(E - E_n)$. The limit $\omega \to 0$ now asserts:

$$\lim_{\omega\to 0} \frac{\omega}{E_n - E_q - \omega} = \delta_{nq}. \tag{221}$$

thereby, we can recover the expression Eq. (88) for $n_E(x, x')$:

$$\begin{aligned} & \lim_{\omega\to 0} \frac{\omega}{2\pi i \overline{\rho_E}} G^{(+)}(x, x', E + \omega) \times \left(G^{(-)}(x', x, E) - G^{(+)}(x', x, E) \right) \\ = & \sum_{n=0}^{\infty} |\langle x|\phi_n\rangle\langle\phi_n|x'\rangle|^2 \delta(E_n - E)/\overline{\rho_E} \\ = & \; n_E(x, x'). \end{aligned} \tag{222}$$

as stated in Eq. (89).

Equivalence between the average Eq. (24) and (107)

Taking the average of Eq. (24), we may write:

$$\begin{aligned} \overline{n(x)} &= \sum_{n=0}^{\infty} \overline{|\langle x|\phi_n\rangle\langle\phi_n|\psi_0\rangle|^2}, \\ &= \int_{-\infty}^{\infty} \mathrm{d}E \; \overline{\sum_{n=0}^{\infty} |\langle x|\phi_n\rangle\langle\phi_n|\psi_0\rangle|^2 \delta(E_n - E)}. \end{aligned} \tag{223}$$

Introducing the spatial coordinate clausure relation, i. e., $\int_{-\infty}^{\infty} \mathrm{d}x|x\rangle\langle x| = \mathbb{1}$, in Eq. (223), we obtain:

$$\begin{aligned} \overline{n(x)} = \int_{-\infty}^{\infty} \mathrm{d}E \int_{-\infty}^{\infty} \mathrm{d}x''\mathrm{d}x''' \; \langle x''|\psi_0\rangle\langle\psi_0|x'''\rangle \times \\ \overline{\sum_{n=0}^{\infty} \langle x|\phi_n\rangle\langle\phi_n|x\rangle\langle x''|\phi_n\rangle\langle\phi_n|x'''\rangle \delta(E_n - E)}. \end{aligned} \tag{224}$$

In order to demostrate the equivalence between Eqs. (107) and (224), we use Eqs. (218) and (219), where we replace x' by x'' or x'', respectively:

$$\begin{aligned} G^{(-)}(x''', x, E) - G^{(+)}(x''', x, E) = 2\pi i \times \\ \sum_{n=0}^{\infty} \delta(E_n - E)\langle x'''|\phi_n\rangle\langle\phi_n|x\rangle, \end{aligned} \tag{225}$$

and:

$$G^{(+)}(x, x'', E + \omega) = \sum_{q=0}^{\infty} \frac{\langle x|\phi_q\rangle\langle\phi_q|x''\rangle}{E - E_q + \omega}. \tag{226}$$

Using the ensemble average of the product of the Eqs. (225) and (226) in Eq. (107), where we neglect the products $\overline{G^{(+)}(x, x'', E + \omega)G^{(+)}(x''', x, E)}$ due to its random phases, we recover the expression given by Eq. (224).

B

BEREZINSKII'S METHOD FOR WAVE PACKETS

In this appendix, we generalize the diagrammatic method of Berezinskii (see Chapter 4) to the case of a wave packet. As we already explained in Subs. 4.2.1, we must, for this purpose, consider the intensity propagator $\tilde{\Phi}(x, x'', x''', E, \omega)$ with two different source points x'' and x''':

$$\tilde{\Phi}(x, x'', x''', E, \omega) = \overline{G^{(+)}(x, x'', E+\omega) G^{(-)}(x''', x, E)},$$

see Eq. (108).

In Subs. 4.2.2, we neglected the disorder in the vicinity of the source points. In this case, we obtain the final result, Eq. (9), but with the spectral function $A_0(p, E)$ of a free particle instead of the spectral function $A(p, E)$ in the presence of disorder.

In this appendix, we show that $A(p, E)$ is recovered if the disorder in the vicinity of the source points is taken into account. Let us first assume $x'' < x''' < x$ and a particle initially propagating towards the right-hand side, as in the example shown in Fig. (13). Obviously, the difference with respect to the original Berezinskii diagram shown in Fig. (10) only concerns the part between the source points x'' and x'''. Here, the number of solid lines $(2m+1)$ and dashed lines $(2m)$ is not identical. We thus introduce the quantity $A_m(x)$ describing this additional part. The differential equation for $A_m(x)$ can be obtained in a similar way as described above:

$$\frac{\mathrm{d}A_m}{\mathrm{d}x} = \Big[-\frac{1}{2\ell_-} - \frac{1}{2\ell_+} - \frac{i}{2\ell_0} - \Big(m^2 + (m-1)m\Big)\frac{1}{\ell_-}\Big] A_m + \frac{1}{\ell_-}\Big(m^2 A_{m-1} e^{-i\omega x/p_E} + m(m+1) A_{m+1} e^{i\omega x/p_E}\Big). \quad (227)$$

As boundary condition, we impose $A_m(x'') = \tilde{L}_m(x'')$, since the additional part A must be connected to the left-hand part $\tilde{L}$ at $x = x''$. Similarly to Eq. (101), we obtain:

$$\tilde{\Phi}(x, x'', x''', E, \omega) = \tilde{\Phi}_R(x, x'', x''', E, \omega) + \tilde{\Phi}_L(x, x'', x''', E, \omega), \quad (228)$$

where

$$\tilde{\Phi}_R(x, x'', x''', E, \omega) = e^{ip_E(x'''-x'')} \frac{e^{-\frac{i\omega x''}{2p_E}}}{4p_E^2} \sum_{m,m'=0}^{\infty} A_{m'}(x''') \times Z_{m',m}(x''', x)\Big(e^{\frac{i\omega x}{2p_E}} \tilde{R}_m(x) + e^{-\frac{i\omega x}{2p_E}} \tilde{R}_{m+1}(x)\Big) \quad (229)$$

and similarly for $\tilde{\Phi}_L(x, x'', x''', E, \omega)$ (see below). Let us now compare Eqs. (102,229).

The essential difference consists of the term $\tilde{L}_{m'}(x')Z_{m',m}(x', x)$ occurring in Eq. (102) instead of $A_{m'}(x''')Z_{m',m}(x''', x)$ in Eq. (229). Expanding the solution of Eq. (227) in first order of $x''' - x''$, we obtain:

$$A_{m'}(x''') = \tilde{L}_{m'}(x'') + (x''' - x'')\left\{\left[-\frac{1}{2\ell_-} - \frac{1}{2\ell_+} - \frac{i}{2\ell_0} - \left((m')^2 + (m'-1)m'\right)\frac{1}{\ell_-}\right]\tilde{L}_{m'}(x'') + \frac{1}{\ell_-}\left((m')^2\tilde{L}_{m'-1}(x'')e^{-i\omega x''/p_E} + m'(m'+1)\tilde{L}_{m'+1}(x'')e^{i\omega x''/p_E}\right)\right\}. \tag{230}$$

Similarly, we have:

$$\tilde{L}_{m'}(x'') = \tilde{L}_{m'}(x') - \frac{x' - x''}{\ell_-}\left((m')^2\tilde{L}_{m'-1}(x')e^{-i\omega x'/p_E} + (m')^2\tilde{L}_{m'+1}(x')e^{i\omega x'/p_E} - 2(m')^2\tilde{L}_{m'}(x')\right) \tag{231}$$

and

$$Z_{m',m}(x''', x) = Z_{m',m}(x', x) - \frac{x''' - x'}{\ell_-}\left((m')^2 Z_{m'-1,m}(x', x)e^{i\omega x'/p_E} + (m'+1)^2 Z_{m'+1,m}(x', x)e^{-i\omega x'/p_E} - \left((m')^2 + (m'+1)^2\right)Z_{m',m}(x', x)\right) \tag{232}$$

where Eq. (231) results from Eq. (105) together with $\tilde{L}_m(x) = \tilde{R}_m(-x)$, and Eq. (232) from Eq. (104b) together with $Z_{m',m}(x, x') = Z_{m,m'}(-x', -x)$. Summing over m' and keeping again only terms linear in the difference $x''' - x'' = 2(x' - x'') = 2(x''' - x')$ (since $x' = \frac{x''+x'''}{2}$), we obtain:

$$\sum_{m'} A_{m'}(x''')Z_{m',m}(x''', x) = \sum_{m'}\tilde{L}_{m'}(x')Z_{m',m}(x', x) + (x''' - x'')\left(-\frac{1}{2\ell_-} - \frac{1}{2\ell_+} - \frac{i}{2\ell_0}\right)\sum_{m'}\tilde{L}_{m'}(x')Z_{m',m}(x', x) + \sum_{m'}(x''' - x'')e^{-i\omega m x'/p_E}\frac{R_{m'+1} - R_{m'}}{2}Z_{m',m}(x', x). \tag{233}$$

The term $R_{m'+1} - R_{m'}$ can be neglected in the limit $m' \to \infty$ corresponding to $\omega \to 0$ [20]. Defining the effective complex wavevector

$$\tilde{p}_E = p_E + \frac{i}{2\ell_-} + \frac{i}{2\ell_+} - \frac{1}{2\ell_0} \tag{234}$$

describing average propagation in the random potential, Eq. (117) follows from Eqs. (102, 229, 232):

$$\tilde{\Phi}_R(x,x'',x''',E,\omega) = e^{i\tilde{p}_E(x'''-x'')}\Phi_R(x,x',E,\omega) \tag{235}$$

for small ω and small $x''' - x''$.

The corresponding relation for $\tilde{\Phi}_L(x,x'',x''',E,\omega)$ can immediately be deduced from Eq. (235), since an initially left-propagating diagram can be mapped to a right-propagating one by exchanging solid with dashed lines and inverting the coordinates, i. e.,

$$\tilde{\Phi}_L(x,x'',x''',E,\omega) = \tilde{\Phi}^*_R(-x,-x''',-x'',E+\omega,-\omega) \tag{236}$$

and

$$\Phi_L(x,x',E,\omega) = \Phi^*_R(-x,-x',E+\omega,-\omega). \tag{237}$$

From this, we obtain Eq. (118)

$$\tilde{\Phi}_L(x,x'',x''',E,\omega) = e^{-i\tilde{p}^*_E(x'''-x'')}\Phi_L(x,x',E,\omega).$$

Taking into account that for small ω, $\Phi_R(x,x',E,\omega) = \Phi_L(x,x',E,\omega)$, the sum of Eqs. (117, 118) yields:

$$\rho_E \overline{G^{(+)}(x,x'',E+\omega)G^{(+)}_E(x''',x,E)} = \frac{e^{i\tilde{p}_E|x'''-x''|} + e^{-i\tilde{p}^*_E|x'''-x''|}}{4\pi p_E} \times \overline{G^{(+)}(x,x',E+\omega)G^{(+)}_E(x',x,E)} \tag{238}$$

where we included the normalization factor $\rho_E = 1/(2\pi p_E)$ on both sides of the equation. This expression is valid also for $x''' < x''$ (as can be proven by inverting the sign of all spatial arguments and exchanging $L \leftrightarrow R$). Our aim is to show, that the prefactor on the right-hand side of Eq. (238) reproduces the imaginary part of the average Green function. According to the Dyson equation (see Sec. 3.3.3) the latter is related as follows

$$\begin{aligned}\overline{G^{(+)}(x''-x''',E)} &= G^{(+)}_0(x''-x''',E) \\ &+ \int_{-\infty}^{\infty} \mathrm{d}\tilde{x}\; G^{(+)}_0(x''-\tilde{x},E)\Sigma(E)\overline{G^{(+)}(\tilde{x}-x''',E)}\end{aligned} \tag{239}$$

to the self-energy $\Sigma(E)$, which, using the Born approximation, Eq. (182), is given by $\Sigma(E) = p_E^2 - \tilde{p}_E^2 \simeq -2p_E(\tilde{p}_E - p_E)$, with $\tilde{p}_E$ as defined in Eq. (234). Diagrammatically, this self energy corresponds to vertex a displayed in Fig. (11). The solution of Eq. (239) is given by Eq. (77), which has the same form as the free-particle Green function, see Eq. (57), but with the wave number p_E replaced by the effective wave number $\tilde{p}_E$.

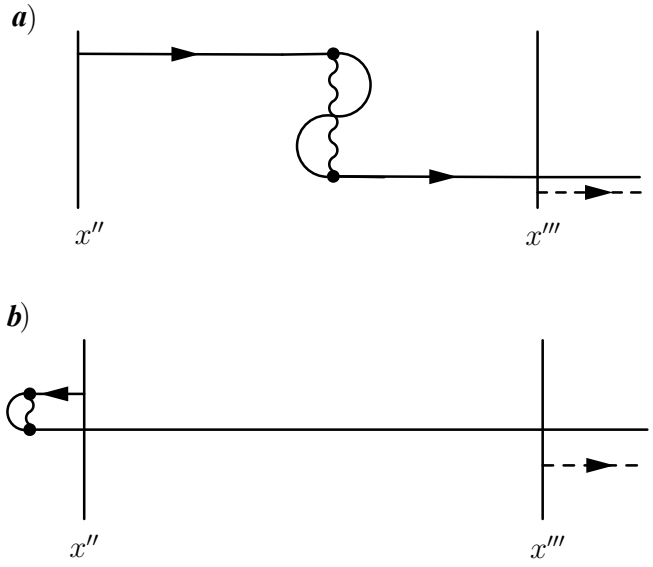

Fig. (39) (a) Inserting the vertex Fig. (11 a) on the line between x'' and x''' yields the first-order expansion (in $x''' - x''$) of the term $\exp[i\tilde{p}_E(x''' - x'')]$. (b) The denominator $1/\tilde{p}_E$ present in the average Green function, see Eq. (77) is recovered by diagrams where the vertex occurs outside the interval $[x'', x''']$.

As compared to the prefactor in Eq. (238), however, the denominator $1/p_E$ is replaced by $1/\tilde{p}_E$. Although this difference is small in the validity regime of the diagrammatic approach ($p_E\ell_- \gg 1$), we will show in the following how the factor $1/\tilde{p}_E$ can be recovered by considering additional diagrams.

In our above derivation, we have restricted ourselves to diagrams where vertex a is inserted only in the interval between x'' and x''', as indicated in Fig. (12). Here, we focus on the initial stage of propagation, i. e., we consider the solid line originating from the source point x'' until it passes the second source point x'''. Up to first order in $x''' - x''$, the contribution from these diagrams to the average Green function, $\overline{G^{(+)}(x'' - x''', E)}$, reads:

$$G_0^{(+)}(x'' - x''', E) + \int_{x''}^{x'''} \mathrm{d}\tilde{x}\; G_0^{(+)}(x'' - \tilde{x}, E)\Sigma(E)G_0^{(+)}(\tilde{x} - x''', E) = G_0^{(+)}(x'' - x''', E)\left(1 + i(\tilde{p}_E - p_E)(x''' - x'')\right) \simeq -\frac{i}{p_E}e^{i\tilde{p}_E(x''' - x'')}, \tag{240}$$

which exhibits p_E instead of $\tilde{p}_E$ in the denominator, as in Eq. (238). According to Eq. (239) – where the integration over $\tilde{x}$ is not restricted to $[x'', x''']$ –and its solution, Eq. (77), the denominator $1/\tilde{p}_E$ is recovered if the vertex a is inserted outside the interval $[x'', x''']$, as in the diagram depicted in Fig. (39).

This finally yields:

$$\overline{n(x)} = \int_{-\infty}^{\infty} \mathrm{d}E \int_{-\infty}^{\infty} \mathrm{d}x'' \mathrm{d}x''' \overline{n_E\left(x - \frac{x'' + x'''}{2}\right)} \langle x''|\psi_0\rangle\langle\psi_0|x'''\rangle \times \left(-\Im\left\{\overline{G^{(+)}(x'' - x''', E)}\right\}\right) \quad (241)$$

where, as compared to Eq. (114), the free-particle Green function is replaced by the average Green function. Since the imaginary part of the Green function defines the spectral function $A(p, E)$, see Eq. (174), we obtain our final result, Eq. (9); which is the same as Eq. (116), but with $A_0(p, E)$ replaced by $A(p, E)$. This result is valid under the assumption of a strongly confined initial wave packet ($\sigma \ll \ell_-$), where the first-order expansion in the difference $x''' - x''$ between the two source points, which we applied several times in our above derivation, is justified.

C

NUMERICAL INTEGRATION SCHEMES

Finite element discrete varible representation (FEDVR)

The name FEDVR arises from finite element (FE) and discrete variable representation (DVR). The numerical integration scheme consists of splitting an interval $[x^0, x^{n_e}]$ into n_e finite elements $[x^i, x^{i+1}]$ (where $i = 0, ..., n_e - 1$). In each finite element i, there are $n - 1$ Gauss-Lobatto points, x_m^i (with weights w_m^i), $m = 1, ..., n - 1$, defined in terms of stationary points x_m of the Legendre polynomial, $P_n(x)$. Then, every FE has its local n element basis, which will be used to expand the wave functions and relevant operators in a problem to study [75], [77], [99]. See Fig. (40).

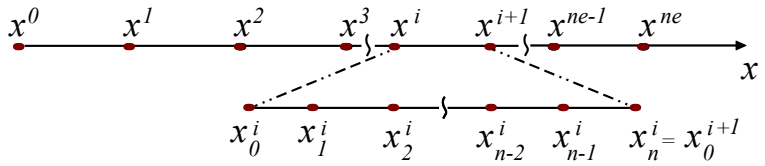

Fig. (40) FEDVR representation. The interval $[x^0, x^{n_e}]$ is divided in n_e finite elements $[x_0^i, x_0^{i+1}]$.

We construct the DVR local basis using the translated Gauss-Lobatto points x_m^i with weights w_m^i. First, the Gauss-Lobatto points (x_m) are defined as the roots of the first derivative of the Legendre polynomial $P_n(x)$:

$$\frac{\mathrm{d}P_n(x_m)}{\mathrm{d}x} = 0 \quad m = 1, ..., n - 1, \tag{242}$$

whereas $x_0 = -1$ and $x_n = +1$. The associated weights are defined by:

$$w_m = \frac{2}{n(n+1)[P_n(x_m)]^2}, \tag{243}$$

where $m = 0, ..., n$. Secondly, since the zeros of $P_n'(x)$ are between -1 and 1, we must move the Gauss-Lobatto points x_m (and weights w_m) to the i-th finite element using the following rule for positions:

$$x_m^i = \frac{1}{2}[(x^{i+1} - x^i)x_m + (x^{i+1} + x^i)], \tag{244}$$

and for the weights:

$$w_m^i = \frac{w_m}{2}(x^{i+1} - x^i), \tag{245}$$

where x_m^i and w_m^i (with $m = 0, 1, ..., n$) are the Gauss-Lobatto and their weights in the i-th finite element, respectively. Note that the points x_m^i are between x^i and x^{i+1}.

The advantage of using Gauss-Lobatto on the DVR is the possibility to approximate integrals as sums using *Gauss-Lobatto quadrature*: For every FE the integral of a function $g(x)$ in the interval $[x_0^1, x_n^i]$ is approximated as:

$$\int_{x_0^i}^{x_n^i} \mathrm{d}x\; g(x) \approx \sum_{m=0}^{n} g(x_m^i) w_m^i, \tag{246}$$

which is exact for a polynomial of degree $\leq 2n + 1$. To construct a DVR based on the Gauss-Lobatto quadrature, we use the Lobatto shape functions for the intervals $x_j^i \leq x \leq x_{j+1}^i$:

$$f_m^i(x) = \prod_{j \neq i} \frac{(x - x_j^i)}{(x_m^i - x_j^i)}, \tag{247}$$

where $f_m^i(x) = 0$ for $x < x_j^i$ or $x > x_{j+1}^i$. Thereby, the basis functions are defined in terms of $f_m^i(x)$:

$$\chi_m^i(x) = \begin{cases} \frac{f_n^{i-1}(x) + f_0^i(x)}{\sqrt{w_n^{i-1} + w_0^i}}, & m = 0, \\ \frac{f_m^i(x)}{\sqrt{w_m^i}}, & m = 1, 2, ..., n-1. \end{cases} \tag{248}$$

Due to Eq. (247), note that the functions χ_m^i in Eq. (248) fulfill:

$$\chi_m^i(x_{m'}^{i'}) = \begin{cases} \frac{\delta_{ii'}}{\sqrt{w_m^{i-1} + w_0^i}}, & m = 0, \\ \frac{\delta_{ii'}\delta_{mm'}}{\sqrt{w_m^i}}, & m = 1, 2, ..., n-1. \end{cases} \tag{249}$$

Fig. (41) shows the basis functions for $n = 4$.

Initial state and Hamiltonian in DRV

Once having defined the basis functions, we may expand the initial state $\psi(x)$ as:

$$\psi(x) = \sum_{i,m} c_m^i \chi_m^i(x), \tag{250}$$

where

$$c_m^i = \psi(x_m^i) \times \begin{cases} \sqrt{w_n^{i-1} + w_0^i}, & m = 0, \\ \sqrt{w_m^i}, & m = 1, 2, ..., n-1. \end{cases} \tag{251}$$

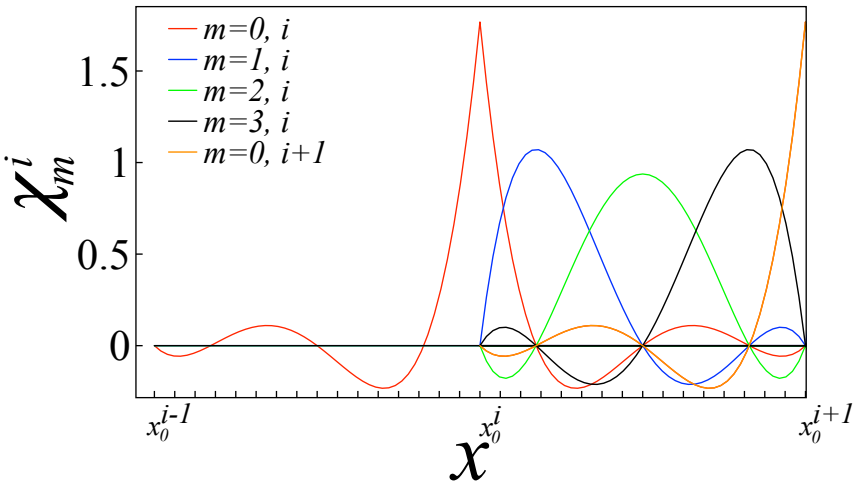

Fig. (41) Basis functions $\{\chi_m^i(x)\}$ for $m = 0, 1, 2, 3$ and $\chi_0^{i+1}(x)$. The function $\chi_0^i(x)$ represents a bridge-function between the two FE intervals $i-1$ and i. For $m = 1, 2, 3$ the functions $\chi_m^i(x)$ are not zero only in the i-th FE interval.

follows from Eq. (249). We may also expand the kinetic and potential operators of the Hamiltonian Eq. (15). We expand first the kinetic energy as $t_{m_1,m_2}^{i_1,i_2}$:

$$t_{m_1,m_2}^{i_1,i_2} = -\frac{1}{2}\int_{x^0}^{x^{n_e}} \mathrm{d}x\ \chi_{m_1}^{i_1}(x)\nabla^2\chi_{m_2}^{i_2}(x)$$

$$= \begin{cases} \dfrac{\delta_{i_1 i_2}\tilde{t}_{m_1 m_2}^{i_1}}{2\sqrt{w_{m_1}^{i_1} w_{m_2}^{i_1}}}, & m_1 > 0,\ m_2 > 0,\ (\times) \\ \dfrac{(\delta_{i_1 i_2}\tilde{t}_{n-1 m_2}^{i_1} + \delta_{i_1 i_2 - 1}\tilde{t}_{0 m_2}^{i_2})}{\sqrt{w_{n-1}^{i_1} + w_0^{i_1+1}}}, & m_1 = 0,\ m_2 > 0,\ (\circ) \\ \dfrac{(\delta_{i_1 i_2}\tilde{t}_{m_1 n-1}^{i_1} + \delta_{i_1 i_2+1}\tilde{t}_{m_1 0}^{i_1})}{\sqrt{w_{m_1}^{i_1}(w_{n-1}^{i_1} + w_0^{i_2+1})}}, & m_1 > 0,\ m_2 = 0,\ (\otimes) \\ \dfrac{\delta_{i_1 i_2}(\tilde{t}_{n-1 n-1}^{i_1} + \tilde{t}_{00}^{i_1+1}) + \delta_{i_1 i_2 - 1}\tilde{t}_{0 n-1}^{i_2} + \delta_{i_1 i_2+1}\tilde{t}_{n-1 0}^{i_1}}{2\sqrt{(w_{n-1}^{i_1} + w_0^{i_1+1})(w_{n-1}^{i_2} + w_0^{i_2+1})}}, & m_1 = m_2 = 0,\ (*) \end{cases} \tag{252}$$

where $\tilde{t}_{m_1,m_2}^i$ is defined via:

$$\tilde{t}_{m_1,m_2}^i = \sum_m \frac{\mathrm{d}f_{m_1}^i(x_m^i)}{\mathrm{d}x}\frac{\mathrm{d}f_{m_2}^i(x_m^i)}{\mathrm{d}x} w_m^i. \tag{253}$$

And after, we expand the potential as $v_{m_1 m_2}^{i_1 i_2}$:

$$v_{m_1 m_2}^{i_1 i_2} = \int_{x^0}^{x^{n_e}} \mathrm{d}x\ \chi_{m_1}^{i_1}(x)V(x)\chi_{m_2}^{i_2}(x) = \delta_{i_1 i_2}\delta_{m_1 m_2} v_{m_1}^{i_1}, \tag{254}$$

with

$$v_m^i = \begin{cases} \frac{V(x_{n-1}^i)w_{n-1}^i + V(x_0^{i+1})w_0^{i+1}}{w_{n-1}^i + w_{i+1}^0}, & m = 0 \\ V(x_m^i), & m = 1, 2, ..., n-1 \end{cases} \tag{255}$$

The matrix representation of p^2, Eq. (252), used for the diagonalization of the Hamiltonian Eq. (15), has the following form:

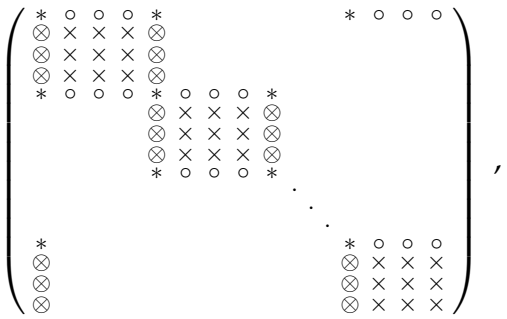

, (256)

where the symbols denote non-zero elements and the elements at the corners (up right and down left) are due to the periodical boundary conditions. Every one of the blocks in the matrix representation is related with the i-th FE. The matrix representation of $V(x)$, Eq. (255), is purely diagonal.

The second-order differencing scheme (SOD)

For closed systems, the unitary propagation can be calculated numerically by the expansion of the evolution operator into a Taylor series [100]:

$$U(t) = 1 - iH\Delta t + \cdots . \tag{257}$$

After truncation of the series at certain order of Δt, however, the operator $U(t)$ is not unitary any more, and thus violates energy and momentum conservation. To avoid this problem, the second order differencing scheme (SOD) is used as follows

$$\begin{aligned} |\psi(t+\Delta t)\rangle - |\psi(t-\Delta t)\rangle &= (e^{-iH\Delta t} - e^{iH\Delta t})|\psi(t)\rangle, \\ |\psi(t+\Delta t)\rangle &\approx |\psi(t-\Delta t)\rangle - 2i\Delta t H|\psi(t)\rangle. \end{aligned} \tag{258}$$

To prove the unitary and energy-conserving property of the SOD scheme, we can multiply Eq. (258) by $\langle\psi(t)|$:

$$\langle\psi(t)|\psi(t+\Delta t)\rangle = \langle\psi(t)|\psi(t-\Delta t)\rangle - 2i\Delta t\langle\psi(t)|H|\psi(t)\rangle. \tag{259}$$

Conjugating Eq. (259), adding Eq. (259) and integrating over all space, we get:

$$\int_{-\infty}^{\infty} \mathrm{d}x\, \psi(x, t-\Delta t)\psi^*(x,t) = \int_{-\infty}^{\infty} \mathrm{d}x\, \psi(x,t)\psi^*(x,t+\Delta t) = \text{const.} \tag{260}$$

Since, for small Δt ($\Delta t \ll E_{max}$, where E_{max} is the eigenvalue with largest absolute value of the discrete Hamiltonian) the state $|\psi(t+\Delta t)\rangle$ is very close to $|\psi(t)\rangle$, Eq. (260) ensures the conservation of the total norm $\langle\psi(t)|\psi(t)\rangle$. Following the same steps, but with the function $H|\psi(t)\rangle$, the energy conservation for different time steps (t and $t+\Delta t$) is demonstrated as follows:

$$\int_{-\infty}^{\infty} \mathrm{d}x\ \psi(x,t-\Delta t)H\psi^*(x,t) = \text{const.} \tag{261}$$

SOD recurrence

Using Eq. (258) for $t=0$ and $t=\Delta t/2$, we may get $|\psi(\Delta t)\rangle$ in terms of $|\psi(t=0)\rangle$ and $|\psi(\Delta t/2)\rangle$ [100]:

$$|\psi(\Delta t)\rangle \approx |\psi(t=0)\rangle - i\Delta t H|\psi(\Delta t/2)\rangle. \tag{262}$$

In order to get $|\psi(\Delta t/2)\rangle$ as a function of $|\psi(t=0)\rangle$, we use the first-order scheme:

$$|\psi(\Delta t/2)\rangle \approx |\psi(t=0)\rangle - i(\Delta t/2)H|\psi(t=0)\rangle. \tag{263}$$

Then, with help of Eq. (263), we can propagate the state $|\psi(t=0)\rangle$ in time using the following recurrence for the SOD scheme:

$$|\psi(n\Delta t)\rangle \approx |\psi((n-2)\Delta t)\rangle - 2i\Delta t H|\psi((n-1)\Delta t)\rangle, \tag{264}$$

for $n = 2, 3, ...$

In case of a time dependent Hamiltonian $H(t)$, see Eq. (197), the SOD scheme is applied as follows: we replace H by $H(t)$ in Eq. (258), $H(\Delta t/2)$ in Eq. (262), $H(0)$ in Eq. (263), and $H((n-1)\Delta t)$ in Eq. (264).

Fourier Propagation

To check the results obtained with the SOD scheme in Chapter 9, we compare then with an alternative method: the Fourier propagation scheme. This scheme relies on the fact that in

$$H(t) = p^2 + V, \tag{265}$$

the kinetic energy p^2 is diagonal in momentum space, whereas V is diagonal in position space.

For small Δt, we approximate:

$$|\phi(t+\Delta)\rangle = e^{-iV\Delta t/2}e^{-ip^2\Delta t}e^{-iV\Delta t/2}|\phi(t)\rangle. \tag{266}$$

If $|\phi(t)\rangle$ is represented in position space, the first term, i. e. $e^{-iV\Delta t/2}$, amounts to a multiplication with a complex phase factor:

$$\langle x|e^{-iV\Delta t/2}|\phi(t)\rangle = e^{-iV(x)\Delta t/2}\langle x|\phi(t)\rangle. \tag{267}$$

To evaluate the second term, i. e. $e^{-ip^2\Delta t}$, we apply the Fourier transform:

$$\tilde{\phi}(k,t) = \mathcal{F}\phi(x,t) = \frac{1}{L}\int_0^L \mathrm{d}x\; e^{-ikx}\phi(x,t) \tag{268a}$$

with L the length of the 1D potential (remember that we impose periodic boundary conditions with period L), and the back transform

$$\phi(x,t) = \mathcal{F}^{-1}\phi(k,t) = \sum_k e^{ikx}\phi(k,t), \tag{268b}$$

where $k = 2n\pi/L$, $n \in \mathbb{Z}$. Thereby, we write the propagator

$$\phi(x,t+\Delta) = e^{-iV(x)\Delta t/2}e^{-ip^2\Delta t}e^{-iV(x)\Delta t/2}\phi(x,t), \tag{269}$$

in terms of Fourier transforms and multiplication with complex numbers:

$$\phi(x,t+\Delta) = e^{-iV(x)\Delta t/2}\mathcal{F}^{-1}e^{-ik^2\Delta t}\mathcal{F}e^{-iV(x)\Delta t/2}\phi(x,t). \tag{270}$$

In case of the Gross-Pitaevskii equation, see Chapter 8, we replace $V(x)$ by $V(x) + g|\psi(x,t)|^2$ in Eq. (270).

BIBLIOGRAPHY

[1] P. Drude, "Zur Elektronentheorie der Metalle," *Ann. Phys.*, vol. 306, no. 3, pp. 566–613, 1900.

[2] ——, "Zur Elektronentheorie der Metalle; ii. Teil. Galvanomagnetische und thermomagnetische effekte," *Ann. Phys.*, vol. 308, no. 11, pp. 369–402, 1900.

[3] F. Bloch, "Über die Quantenmechanik der Elektronen in Kristallgittern," *Z. Phys.*, vol. 52, no. 7, pp. 555–600, 1929.

[4] P. W. Anderson, "Absence of diffusion in certain random lattices," *Phys. Rev.*, vol. 109, pp. 1492–1505, 5 1958.

[5] A. Rodríguez, "One-dimensional models of disordered quantum wires: General formalism," *J. Phys. A*, vol. 39, no. 46, p. 14 303, 2006.

[6] F. Evers and A. D. Mirlin, "Anderson transitions," *Rev. Mod. Phys.*, vol. 80, pp. 1355–1417, 4 2008.

[7] N. Mott and W. Twose, "The theory of impurity conduction," *Adv. Phys.*, vol. 10, no. 38, pp. 107–163, 1961.

[8] A. Lagendijk, B. v. Tiggelen, and D. S. Wiersma, "Fifty years of Anderson localization," *Phys. Today*, vol. 62, no. 8, pp. 24–29, 2009.

[9] E. Abrahams, P. W. Anderson, D. C. Licciardello, and T. V. Ramakrishnan, "Scaling theory of localization: Absence of quantum diffusion in two dimensions," *Phys. Rev. Lett.*, vol. 42, pp. 673–676, 10 1979.

[10] D. H. Dunlap, H.-L. Wu, and P. W. Phillips, "Absence of localization in a random-dimer model," *Phys. Rev. Lett.*, vol. 65, pp. 88–91, 1 1990.

[11] F. M. Izrailev and A. A. Krokhin, "Localization and the mobility edge in one-dimensional potentials with correlated disorder," *Phys. Rev. Lett.*, vol. 82, pp. 4062–4065, 20 1999.

[12] Y. Lahini, A. Avidan, F. Pozzi, M. Sorel, R. Morandotti, D. N. Christodoulides, and Y. Silberberg, "Anderson localization and nonlinearity in one-dimensional disordered photonic lattices," *Phys. Rev. Lett.*, vol. 100, p. 013 906, 1 2008.

[13] U. Kuhl, F. M. Izrailev, and A. A. Krokhin, "Enhancement of localization in one-dimensional random potentials with long-range correlations," *Phys. Rev. Lett.*, vol. 100, p. 126 402, 12 2008.

[14] H. Hu, A. Strybulevych, J. H. Page, S. E. Skipetrov, and B. A. van Tiggelen, "Localization of ultrasound in a three-dimensional elastic network," *Nat Phys*, vol. 4, no. 12, pp. 945–948, Dec. 2008.

[15] B. von Tiggelen, *Localization of waves in: Diffusive waves in complex media*, J. P. Fouque, Ed. Academic Publischers, Dordrecht, 1999, 1999, pp. 1–60.

[16] M. P. V. Albada and A. Lagendijk, "Observation of weak localization of light in a random medium," *Phys. Rev. Lett.*, vol. 55, pp. 2692–2695, 24 1985.

[17] D. S. Wiersma, P. Bartolini, A. Lagendijk, and R. Righini, "Localization of light in a disordered medium," *Nature*, vol. 390, pp. 671–673, 1997.

[18] B. Damski, J. Zakrzewski, L. Santos, P. Zoller, and M. Lewenstein, "Atomic Bose and Anderson glasses in optical lattices," *Phys. Rev. Lett.*, vol. 91, p. 080 403, 8 2003.

[19] Y. Dubi, Y. Meir, and Y. Avishai, "Nature of the superconductor-insulator transition in disordered superconductors," *Nature*, vol. 449, no. 7164, pp. 876–880, Oct. 2007.

[20] V. L. Berezinskii, "Kinetics of a quantum particle in a one-dimensional random potential," *Sov. Phys. JETP*, vol. 38(3), p. 620, 1974.

[21] A. A. Gogolin, V. L. Mel'nikov, and E. I. Rashba, "Conductivity in a disordered one-dimensional system induced by electron-phonon interaction," *Sov. Phys. JETP*, vol. 42(1), p. 168, 1976.

[22] A. A. Gogolin, "Electron density distribution for localized states in a one-dimensional disordered system," *Sov. Phys. JETP*, vol. 44(5), p. 1003, 1976.

[23] D. J. Thouless, "A relation between the density of states and range of localization for one dimensional random systems," *J. Phys. Condens. Matter*, vol. 5, no. 1, p. 77, 1972.

[24] K. Jänich, *Analysis für Physiker und Ingenieure*. Springer-Lehrbuch, Berlin, 1975, p. 128.

[25] B. I. Halperin, "Green's functions for a particle in a one-dimensional random potential," *Phys. Rev.*, vol. 139, A104–A117, 1A 1965.

[26] A. S. Pikovsky and D. L. Shepelyansky, "Destruction of Anderson localization by a weak nonlinearity," *Phys. Rev. Lett.*, vol. 100, p. 094 101, 9 2008.

[27] L. Sanchez-Palencia, D. Clément, P. Lugan, P. Bouyer, G. V. Shlyapnikov, and A. Aspect, "Anderson localization of expanding Bose-Einstein condensates in random potentials," *Phys. Rev. Lett.*, vol. 98, p. 210 401, 21 2007.

[28] M. Piraud, P. Lugan, P. Bouyer, A. Aspect, and L. Sanchez-Palencia, "Localization of a matter wave packet in a disordered potential," *Phys. Rev. A*, vol. 83, p. 031 603, 3 2011.

[29] J. Billy, V. Josse, Z. Zuo, A. Bernard, B. Hambrecht, P. Lugan, D. Clément, L. Sanchez-Palencia, P. Bouyer, and A. Aspect, "Direct observation of Anderson localization of matter waves in a controlled disorder," *Nature*, vol. 453, pp. 891–894, 2008.

[30] D. Clément, A. F. Varón, M. Hugbart, J. A. Retter, P. Bouyer, L. Sanchez-Palencia, D. M. Gangardt, G. V. Shlyapnikov, and A. Aspect, "Suppression of transport of an interacting elongated Bose-Einstein condensate in a random potential," *Phys. Rev. Lett.*, vol. 95, p. 170 409, 17 2005.

[31] C. Fort, L. Fallani, V. Guarrera, J. E. Lye, M. Modugno, D. S. Wiersma, and M. Inguscio, "Effect of optical disorder and single defects on the expansion of a Bose-Einstein condensate in a one-dimensional waveguide," *Phys. Rev. Lett.*, vol. 95, p. 170 410, 17 2005.

[32] T. Schulte, S. Drenkelforth, J. Kruse, W. Ertmer, J. Arlt, K. Sacha, J. Zakrzewski, and M. Lewenstein, "Routes towards Anderson-like localization of Bose-Einstein condensates in disordered optical lattices," *Phys. Rev. Lett.*, vol. 95, p. 170 411, 17 2005.

[33] L. Pezzé and L. Sanchez-Palencia, "Localized and extended states in a disordered trap," *Phys. Rev. Lett.*, vol. 106, p. 040 601, 4 2011.

[34] L. Sanchez-Palencia, D. Clément, P. Lugan, P. Bouyer, and A. Aspect, "Disorder-induced trapping versus Anderson localization in Bose-Einstein condensates expanding in disordered potentials," *New J. Phys.*, vol. 10, no. 4, p. 045 019, 2008.

[35] D. J. Thouless, "Phase transitions for the one-dimensional Landau-Ginzburg system and their relation to the theory of polymers and of electrons in a random potential," *J. Phys. Condens. Matter*, vol. 8, no. 12, p. 1803, 1975.

[36] P. Lugan, A. Aspect, L. Sanchez-Palencia, D. Delande, B. Grémaud, C. A. Müller, and C. Miniatura, "One-dimensional Anderson localization in certain correlated random potentials," *Phys. Rev. A*, vol. 80, p. 023 605, 2 2009.

[37] S. Datta, *Quantum Transport: Atom to Transistor*. Cambridge University Press, 2005.

[38] E. Akkermans and G. Montambaux, *Mesoscopic Physics of Electrons and Photons*. Cambrige University Press, 2007.

[39] L. L. Foldy, "The multiple scattering of waves. I. General theory of isotropic scattering by randomly distributed scatterers," *Phys. Rev.*, vol. 67, pp. 107–119, 3-4 1945.

[40] E. A. Cornish and R. A. Fisher, "Moments and cumulants in the specification of distributions," *Revue de l'Institut International de Statistique / Review of the International Statistical Institute*, vol. 5, no. 4, pp. 307–320, 1938.

[41] C. W. Gardiner, *Handbook of Stochastic Methods for Physics, Chemistry and the Natural Sciences*. Springer-Verlag, Berlin, 1997.

[42] M. G. Kendall and A. Stuart, *The Advanced Theory of Statistics*. Charles Griffin and Company Limited, London, 1958, vol. 1.

[43] R. J. Larsen and M. L. Marx, *An Introduction to Mathematical Statistics and Its Applications*. Prentice-Hall International, Boston, 1986.

[44] R. G. Brown, *Introduction to Random Signal Analysis and Kalman Filtering*. John Wiley and Sons, New York, 1983.

[45] H.-H. Kuo, *White Noise Distribution Theory*. CRC Press, New York, 1996.

[46] S. S. Takeyuki Hida, *An Innovation Approach to Random Fields: Application of White Noise Theory*. World Scientific, Singapore, 2004.

[47] D. J. Wales, *Energy Landscapes*. Cambridge University Press, Cambridge, 2004.

[48] J. Bewerunge and S. U. Egelhaaf, "Experimental creation and characterization of random potential-energy landscapes exploiting speckle patterns," *Phys. Rev. A*, vol. 93, p. 013 806, 1 2016.

[49] R. C. Kuhn, O. Sigwarth, C. Miniatura, D. Delande, and C. A. Müller, "Coherent matter wave transport in speckle potentials," *New J. Phys.*, vol. 9, no. 6, p. 161, 2007.

[50] D. Li, D. P. Kelly, and J. T. Sheridan, "Three-dimensional static speckle fields. Part I. Theory and numerical investigation," *J. Opt. Soc. Am. A*, vol. 28, no. 9, pp. 1896–1903, 2011.

[51] ——, "Three-dimensional static speckle fields. Part II. Experimental investigation," *J. Opt. Soc. Am. A*, vol. 28, no. 9, pp. 1904–1908, 2011.

[52] P. Lugan, "Gaz de bosons ultra-froids dans des potentiels desordonnes: Excitations collectives er effets de localisation," PhD thesis, These de doctorat de L'Ecole Polytechnique, Paris, 2010.

[53] E. N. Economou, *Green's Functions in Quantum Physics*. Springer Series in Solid-State Sciences, Berlin, 2006, vol. 7.

[54] I. N. Bronstein, *Handbook of Mathematics*. Springer-Verlag Berlin Heidelberg, 2004.

[55] D. Duffy, *Green's Functions with Applications*. Chapman and Hall/CRC, 2001.

[56] J. Rammer, *Quantum Transport Theory,* Perseus Books, Reading, Massachusetts, 1998.

[57] V. I. Oseledets, "A multiplicative ergodic theorem. Lyapunov characteristic numbers for dynamical systems," *Trans. Mosc. Math. Soc.*, vol. 19, pp. 179 –210, 1968.

[58] H. Furstenberg, "Non-commuting random products," *Trans. Mosc. Math. Soc.*, vol. 108, pp. 377–428, 1963.

[59] H. Furstenberg and H. Kesten, "Products of random matrices," *Ann. Math. Statist.*, vol. 31, no. 2, pp. 457–469, Jun. 1960.

[60] F. M. Izrailev and N. M. Makarov, "Anomalous transport in low-dimensional systems with correlated disorder," *J. Phys. A*, vol. 38, no. 49, p. 10 613, 2005.

[61] A. Crisanti, G. Paladin, and A. Vulpiani, *Products of random matrices in statistical physics,* Springer-Verlag, Berlin, 1933.

[62] R. Landauer, "Spatial variation of currents and fields due to localized scatterers in metallic conduction," *IBM J. Res. Dev.*, vol. 1, pp. 223–231, 1957.

[63] K. Ishii, "Localization of eigenstates and transport phenomena in the one-dimensional disordered system," *Prog. Theor. Phys. Supplement*, vol. 53, pp. 77–138, 1973.

[64] P. W. Anderson, D. J. Thouless, E. Abrahams, and D. S. Fisher, "New method for a scaling theory of localization," *Phys. Rev. B*, vol. 22, pp. 3519–3526, 8 1980.

[65] P. A. Mello, "Macroscopic approach to universal conductance fluctuations in disordered metals," *Phys. Rev. Lett.*, vol. 60, pp. 1089–1092, 11 1988.

[66] P. A. Mello, "Central-limit theorems on groups," *J. Math. Phys.*, vol. 27, no. 12, pp. 2876–2891, 1986.

[67] A. Rodríguez, "Quantum wires in one dimension: Disorder, electronic transport and dissipation," PhD thesis, Universidad de Salamanca, 2005.

[68] R. Johnston and H. Kunz, "The conductance of a disordered wire," *J. Phys. Condens. Matter*, vol. 16, no. 20, p. 3895, 1983.

[69] H. Prüfer, "Neue Herleitung der Sturm-Liouvilleschen Reihenentwicklung stetiger Funktionen," *Math. Ann.*, vol. 95, p. 499, 1926.

[70] H. L. Frisch and S. P. Lloyd, "Electron levels in a one-dimensional random lattice," *Phys. Rev.*, vol. 120, pp. 1175–1189, 4 1960.

[71] H. M. James and A. S. Ginzbarg, "Band structure in disordered alloys and impurity semiconductors," *The Journal of Physical Chemistry*, vol. 57, no. 8, pp. 840–848, 1953.

[72] H. Schmidt, "Disordered one-dimensional crystals," *Phys. Rev.*, vol. 105, pp. 425–441, 2 1957.

[73] A. Suna, "Green's function approach to exciton-phonon interactions," *Phys. Rev.*, vol. 135, A111–A123, 1A 1964.

[74] J. R. Klauder, "The modification of electron energy levels by impurity atoms," *Ann. Phys. (N.Y.)*, vol. 14, pp. 43 –76, 1961.

[75] I. Březinová, L. A. Collins, K. Ludwig, B. I. Schneider, and J. Burgdörfer, "Wave chaos in the nonequilibrium dynamics of the Gross-Pitaevskii equation," *Phys. Rev. A*, vol. 83, p. 043 611, 4 2011.

[76] T. N. Rescigno and C. W. McCurdy, "Numerical grid methods for quantum-mechanical scattering problems," *Phys. Rev. A*, vol. 62, p. 032 706, 3 2000.

[77] B. I. Schneider, L. A. Collins, and S. X. Hu, "Parallel solver for the time-dependent linear and nonlinear Schrödinger equation," *Phys. Rev. E*, vol. 73, p. 036 708, 3 2006.

[78] M. I. Trappe, D. Delande, and C. A. Müller, "Semiclassical spectral function for matter waves in random potentials," *J. Phys. A*, vol. 48, no. 24, p. 245 102, 2015.

[79] P. Pickl, "Derivation of the time dependent Gross-Pitaevskii equation with external fields," *Rev. Math. Phys.*, vol. 27, no. 1550003, pp. 1–45, 2015.

[80] E. H. Lieb, R. Seiringer, and J. Yngvason, "Bosons in a trap: A rigorous derivation of the Gross-Pitaevskii energy functional," *Phys. Rev. A*, vol. 61, p. 043 602, 4 2000.

[81] L. Pitaevskii and S. Stringari, *Bose-Einstein Condensation*. Oxford University Press, Oxford, 2003.

[82] C. J. Pethick and H. Smith, *Bose-Einstein Condensation in Dilute Gases*. Cambrige University Press, 2002.

[83] F. Dalfovo, S. Giorgini, L. P. Pitaevskii, and S. Stringari, "Theory of Bose-Einstein condensation in trapped gases," *Rev. Mod. Phys.*, vol. 71, pp. 463–512, 3 1999.

[84] T. Ernst, T. Paul, and P. Schlagheck, "Transport of ultracold bose gases beyond the Gross-Pitaevskii description," *Phys. Rev. A*, vol. 81, p. 013 631, 1 2010.

[85] I. Březinová, A. U. J. Lode, A. I. Streltsov, O. E. Alon, L. S. Cederbaum, and J. Burgdörfer, "Wave chaos as signature for depletion of a Bose-Einstein condensate," *Phys. Rev. A*, vol. 86, p. 013 630, 1 2012.

[86] T. Geiger, T. Wellens, and A. Buchleitner, "Inelastic multiple scattering of interacting bosons in weak random potentials," *Phys. Rev. Lett.*, vol. 109, p. 030 601, 3 2012.

[87] B. Shapiro, "Expansion of a Bose-Einstein condensate in the presence of disorder," *Phys. Rev. Lett.*, vol. 99, p. 060 602, 6 2007.

[88] D. L. Shepelyansky, "Delocalization of quantum chaos by weak nonlinearity," *Phys. Rev. Lett.*, vol. 70, pp. 1787–1790, 12 1993.

[89] C. Skokos, D. O. Krimer, S. Komineas, and S. Flach, "Delocalization of wave packets in disordered nonlinear chains," *Phys. Rev. E*, vol. 79, p. 056 211, 5 2009.

[90] Y. Kagan, E. L. Surkov, and G. V. Shlyapnikov, "Evolution of a Bose-condensed gas under variations of the confining potential," *Phys. Rev. A*, vol. 54, R1753–R1756, 3 1996.

[91] Y. Castin and R. Dum, "Bose-Einstein condensates in time dependent traps," *Phys. Rev. Lett.*, vol. 77, pp. 5315–5319, 27 1996.

[92] C. Cohen-Tannoudji, B. Diu, and F. Laloë, *Quantum Mechanics,* Hermann Publishers, Paris, 1977.

[93] S. Flach, D. O. Krimer, and C. Skokos, "Universal spreading of wave packets in disordered nonlinear systems," *Phys. Rev. Lett.*, vol. 102, p. 024 101, 2 2009.

[94] K. L. Lee, B. Grémaud, and C. Miniatura, "Dynamics of localized waves in one-dimensional random potentials: Statistical theory of the coherent forward scattering peak," *Phys. Rev. A*, vol. 90, p. 043 605, 4 2014.

[95] T. Karpiuk, N. Cherroret, K. L. Lee, B. Grémaud, C. A. Müller, and C. Miniatura, "Coherent forward scattering peak induced by Anderson localization," *Phys. Rev. Lett.*, vol. 109, p. 190 601, 19 2012.

[96] T. Wellens and B. Grémaud, "Nonlinear coherent transport of waves in disordered media," *Phys. Rev. Lett.*, vol. 100, p. 033 902, 3 2008.

[97] ——, "Coherent propagation of waves in dilute random media with weak nonlinearity," *Phys. Rev. A*, vol. 80, p. 063 827, 6 2009.

[98] T. Geiger, A. Buchleitner, and T. Wellens, "Microscopic scattering theory for interacting bosons in weak random potentials," *New J. Phys.*, vol. 15, no. 11, p. 115 015, 2013.

[99] K. Balzer, S. Bauch, and M. Bonitz, "Efficient grid-based method in nonequilibrium Green's function calculations: Application to model atoms and molecules," *Phys. Rev. A*, vol. 81, p. 022 510, 2 2010.

[100] C. Leforestier, R. H. Bisseling, C. Cerjan, M. D. Feit, R. Friesner, A. Guldberg, A. Hammerich, G. Jolicard, W. Karrlein, H. D. Meyer, N. Lipkin, O. Roncero, and R. Kosloff, "A comparison of different propagation schemes for the time dependent Schrödinger equation," *Journal of Computational Physics*, vol. 94, no. 1, pp. 59 –80, 1991.

A ver, el mundo no es sólo como lo vemos sino también como lo entendemos, ¿no? Y al entender una cosa, le añadimos algo, ¿no? ¿Eso no convierte a la vida en un cuento?

— Yann Martel